ABSTRACT

Title of Dissertation: COLD COLLISIONS IN AN OPTICALLY BRIGHTENED SODIUM BEAM

William Charles DeGraffenreid, Doctor of Philosophy, 2000

Dissertation directed by: Professor John Weiner
Chemical Physics Program

Cold collisions have proved to be a fertile area of research since the development of the magneto-optical trap (MOT), but the spatial averaging of collision axis in this isotropic environment prevents the study of alignment or orientational effects. Experiments performed in a dense, collimated, and slowed beam can provide such an environment.

In the work presented here, we have prepared the brightest atom beam we are aware of, by using optical forces to collimate and longitudinally cool a sodium beam produced from a novel, externally heated source. Optical molasses collimates the atom beam which is subsequently cooled in the longitudinally dimension with a Zeeman compensated cooling method. The atoms are rapidly decoupled from the cooling cycle at $v_{\|} = 350$ m/s to ensure a narrow distribution of longitudinal velocities in the laboratory frame: $\Delta v_{\|} = 5$ m/s. The average

relative velocity of atoms in the beam is $v_r = 3$ m/s and corresponds to a collision temperature of 4 mK. Because the longitudinal temperature is much greater than the transverse velocity, long-range collisions are aligned along the beam axis. The prepared beam density is 7×10^8 atoms/cm^3, a factor of 25 larger than the original thermal beam, allowing data collection to be faster and more efficient than possible with unbrightened beams.

We are the first group to use an optically prepared beam to study an atomic collision. With it, we have studied in detail the polarization dependence of the optical suppression of photoassociative ionization (PAI) in sodium. The polarization axis of a linearly polarized suppression laser is rotated such that the angle between it and the collision axis varies from 0 thru 90 to 180 degrees. For high optical field strengths ($I_S = 2.5$ W/cm^3), a strongly anisotropic suppression of (PAI) is observed, with marked reductions in PAI signal at 55, 90, and 125 degrees. At low suppression laser intensity ($I_S = 0.6$ W/cm^3), collisions are isotropically suppressed. For the higher field intensities we interpret the angular structure in terms of light-field coupling to higher angular momentum partial waves. However, the model only provides a rough picture of the phenomena and does not quantitatively agree with experiment.

COLD COLLISIONS IN AN OPTICALLY BRIGHTENED SODIUM BEAM

by

William Charles DeGraffenreid

Dissertation submitted to the Faculty of the Graduate School of the
University of Maryland, College Park in partial fulfillment
of the requirements for the degree of
Doctor of Philosophy
2000

Advisory Committee:

Professor John Weiner, Chairman/Advisor
Professor Wendell Hill
Special Professor L. G. Marcassa
Professor Robert Walker
Professor Richard Webb

DEDICATION

To my family: while I'm sure they don't understand this stuff, their love made it possible.

ACKNOWLEDGEMENTS

I do not even know where to start thanking people for support that I have received over the years. If I tried to include everyone that I really want to thank, this thesis would have to be broken into two volumes. I have been blessed in my education by being surrounded by many excellent teachers, professors, collaborators, and fellow students. Similarly, without the love and support of my friends and family I doubt that this thesis would have come to fruition.

I guess the first words of thanks should go back to high school. A pair of very special teachers guided me through the wonders of biology, chemistry, and physics: Ms. Eileen Nakagawa and Mr. Frank Arena. Their classes made me want to become a scientist and prepared me for future endeavors in ways that I have just began to comprehend.

The faculty of professors in physics and chemistry at the California State Polytechnic University, Pomona can not begin to understand the influence they had on me. After a year at the University of Arizona left me bitter and broke, this spectacular group of people guided me through the maze of equations, theorems, and laws while taking a genuine interest in me as a young scientist. Profs. Harvey Leff, John Mallinckrodt, Peter Siegel, Kai Lam, Steve McCauley, Elishiva Goldstein, and Charles Millner deserve a special acknowledgement for the discussions over the years. They helped me realize that I had much to offer the world as a scientist that I should take my studies further.

This brings me to the University of Maryland. To my advisor, mentor, and friend, John Weiner: "Thank you." Your support during my graduate studies has molded me into a real experimental scientist. I no longer fear tackling challenges and circuit diagrams. Whether discussing the physics of photoassociation or the implications of the movie "Pulp Fiction", our discussions always were thought provoking and educational. I will miss our chat sessions. Dr. Yinde Wang worked at my side for two years. He taught me so many invaluable lessons that I feared I would not make it alone when he moved on to the campus NMR facilities. Luckily he prepared me well and was only a five-digit phone call away. Dr. Yao-Ming Liu and I toiled together on much of the work presented in this thesis. His willingness to volunteer for the dirty work has become the model I try to follow in the lab. During graduate school, I had the opportunity to spend

four months at our sister laboratory at the Instituto de Física de São Carlos in São Carlos, Brazil. While there I had the pleasure of working with some of the finest people I have ever met in my life. Profs. Vanderlei Bagnato and L. G. Marcassa, along with their graduate students, Sergio Muniz, Lino Misuguti, and Gustave Telles showed me that it is possible to work hard, play hard, and enjoy both. To them: "*Obrigado*". It has been a wonderful pleasure to work with two other students at the University of Maryland: Jaime Ramirez-Serrano and Aaron Rosenbaum. Jaime, a fellow graduate student in the Chemical Physics Program, is well on his way to finishing up his studies. He has shown remarkable talent and I am always amazed at what he manages to get accomplished. Aaron was an undergraduate double major in physics and chemistry at UM that recently moved on to graduate school at the University of Chicago. I am the first to admit that I was hard on him, but only because he handled everything I asked of him and I ran out of easy things. I hope he found the experience as helpful as I did.

I think that the friendships you make in graduate school are of the most important in your life. These friends truly understand what you are going through and share in the highs as well as the lows. I have made so many wonderful friendships in graduate school that I know that I will certainly forget someone if I tried to list them. So I don't forget anyone: a blanket "Thanks" will have to suffice.

I don't think I have made it clear to my family how much their love and support means to me. Mom and Dad, you taught me to work hard, work honestly, and to treat people well. If everybody was learned these simple lessons, the world would be a better place. My siblings (Katie, Mat, and Sarah) have enjoyed harassing me about my receding hairline and are always quick to come up with nerd jokes aimed at me. In my opinion, there is no better expression of sibling love than good natured teasing.

This leaves me with one final person to thank, my dearest Abbey. You came into my life a year and a half ago and made it complete. Your love, support, and wondrously big heart are much more than I deserve. I wake everyday happy that I have all three.

TABLE OF CONTENTS

List of Tables **x**

List of Figures **xi**

1 Introduction **1**

2 Laser Cooling **5**

2.1 Coldness 7

2.2 Mechanical Effects of Light I: The Dipole Force 9

2.3 Mechanical Effects of Light II: Radiation Pressure Force 12

2.3.1 One Dimensional Slowing 17

2.3.2 Optical Molasses 19

2.3.3 Magneto-Optical Trap 24

2.4 Mechanical Effects of Light III: Sub-Doppler Cooling 27

2.5 Discussion of Laser Cooling 31

3 Experimental System **33**

3.1 Laser and Optical System 33

3.2 Atomic Sodium 37

3.2.1 Atomic States 37

3.2.2 Zeeman Splitting 40

3.2.3 "Real" Laser Cooling 43
3.3 Frequency References 46
3.3.1 Crossed Beam Spectroscopy 47
3.3.2 Saturated Absorption Spectroscopy 47
3.3.3 Molecular Iodine 54
3.4 Electro-optics 54
3.4.1 Acousto-optic modulators 55
3.4.2 Electro-optic modulators 57
3.5 Vacuum System 58
3.6 Signal Detection and Data Acquisition 60
3.6.1 Charged Coupled Device Cameras 60
3.6.2 PMT 62
3.6.3 Ion Detection 63

4 A Bright, Cold Sodium Beam 65

4.1 Introduction 65
4.1.1 Beam Performance Measures 67
4.2 Review of Beam Sources 68
4.3 Experiment 72
4.3.1 Résumé 72
4.3.2 Thermal Beam Source 73
4.3.3 Optical Collimation 77
4.3.4 Longitudinal Cooling 81
4.3.5 Extraction 86
4.4 Beam Diagnostics 88
4.4.1 Atom Beam Size and Density 89

4.4.2 Longitudinal Velocity Distribution 91
4.4.3 Transverse Velocity Estimation 95
4.5 Conclusions 96

5 Polarization Dependence of the Optical Suppression of Photoassociation 98

5.1 Introduction 98
5.1.1 Long-range Internuclear Potentials 99
5.1.2 Photoassociative Ionization 101
5.1.3 Optical Suppression 104
5.2 Early Suppression Experiments 106
5.2.1 Experimental Investigations 106
5.2.2 Theoretical Investigations 110
5.3 Experiment 118
5.3.1 Lasers 118
5.3.2 Atom Beam 120
5.3.3 Collision Experiment 121
5.4 Results 126
5.5 Theory 128

6 Summary and Discussion 132

A Notations and Definitions 135

Bibliography 140

LIST OF TABLES

2.1 Summary of radiation forces. 32

4.1 Beam performance. 96

5.1 Comparison of different models of suppression. 117

5.2 Laser frequencies in laboratory and atomic frames. 122

LIST OF FIGURES

1.1 Alignment of collision and laboratory beam axes. 3

2.1 The dipole force as a function of position for a 1D laser intensity profile. 11

2.2 Schematic diagram of radiation pressure cooling. 13

2.3 Radiation pressure force. 15

2.4 The Doppler shift of the radiation pressure force. 16

2.5 The Zeeman effect. 18

2.6 Radiation pressure force for 1D optical molasses. 21

2.7 One-dimensional MOT. 25

2.8 Photograph of a sodium MOT. 26

2.9 Sub-Doppler molasses temperature. 28

2.10 $Lin \perp lin$ cooling process. 29

3.1 Laser system. 34

3.2 Atomic energy level diagram for ^{23}Na. 39

3.3 The Zeeman effect in ^{23}Na. 41

3.4 Optical repumping needed in laser cooling of Na. 45

3.5 Crossed beam fluorescence spectra. 48

3.6 Saturated absorption optical setup. 49

3.7 Saturated absorption amplification circuit. 52
3.8 Sodium saturated absorption spectrum. 53
3.9 Iodine fluorescence spectrum. 55
3.10 Acousto-optic and electro-optic modulators. 56
3.11 Vacuum system system. 59
3.12 Schematic of detection devices around the interaction region. . . . 61
3.13 Block diagram of data acquisition. 62

4.1 Comparison of several beam sources. 72
4.2 Schematic of beam source. 74
4.3 Cutaway diagram of thermal sodium beam source. 75
4.4 Collimation chamber. 79
4.5 2D versus 2 × 1D molasses. 80
4.6 Fringe field cancellation. 81
4.7 The magnetic field inside the Zeeman cooler as a function of position. 83
4.8 Model intensity for longitudinal slowing laser as a function of upstream distance. 85
4.9 Magnetic field and field gradient at the end of the Zeeman slower. 87
4.10 Fluorescence profiles of the collimated and uncollimated atom beams. 90
4.11 Doppler spectra for hot and cold atom beams. 92
4.12 Laboratory and relative velocity distributions. 94

5.1 Photoassociative ionization in sodium. 101
5.2 Optical suppression of PAI. 105
5.3 Early optical suppression experiments I. 108
5.4 Early optical suppression experiments II. 109

5.5 Polarization dependence of optical suppression in a sodium beam. 110
5.6 Avoided crossing in 1D L-Z model. 112
5.7 Intensity dependent penetration probability, in 1D L-Z model, for sodium. 113
5.8 3-D Landau Zener model of optical suppression. 114
5.9 3-D Quantum Close Coupling model. 116
5.10 Overview of experiment. 119
5.11 Frequencies and Condon radii for suppression experiment. 123
5.12 Timing diagram for PAI counting. 125
5.13 Fractional ionization as a function of the angle and intensity. . . . 127
5.14 Three-dimensional quantum close coupling (3D QCC) model for penetration probability. 129
5.15 Corrected 3D quantum close coupling (Corrected 3D QCC) model for penetration probability. 130

6.1 Polarization dependent photoassociative ionization spectra below the D2 resonance in sodium. 134

Chapter 1

Introduction

Optical cooling opened a new world of research for physicists and chemists, where atoms are slowed down to velocities in the quantum mechanics realm. While the earliest experiments were used to slow atomic beams for the purpose of loading optical traps, the development of vapor cell three-dimensional atom traps diverted the focus away from improving beam performance. Recently, atomic beams prepared with laser cooling techniques have reemerged as a valuable tool in the laboratory.

Compared to the vapor cell magneto-optic traps (MOTs) discussed in Chapter 2, cold, bright atom beams did not gain favor because of the complexity of preparing a beam with high density and low divergence. The vacuum system required for a beam is much more complicated than the simple vapor cell chambers used for MOTs. The large flux from hot, effusive atom sources require pumps with high pumping speed and several subsequent differentially pumped stages to maintain an adequate vacuum for experimental conditions. Cooling alkali atoms exiting the thermal source ($\langle v \rangle \sim 1000$ m/s) to near zero velocity requires long chambers (≥ 1 m) where beam divergence significantly reduces the density of slow atoms after longitudinal cooling. The length of the chamber also necessi-

tates the ability to carefully position the source with respect to the rest of the vacuum chamber. In short, vapor cell traps became such a comparatively simple and inexpensive alternative that most research groups began using them.

Although the vapor cell trap is immensely popular, there are many instances when a bright atom beam, characterized by high density and low divergence, is required. Trap loading efficiency can be improved by using brightened beams. Beams of radioactive atomic isotopes produced from accelerators suffer from low flux and high divergence; collimation of the beam increases the number of atoms that become trapped [1]. Introducing atoms to a trap within an ultrahigh vacuum chamber via a cold bright beam increases the size and density of the optical trap [2–4]: an important precursor to the production of Bose-Einstein condensation. Atom interferometry is possible with the flux from an optically brightened atom beam with a mono-energetic longitudinal velocity [5, 6]. Collimation of atom beams by reducing the transverse velocity of atoms within the beam narrows the absorption linewidths in crossed beam Doppler-free laser spectroscopy [7]. Nanolithography requires beams with large flux and low divergence; optically brightening beams reduces the time needed to write-to or etch-from a substrate [8–12]. In the work in this thesis, a bright beam serves as the environment in which collision experiments are performed.

The low divergence, high density, and monochromaticity of velocity of an optically prepared atom beam provide orientational and alignment opportunities for collisional studies not possible within a vapor cell. Atoms colliding within a beam are useful for studying effects dependent upon orientation of the collision axis with respect to an external field [13]. For a broad class of collisions involving excited state atoms, the average collision axis is restricted to a small acceptance

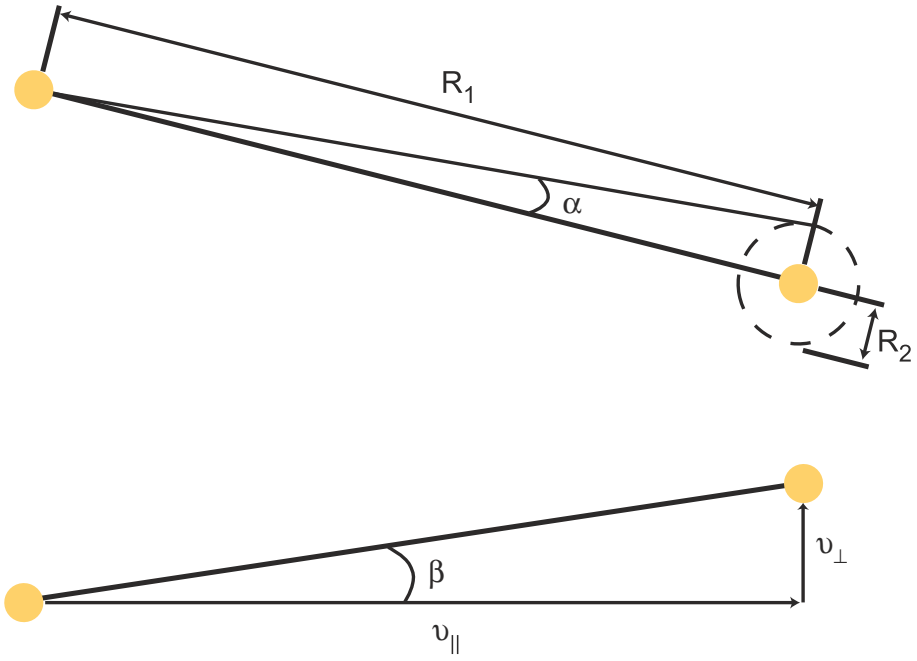

Figure 1.1: The narrow acceptance angle α for the collision process is defined by a two-step process: excitation at R_1 and collision at R_2. Collimating the atom beam results a small divergence angle β because the transverse velocity $v_\perp$ is much less than the longitudinal velocity $v_\parallel$. Because α and β are small, the collisions are restricted along the beam axis.

angle α determined by the excitation radius (R_1) and the "collision radius (R_2)" as shown in Fig. 1.1. In a well-collimated atom beam, the center-of-mass laboratory velocity, with transverse velocity $v_\perp$ and longitudinal velocity $v_\parallel$ for a pair of atoms diverges from the laboratory beam axis by a small angle $\beta = \tan^{-1} v_\perp / v_\parallel$ as shown in Fig. 1.1. The small angular divergence of both the collision and velocity axes ensure that the collision axis is aligned with the laboratory beam axis. Additionally, the beam symmetry defines a good quantization axes for collisional effects that are state dependent, where a laser beam prepares the

atoms in well defined quantum states via optical pumping techniques. Examples of recent intrabeam collision experiments are spin-changing collisions in cesium [14], photoassociative ionization [15] and associative ionization [16] collisions in sodium, and energy pooling collisions in strontium [17].

In this thesis, we describe the production of a bright, continuous sodium atom beam using laser cooling techniques and how we use the beam to study the polarization dependence of the optical suppression of the rate of inelastic collisions. A summary of the physics of the mechanical effects of light is presented in Chapter 2. The summary is not intended to be a complete development of the theory, but rather to serve as a reference for optical cooling as it is applied within the work summarized here. Chapter 3 summarizes the details of the experiment such as the laser systems, atomic structure, and vacuum system. The details of producing a bright, dense, highly-collimated sodium atom beam are described in Chapter 4, along with the diagnostic techniques used to characterize the beam performance. Using the beam described in Chapter 4, we determine the polarization dependance of optical suppression of photoassociative ionization collisions between sodium atoms and present the results in Chapter 5. Chapter 6 summarizes the work in this thesis and contains a discussion of the future of collision studies within atomic beams.

Chapter 2

Laser Cooling

Over the last twenty years, optical cooling techniques have rapidly developed from a research topic into a tool used in many laboratories. Optical forces are used to deposit [6, 8–10], or in some cases to etch [11, 12], structures on surfaces, to study reactions between viruses and inhibitors [18], and as the first step in creating Bose-Einstein Condensation (BEC) [19]. In this thesis, optical forces brighten a thermal beam of sodium atoms.

In the dipole approximation, the interaction energy of a light field and atom is given by

$$U = -\overrightarrow{d} \cdot \overrightarrow{E} \tag{2.1}$$

where $\overrightarrow{d}$ is the transition dipole and $\overrightarrow{E} = \overrightarrow{\varepsilon} E_0[\cos(\omega_L t - \overrightarrow{k_L} \cdot \overrightarrow{r})]$ is the electric field of the light with polarization vector $\overrightarrow{\varepsilon}$. The negative spatial gradient of the interaction energy is the force exerted on the atoms

$$\overrightarrow{F} = -\overrightarrow{\nabla} U = \tilde{d} \overrightarrow{\nabla} E \tag{2.2}$$

where the gradient of the dipole itself is negligible because the dipole does not vary significantly over the length scale of the wavelength of the light. Here we

have set $\widetilde{d} = \overrightarrow{d} \cdot \overrightarrow{\varepsilon}$ to simplify notation. The average force exerted on the atom is

$$\left\langle \overrightarrow{F} \right\rangle = \left\langle \widetilde{d}\overrightarrow{\nabla}E \right\rangle = \widetilde{d}[(\nabla E_0)u_{ss} + (E_0\nabla(-\overrightarrow{k_L} \cdot \overrightarrow{r}))v_{ss}] \tag{2.3}$$

where u_{ss} and v_{ss} arise from an analysis of the steady-state solutions to the optical Bloch equations [20]:

$$u_{ss} = \frac{\Omega}{2}\frac{\Delta}{\Delta^2 + (\Gamma/2)^2 + \Omega^2/2} \tag{2.4}$$

and

$$v_{ss} = \frac{\Omega}{2}\frac{\Gamma/2}{\Delta^2 + (\Gamma/2)^2 + \Omega^2/2}. \tag{2.5}$$

In Eqns. 2.4 and 2.5, the detuning $\Delta = \omega_L - \omega_0$ is the difference between the laser frequency ω_L from the atomic resonant frequency ω_0, Γ is the natural linewidth of the transition, and the Rabi frequency Ω is a measure of the coupling strength of the atom and field

$$\Omega = -\frac{\widetilde{d}E_0}{\hbar}. \tag{2.6}$$

The two terms in Eqn. 2.3 summarize the forces exerted on an atom within a light field. The first term is proportional to the gradient of the electric field amplitude, sometimes called the dipole force, and the second is proportional to the gradient of the phase, usually called the radiation pressure force for reasons to become clear later. The lineshape function for the dipole force is dispersive and changes sign as the detuning of the laser passes through zero. The radiation pressure force has a Lorentzian profile peaking at zero detuning. This chapter, after a brief discussion of how to characterize the temperature of a cold sample of atoms, presents a brief summary of the dipole and radiation pressure forces

and how they can be implemented to cool an ensemble of atoms to very low temperatures. Additional cooling mechanisms that cool atoms to even lower temperatures, called sub-Doppler cooling, are also described here.

A common source of confusion for the cooling and trapping novice is the usage of frequency. Experimentally, frequency is measured and reported in terms of cycles per second (Hz). Theorist, however, generally use angular frequency, measured in radians per second (s^{-1}), but not always. It is not uncommon in literature for factors of 2π to disappear and reappear without warning. In this thesis, all theory is developed and presented in angular frequency units (rad/s), but experimental results are presented in linear frequency (Hz); therefore when applying experimental frequencies to an equation, they must first be converted to the angular form by multiplying by a factor of 2π. When referring to literature cited in this thesis, care must be taken to ensure the correct use of frequency because there is no universal standard.

2.1 Coldness

The kinetic energy of cooled atoms is so low that it is impossible to measure the temperature with conventional probes. To understand the notion of temperatures as described within this thesis, a brief discussion s presented here. "Coolers and trappers" commonly define temperature by equating the thermal energy to the average kinetic energy. For a system with n degrees of freedom the temperature is calculated from

$$\frac{n}{2}k_B T = \frac{1}{2}m\left\langle v\right\rangle^2 \tag{2.7}$$

where k_B is the Boltzman constant and m is the atomic mass of an atom with average (rms) velocity $\langle v \rangle$.

For atoms trapped in three dimensions, the idea of a realistic temperature $T = m \langle v \rangle^2 / 3k_B$ is reasonable. However, assigning a temperature to atoms in a beam is difficult because the longitudinal and transverse components have distinct velocity distributions. Also, while atoms may have a large velocity in the laboratory reference frame, a narrow velocity dispersion within this moving frame yields low relative velocities and correspondingly low collision temperatures. While defining temperatures along different directions may not be proper in a thermodynamic sense, coolers and trappers bravely forge ahead where thermodynamicists fear to tread to allow comparisons between experiment and simple theoretical models. The transverse temperature T_{trans} has two degrees of freedom, due to cylindrical symmetry, and is

$$T_{trans} = \frac{m \langle v \rangle^2}{2k_B}. \tag{2.8}$$

Because of the longitudinal velocity of the atoms is in a moving frame, we define the longitudinal temperature T_{long}, which has only a single degree of freedom, with respect to the average longitudinal velocity v_0:

$$T_{long} = \frac{m \langle |v - v_0| \rangle^2}{k_B}. \tag{2.9}$$

In the case of collision studies, we are interested in the collision temperature T_{coll}. The convention for calculating the temperature is given by

$$T_{coll} = \frac{\mu_m \langle v_r \rangle^2}{2k_B} \tag{2.10}$$

where μ_m is the reduced mass for the pair of colliding atoms and $\langle v_r \rangle$ is the average relative velocity between a pair of atoms.

The definitions presented here vary slightly from research group to research group and have not gained universal acceptance so they should not be taken as an absolute. But these definitions will be used consistently within this thesis.

2.2 Mechanical Effects of Light I: The Dipole Force

While the dipole force does not play a major role within the experimental work described in this thesis, a brief development of the physics is presented here for completeness. Inserting Eqn. 2.4 into the first term of Eqn. 2.3, the dipole force is

$$\overrightarrow{F}_{dip} = \widetilde{d}(\overrightarrow{\nabla} E_0)\frac{\Omega}{2}\frac{\Delta}{\Delta^2 + (\Gamma/2)^2 + \Omega^2/2}. \tag{2.11}$$

With some algebra and using the definition of the Rabi frequency from Eqn. 2.6, the dipole force can be expressed as [20]:

$$\overrightarrow{F}_{dip} = -\frac{\hbar(\overrightarrow{\nabla}\Omega^2)}{4}\frac{\Delta}{\Delta^2 + (\Gamma/2)^2 + \Omega^2/2}. \tag{2.12}$$

While technically complete at this point, it is generally more useful to handle measurable the quantity of optical field intensity, rather than the Rabi frequency, when calculating the force. The Rabi frequency is related to the intensity of the laser by the following relation

$$S_0 = \frac{I}{I_S} = \frac{\Omega^2/2}{(\Gamma/2)^2}. \tag{2.13}$$

Here the on-resonance saturation parameter S_0 is the ratio of the local laser intensity I to the saturation intensity I_S. The saturation intensity I_S is a characteristic intensity $I_S = \hbar\Gamma\omega_0^3 / 12\pi c^2$ for a two level atom at which 25% of the

atomic population is in the excited state for a two state system when the laser is resonant (although some characterize I_S as the intensity at which one third of the atoms are in the excited state). Using Eqn. 2.13, the dipole force reduces to

$$\overrightarrow{F}_{dip} = -\frac{\hbar}{2}\frac{\Delta}{I_S}\frac{\nabla I}{\left(\frac{2\Delta}{\Gamma}\right)^2 + \frac{I}{I_S} + 1}. \tag{2.14}$$

From Eqn. 2.14, it is clear that for the case of the laser tuned below the atomic resonance ($\Delta < 0$), the force is directed toward the maximum intensity, whereas a blue detuned laser ($\Delta > 0$) results in repulsion from high laser intensity.

The dipole force is not a resonant process, in fact, it goes to zero while on resonance. While the force is maximum at half the natural linewidth, unless there is an intensity gradient, the force is small. Also, while the force falls off as Δ^{-1} for large detunings, a strong field intensity gradient ∇I may compensate enough for a significant force to be exerted on an atom.

Very high field gradients are possible by simply focusing a beam to a small spot size. To minimize absorption and spontaneous emission of photons from the laser beam, it is typically tuned well away from the atomic resonance. For $\Delta < 0$, within the focal spot, the dipole force is exerted toward intensity maximum at the center as shown in Fig. 2.1. Atoms oscillate in the trapping potential

$$U_{trap} = \frac{\hbar\Delta}{2}\ln\left[\left(\frac{2\Delta}{\Gamma}\right) + \frac{I}{I_S} + 1\right] \tag{2.15}$$

that is obtained by integrating the force. This kind of trap, called a far-off resonance trap, or FORT, cannot remove energy from the atomic ensemble. Atoms must have kinetic energy less than the trapping potential in order to remain in the trap. In other words, the atoms must be cooled before then can be confined. However, once trapped, the atoms are held for long periods of time and can be the subject of many sorts of fundamental studies.

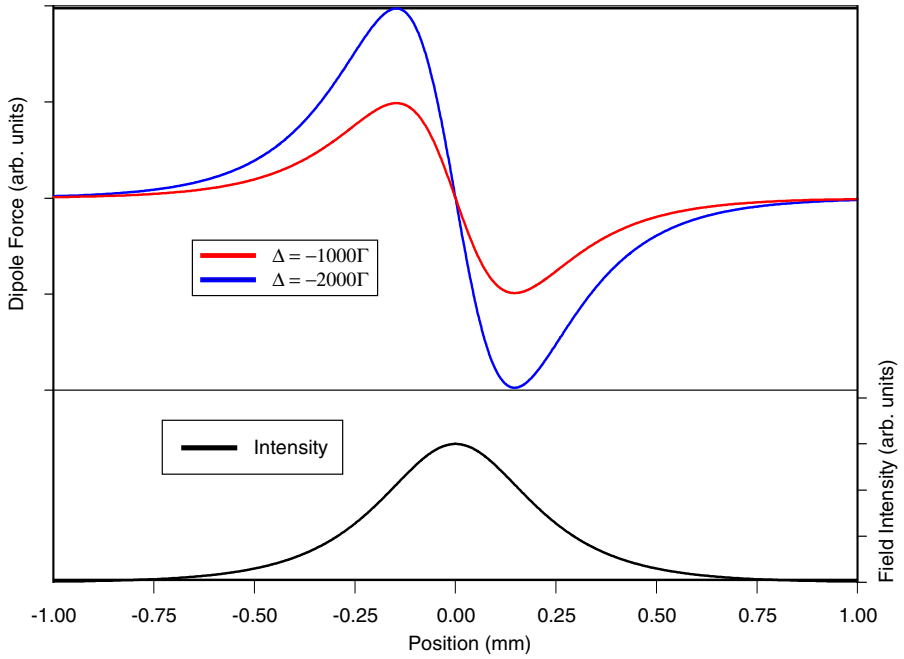

Figure 2.1: The dipole force as a function of position for a focused, 1D laser intensity profile for two different laser detunings, -1000Γ and -2000Γ.

The dipole force can also be extended to larger particles such as living cells and micro-spheres [18, 21]. The trapping potential from a tightly focused beam is strong enough to hold onto such particles. When used on these micro- and meso-scopic particles, the focused beam is called optical tweezers. Broad areas of biotechnology and nanotechnology research have developed around implementation of optical tweezers.

Optical guides that transport atoms without divergence over distances of tens of cm are produced using the dipole force [22, 23]. A hollow beam of light tuned to the blue of the atomic resoance will exert a restoring force towards regions of low field intensity. If atoms are loaded into the hollow center, the force prevents

them from moving outside of the hollow guide. Because the atoms do not touch matter, this method will be useful in transporting metastable species, such as the noble gases, and antimatter.

2.3 Mechanical Effects of Light II: Radiation Pressure Force

The radiation pressure force can be explained with a semi-classical model. Consider a two-level atom, with ground state $|1\rangle$ and excited state $|2\rangle$ separated by $\Delta E = E_2 - E_1 = \hbar\omega_0$, subject to a monochromatic, continuous laser beam, with frequency ω_L propagating along the direction of the wavevector $\overrightarrow{k_L}$ (often more conveniently expressed as $\frac{2\pi}{\lambda}\widehat{k}_L$ because the laser wavelength λ is easier to measure). Because the momentum of each photon within the laser beam is $\hbar\overrightarrow{k_L}$, absorption of a resonant photon results in a momentum transfer of one photon momentum unit to the atom. The atom receives a small kick in the direction of laser propagation. The excited atom is not stable and decays by emitting a photon with frequency ω_0 and momentum $\hbar\overrightarrow{k'_L}$. Even though a two-level atom does not decay isotropically, real atoms with angular momentum decay nearly symmetrically. Under the assumption of isotropic spontaneous decay, the wavevector $\overrightarrow{k'_L}$ of the emitted photon has equal probability of decaying to any direction within the 4π solid angle around the atom. Therefore over many cycles, the momentum change exerted on the atom by spontaneous decay averages to zero. As long as the laser beam remains resonant with the atom, this cycling process continues with an average momentum transfer of $\hbar\overrightarrow{k_L}$ per absorption cycle, resulting in a force $\frac{d\overrightarrow{p}}{dt}$ that decelerates the atom. Figure 2.2 schematically shows the process.

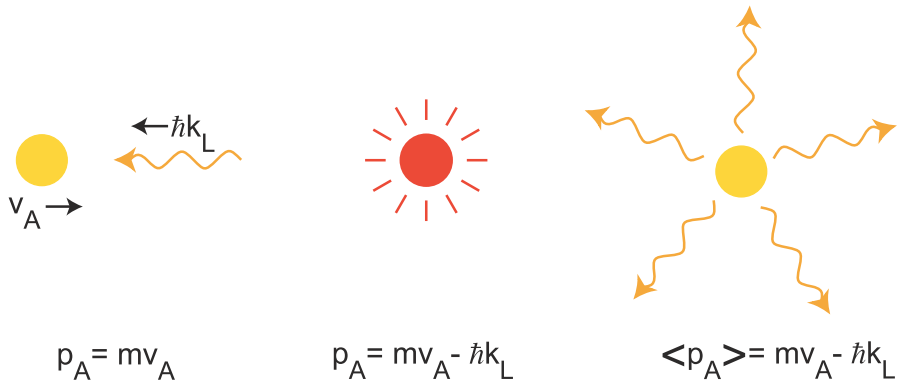

Figure 2.2: Schematic diagram of the radiation pressure force. Over the course of an absorption cycle, the internal energy E_A is unchanged, the momentum of the atom is decreased by an amount equal to the photon momentum due to the isotropic nature of spontaneous decay.

The trick, as will soon be shown, is to keep the atom resonant.

To be more quantitative, we again turn to Eqn. 2.3; this time we focus on the second term. When combined with Eqn. 2.5, the radiation pressure force is given by

$$\overrightarrow{F}_{rad} = -\widetilde{d}E_0\overrightarrow{k_L}\frac{\Omega}{2}\frac{\Gamma/2}{\Delta^2 + (\Gamma/2)^2 + \Omega^2/2} \tag{2.16}$$

where we have already evaluated the phase gradient for a plane wave. By using the definition of the Rabi frequency Ω (Eqn. 2.6) and the resonant saturation parameter S_0 (Eqn. 2.13) the force simplifies to

$$\overrightarrow{F}_{rad} = \frac{\hbar\Gamma\overrightarrow{k_L}}{2}\frac{S_0}{\left(\frac{2\Delta}{\Gamma}\right)^2 + S_0 + 1}. \tag{2.17}$$

The radiation pressure force can also be derived in a different way. The force equals the rate of momentum transfer from the laser beam [20]:

$$\overrightarrow{F}_{rad} = \left\langle \frac{dN_{photon}}{dt} \right\rangle_L \hbar\overrightarrow{k_L}. \tag{2.18}$$

where $\left\langle \frac{dN_{photon}}{dt} \right\rangle_L$ is the rate of photon "scattering" and equals

$$\left\langle \frac{dN_{photon}}{dt} \right\rangle_L = \frac{\rho_2}{\tau} = \rho_2 \Gamma \tag{2.19}$$

where ρ_2 is the excited state population and τ is the excited state radiative lifetime ($\Gamma = 1/\tau$). We calculate the excited state population ρ_2 from the optical Bloch equations [20]

$$\rho_2 = \Omega \upsilon_{ss}. \tag{2.20}$$

Combining Eqns. 2.19 and 2.20 we see that the "scattering" derivation is equivalent to "phase gradient" derivation. The resulting force has a Lorentzian shape as a function of frequency that broadens with increased laser intensity as shown in Fig. 2.3.

Up to this point, the force given by Eqn. 2.17 ignores the velocity of the atom. However, the laser frequency, within the atomic reference frame, is not equal to the frequency in the laboratory frame because of the Doppler effect. In the moving frame, the shifted laser frequency ω_L' is

$$\omega_L' = \omega_L + \Delta\omega_D \tag{2.21}$$

where ω_L is the frequency measured in the laboratory frame and $\Delta\omega_D$ is the Doppler shift given by

$$\Delta\omega_D = -\overrightarrow{k_L} \cdot \overrightarrow{\upsilon_A} \tag{2.22}$$

where the atomic velocity is $\overrightarrow{\upsilon_A}$. Because of the Doppler effect, light resonant with atoms at rest in the laboratory frame may be shifted well off of resonance in the frame of moving atoms. If the atom moves toward the laser beam (i.e. the atom and photon momentums oppose each other $\widehat{\upsilon_A} = -\widehat{k_L}$), the Doppler shift

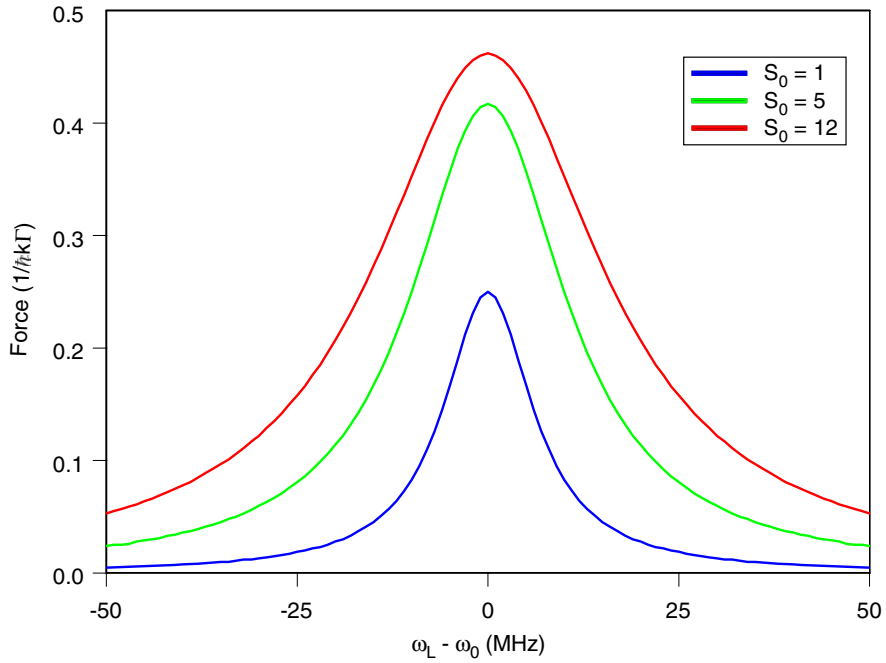

Figure 2.3: The radiation pressure force as a function of frequency (with respect to the atomic resonance). As the intensity of the laser increases, as measured with the saturation parameter S_0, the force increases in strength and broadens in frequency dependence.

$\Delta\omega_D$ is greater than zero and the apparent frequency increases, referred to as a blue shift. The laser frequency must be set below the atomic resonance for the moving atoms to come into resonance. Similarly, atoms moving along with the laser beam are resonant with the laser when tuned to frequencies above the rest frame resonance.

If we add the Doppler shift to Eqn. 2.17 and clarify the definition of detuning Δ as

$$\Delta = \omega_L - \omega_0 \tag{2.23}$$

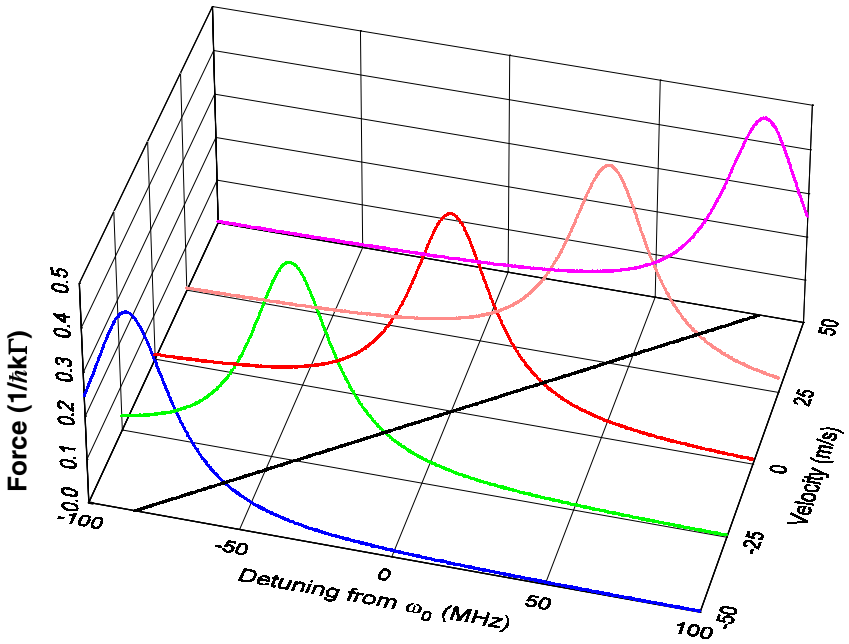

Figure 2.4: The effect of Doppler shift on the radiation pressure force for several velocities for the case of sodium ($\Gamma = 10$ MHz, $\lambda = 589$ nm) as a function of detuning Δ from the rest frame resonance for $S_0 = 10$. The line in the base plane indicates the resonant detuning for a given velocity.

as the difference between the laboratory frame laser frequency ω_L and the atomic frequency ω_0 we have

$$\overrightarrow{F}_{rad} = \frac{\hbar\Gamma\overrightarrow{k_L}}{2}\frac{S_0}{\left[\frac{2(\Delta-\overrightarrow{k_L}\cdot\overrightarrow{v_A})}{\Gamma}\right]^2 + S_0 + 1}. \tag{2.24}$$

The effect of the Doppler shift on the radiation pressure force is shown in Fig. 2.4. Radiation pressure exerts a force on counter-(co-)propagating atoms only if the laser is tuned below (above) the atomic resonance.

The presence of a magnetic field also affects the dynamics of the radiation

pressure force and will prove to be an important part of slowing and trapping atoms. The Zeeman effect splits and shifts the magnetic sublevels of the atom. If a state of the atom has an angular quantum number **J** with magnetic quantum numbers $M = -\mathbf{J}, -\mathbf{J}+1, \ldots, +\mathbf{J}$, the presence of the magnetic field B splits the levels from the zero field energy by an amount

$$\Delta\varepsilon_M = gM\mu_B B \tag{2.25}$$

where g is the Landé factor for the level and μ_B is the Bohr magneton ($e\hbar/2m_e = 9.274\times10^{-28}$ J/G) [24]. The exact value of the Landé factor depends on whether the level is a fine- or hyperfine-state and will be discussed in more detail in Chapter 3 when we consider the application of radiation pressure to a real atom. The transition energy between the ground- and excited-states is given by

$$\Delta E = \hbar\omega_0 + (M_2 g_2 - M_1 g_1)\mu_B B \equiv \hbar\omega_0 + \mu_{12} B \tag{2.26}$$

where we have defined μ_{12} as the Bohr constant for the $|1, M_1\rangle \longrightarrow |2, M_2\rangle$ transition. The Zeeman splitting of a fictitious atom with $\mathbf{J}_1 = 0$ and $\mathbf{J}_2 = 1$ is shown in Fig. 2.5. Adding the Zeeman effect to Eqn. 2.24 by replacing ω_0 with $\omega_0 + \frac{\mu_{12}B}{\hbar}$, and maintaining the definition of Δ, we have

$$\overrightarrow{F}_{rad} = \frac{\hbar\Gamma\overrightarrow{k_L}}{2}\frac{S_0}{\left[\frac{2(\Delta - \overrightarrow{k_L}\cdot\overrightarrow{v_A} + \frac{\mu_{12}B}{\hbar})}{\Gamma}\right]^2 + S_0 + 1}. \tag{2.27}$$

2.3.1 One Dimensional Slowing

Light forces were first used to slow the motion of atoms in a beam by exposing them to a counter-propagating laser tuned near the atomic resonance. Because

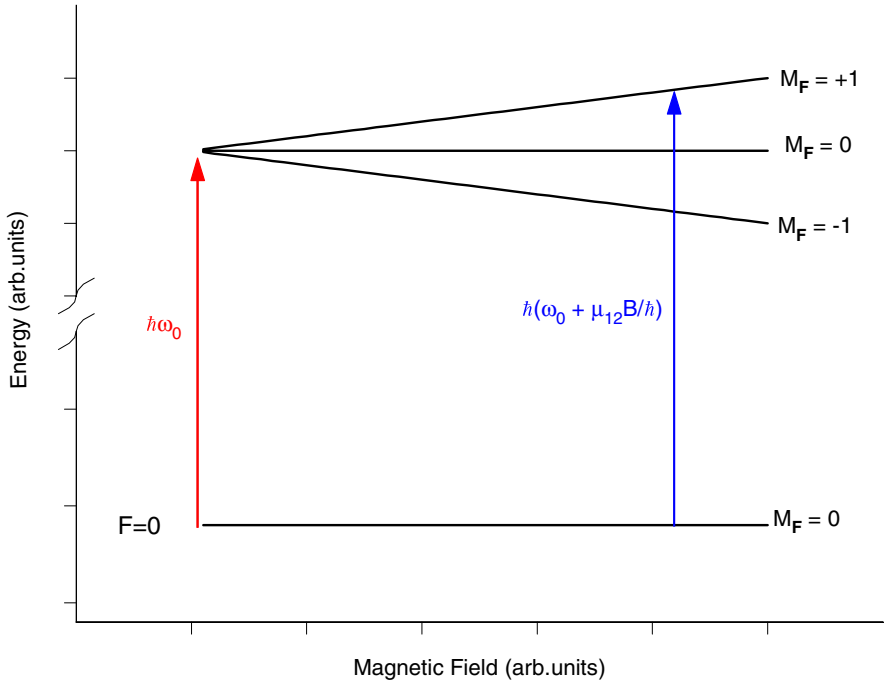

Figure 2.5: The Zeeman splitting of an atom with $\mathbf{J}_1 = 0$ and $\mathbf{J}_2 = 1$.

the force applied in the direction opposing the velocity of the atoms for a counter-propagating laser beam, absorption of photons decelerates atoms in the beam

$$\frac{dv_A(t)}{dt} = \frac{\overrightarrow{F}_{rad}}{m}. \tag{2.28}$$

The force is maximum when the Doppler shifted laser frequency equals the Zeeman shifted transition frequency

$$\Delta - \overrightarrow{k_L} \cdot \overrightarrow{v_A} + \frac{\mu_{12} B}{\hbar} = 0 \tag{2.29}$$

which, for a high laser field intensity ($S_0 \gg 1$), is

$$\overrightarrow{F}_{rad}^{\max} = \frac{\hbar \Gamma \overrightarrow{k}}{2}. \tag{2.30}$$

As the force decelerates the beam, the Doppler shift changes. To maintain the maximum force given by Eqn. 2.30 either the detuning Δ or the Zeeman shift $\frac{\mu_{12}B}{\hbar}$ must simultaneously change for the resonant condition given by Eqn. 4.15 to remain valid. If no compensation occurs, the force decreases and approaches zero as it moves down the Lorentzian wings of Eqn. 2.27. Two techniques to compensate for the Doppler shift are commonly used, one shifts the laser while the internal structure of the atom is changed in the second. Sweeping the laser frequency at a rate that exactly compensates for the changing Doppler shift (chirp cooling) [25] produces a pulsed output of cold atoms superimposed on an uncooled flux. A spatially varying magnetic field that changes the Zeeman shift while the atom slows (Zeeman compensated cooling) produces a continuous output [26]. The Zeeman cooling technique will be discussed in detail in Chapter 3. Both processes have been used to slow down and, in some cases, reverse the velocity of atoms within a beam.

For sodium, the maximum force equals 3.5×10^{-20} N. While seemingly small, the *acceleration* of the sodium atom ($m = 3.84 \times 10^{-26}$ kg) is 9×10^5 m/s^2, nearly 10^5 times the gravitational acceleration on earth! Consider an atom with an initial velocity of 1000 m/s. If the maximum force is maintained during the entire slowing process, it takes $34,000$ absorption cycles and 1.1 ms to bring the atom to rest.

2.3.2 Optical Molasses

While a single laser beam can slow and cool a beam of atoms, pairs of counter-propagating laser beams can cool atoms moving with a velocity component along the propagation axis [27]. To simplify the theoretical development, consider an

ensemble of atoms restricted to move along a single axis in a one-dimensional universe. While unrealistic, the one-dimensional model is straightforward and provides a basis for understanding the cooling process. Two equal intensity, counter-propagating laser beams with the same detuning Δ, aligned along the axis of atom motion, impinge on the ensemble, which is in a region free of magnetic fields. The force exerted on the atoms is the linear combination of the forces from each individual laser beam, given by Eqn. 2.24, and equals

$$\overrightarrow{F} = \frac{\hbar\Gamma\overrightarrow{k_{L1}}}{2}\frac{S_0}{\left[\frac{2(\Delta-\overrightarrow{k_{L1}}\cdot\overrightarrow{v_A})}{\Gamma}\right]^2 + S_0 + 1} + \frac{\hbar\Gamma\overrightarrow{k_{L2}}}{2}\frac{S_0}{\left[\frac{2(\Delta-\overrightarrow{k_{L2}}\cdot\overrightarrow{v_A})}{\Gamma}\right]^2 + S_0 + 1}. \quad (2.31)$$

The magnitude of the wavevectors are equal, but opposite in direction ($\overrightarrow{k_{L1}} = -\overrightarrow{k_{L2}} \equiv \overrightarrow{k_L}$). It is also assumed that the direction of positive atomic velocity is aligned with the wavevector $\overrightarrow{k_L}$. The force simplifies to

$$\overrightarrow{F} = \frac{\hbar\Gamma\overrightarrow{k_L}}{2}\left[\frac{S_0}{\left[\frac{2(\Delta-|k_L v_A|)}{\Gamma}\right]^2 + S_0 + 1} - \frac{S_0}{\left[\frac{2(\Delta+|k_L v_A|)}{\Gamma}\right]^2 + S_0 + 1}\right]. \quad (2.32)$$

As shown in Fig. 2.6 for a laser tuned to a frequency below the atomic resonance ($\Delta < 0$), the one-dimensional (1D) molasses exerts a force in the direction opposite of the direction of motion. As the saturation intensity of the laser increases, the force grows in strength and extends over a larger velocity space. If we expand Eqn. 2.32 about $v_A = 0$, we find the force simplifies to a linear velocity dependence:

$$\overrightarrow{F} \cong \frac{8\hbar k^2\Delta S_0}{\Gamma\left[\left(\frac{2\Delta}{\Gamma}\right)^2 + S_0 + 1\right]^2}\overrightarrow{v_A} \equiv -\alpha\overrightarrow{v_A} \quad (2.33)$$

with a damping coefficient α. For negative laser detuning, the force opposes the velocity regardless of the direction of motion, unlike the dipole force discussed in Section 2.1 which is strictly conservative. This is a classical, frictional force is

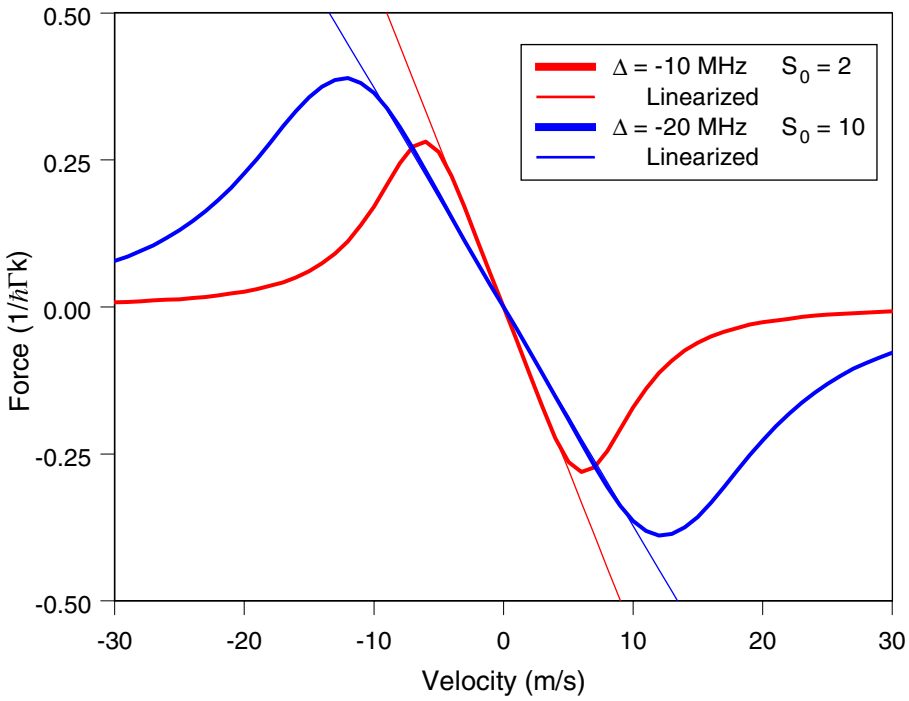

Figure 2.6: The radiation pressure force for 1D optical molasses for $\Delta = -10$ MHz, $S_0 = 2$ and $\Delta = -20$ MHz, $S_0 = 10$. The thin lines show the linear approximation for small values of v.

similar to that exerted on an object moving through a vat of molasses, hence the unusual name for this environment.

The range of captured velocities for a 1D optical molasses depends upon the detuning and intensity of the molasses lasers. For atoms with $|v| < v_{cap}$, the molasses force is strong enough to damp the atomic kinetic energy. Outside the capture velocity, the atoms remain unchanged. Here, we define v_{cap} to be the velocity at which the molasses force drops to 10% of the maximum value. It is

straightforward to show that the v_{cap} is

$$v_{cap} = \frac{1}{|k_L|}\left(-\Delta + \frac{3}{2}\Gamma\sqrt{S_0+1}\right). \tag{2.34}$$

For the case of sodium, for $\Delta = -15$ MHz and $S_0 = 10$, the $v_{cap} \approx 35\,\mathrm{m/s}$. It is important to note that the range of atomic velocities subject to the molasses force is significantly larger than the range where the linear force approximation is valid. However, once the atoms are captured and slowed such that $v_A < \left|\frac{\Delta}{k_L}\right|$, the linear approximation holds.

Under the influence of the cooling force for optical molasses expressed in Eqn. 2.33, the atoms slow to zero velocity and therefore zero temperature, a clearly unrealistic result. The random nature of absorption and emission continuously supplies kinetic energy to and heats the ensemble because of random recoil fluctuations [27]. While the random emission allows us to slow the atoms, it limits the ultimate attainable temperature. The heating rate is given by

$$\left.\frac{dE}{dt}\right|_{heat} = \frac{\hbar^2 k_L^2}{m}\left\langle\frac{dN_{photon}}{dt}\right\rangle_L \tag{2.35}$$

where the rate of photon scattering $\left\langle\frac{dN_{photon}}{dt}\right\rangle_L$ is defined with Eqn. 2.19. The rate of cooling is the product of the cooling force (Eqn. 2.33) and the atomic velocity

$$\left.\frac{dE}{dt}\right|_{cool} = -\alpha v_A^2. \tag{2.36}$$

At equilibrium, the heating rate and cooling rate sum to zero and results in the following equilibrium condition for v_A^2 [27]:

$$v_A^2\big|_{eq} = \frac{\hbar\Gamma^2}{16m\Delta}\left[\left(\frac{2\Delta}{\Gamma}\right)^2 + S_0 + 1\right]. \tag{2.37}$$

The minimum value for v_A^2 occurs for the case of low laser intensity ($S_0 \ll 1$) and a laser detuning Δ equal to half the natural linewidth; under these conditions,

the minimum value of v_A^2 is $\hbar\Gamma/4m$. The minimum rms velocity $\langle v \rangle_D$ for sodium under these conditions is 30 cm/s. If we equate the kinetic energy and the thermal energy of for one degree of freedom as discussed in Section 2.1, we see that the minimum temperature, often called the Doppler limit, is

$$T_D = \frac{\hbar\Gamma}{2k_B}. \tag{2.38}$$

For sodium, T_D is 240 μK. The Doppler limit only turns out to be a characteristic temperature, in fact sub-Doppler cooling mechanisms can further reduce the temperature of the ensemble and will be discussed below.

In addition to damping velocity in one dimension, two- or three-dimensional cooling can be produced with additional pairs laser beams and modeled with three pairs of orthogonal 1D molasses. Two-dimensional (2D) cooling can be used to damp the transverse velocity and decrease the divergence of a beam of atoms without disturbing the longitudinal component of velocity of the flux. The technique of optical collimation, as 2D cooling is known, is described in detail in Chapter 3. Three pairs of orthogonal counter-propagating beams produces a molasses where a damping environment is set up at the intersection of the three beams; this was first demonstrated at AT&T Bell Laboratories in 1985 [28]. At the center, a damping force is exerted on the atom regardless of the velocity direction. An ensemble of cold atoms will collect at the intersection, but because the force is only dissipative and contains no spatially dependent restoring component, atoms are not contained in a well-defined potential and may diffuse outside of the molasses region.

2.3.3 Magneto-Optical Trap

A magneto-optic trap (MOT) [29] uses magnetic fields in conjunction with optical molasses to spatially confine cooled atoms. While not used in the course of the work in this thesis, the MOT is a fundamental tool in many cold and ultracold collision experiments and is included here for background and completeness. As with optical molasses, the essential physics can be described in a 1D model that suffices to describe the main features of the operation.

Consider a linear magnetic field with a value of zero at $z = 0$ and a gradient of $\frac{dB}{dz}$. If an atom has a ground state angular momentum value of $\mathbf{J} = 0$ and an excited state $\mathbf{J} = 1$, the levels split according to Eqn. 2.25 as shown in Fig. 2.7a. Two counter-propagating laser beams, detuned Δ from the atomic resonance, illuminate the ensemble of atoms. The polarization of the laser beams must be appropriately chosen to meet the atomic selection rules; σ^+ for $\Delta M_{\mathbf{J}} = +1$ and σ^- for $\Delta M_{\mathbf{J}} = -1$. The resulting force is the linear superposition from each laser beam, given by Eqn. 2.27

$$\overrightarrow{F}_{MOT} = \frac{\hbar\Gamma\overrightarrow{k_L}}{2}\left[\frac{S_0}{\left[\frac{2\left(\Delta-|k_L v_A|+\frac{\mu_{12}}{\hbar}\frac{dB}{dz}z\right)}{\Gamma}\right]^2+S_0+1} - \frac{S_0}{\left[\frac{2\left(\Delta+|k_L v_A|-\frac{\mu_{12}}{\hbar}\frac{dB}{dz}z\right)}{\Gamma}\right]^2+S_0+1}\right] \tag{2.39}$$

where the direction of the force is defined along the positive z-axis. Figure 2.7b shows the force as a function of position and velocity for typical MOT parameters. For small values of v and z, the equation of motion reduces to a damped harmonic

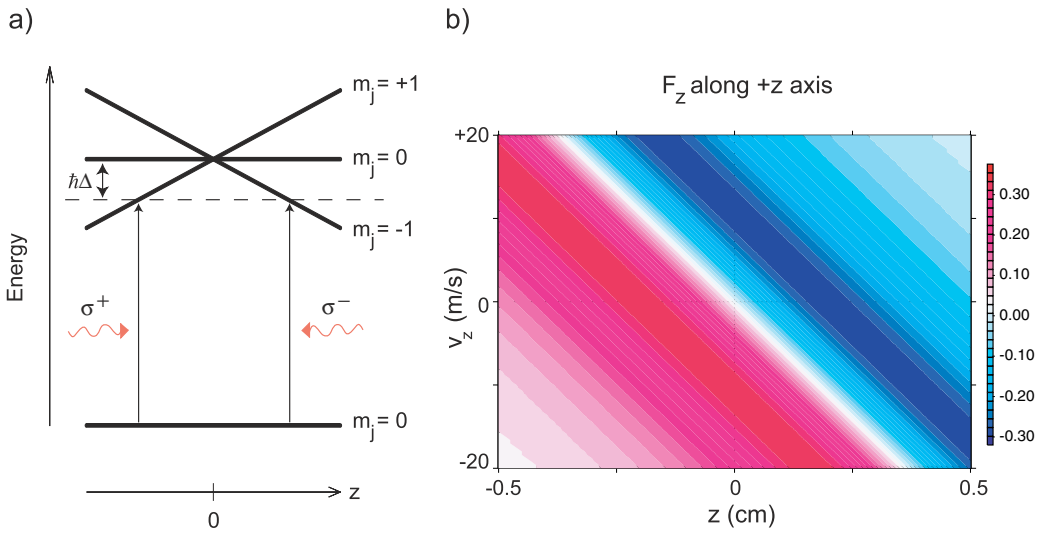

Figure 2.7: a) Zeeman Splitting of atomic levels. b) Contour diagram of the radiation pressure force as a function of position and velocity. Red indicates a force along the positive z-axis and blue along the negative z-axis.

oscillator

$$\overrightarrow{F}_{MOT} = -\alpha \overrightarrow{v} - \beta \overrightarrow{z} \tag{2.40}$$

where the damping coefficient α is defined in Eqn. 2.33 and the restoring coefficient β is given by

$$\beta = \frac{\mu_{12} \frac{dB}{dz}}{\hbar |k|} \alpha. \tag{2.41}$$

Under typical laboratory conditions, where $v_A \to 0$ and $z \to 0$ the atom behaves dynamically like an overdamped harmonic oscillator with a restoring time τ_{MOT} on the order of a few milliseconds.

The 1D MOT model can be implemented in 3D with three pairs of orthogonal, counter-propagating laser beams. A pair of current carrying coils operating in an

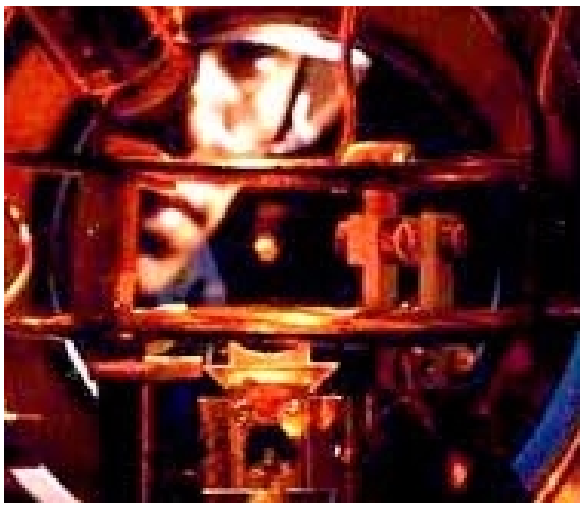

Figure 2.8: Picture of a sodium MOT (courtesy of NIST).

anti-Helmholtz configuration generates a quadrupole magnetic field near the trap center. At the center of the coils, the magnetic field increases linearly from zero in all directions to produce the appropriate field shape. However, the magnetic field slope at the trap center is not the same along the coil axis and the symmetry plane. Atoms in a MOT are usually confined to a cloud a few millimeters in diameter with densities $\sim 10^{10}$ atoms/cm^3. Typical MOT temperatures are near the Doppler limit T_D. Figure 2.8 shows a sodium MOT at the National Institute of Standards and Technology. In addition to a trapping in three dimensions, MOTs operating in two dimensions focus and compress atomic beams [30, 31].

2.4 Mechanical Effects of Light III: Sub-Doppler Cooling

Early experimental realizations of three-dimensional optical molasses reported temperatures near the Doppler limit. However, a detailed study of optical molasses at the National Bureau of Standards (now National Institute of Standards and Technology - NIST), using multiple methods to measure the temperature of a 3D sodium molasses, reported values significantly lower than T_D [32]. Typical temperatures of 45 μK were an order of magnitude lower than the 240 μK Doppler limit predicted by the radiation pressure theory. Figure 2.9 shows the fluorescence signal from a time-of-flight technique used at NIST along with numerically predicted signals for 240 μK and 40 μK.

The Doppler cooling theory, as pleasing and simple as it is, fails to accurately predict the ultimate temperature of optical molasses. Additional damping mechanisms exist that further cool the ensemble to sub-Doppler temperatures. The sub-Doppler forces arise from optical pumping and light shifts from the near-resonant interactions between light and the atoms dependent on optical polarization and internal atomic structure (i.e. hyperfine structure) not considered in the Doppler-limited cooling model [33].

The state of optical polarization used to generate an optical molasses is rather flexible. The two primary optical polarization arrangements are $lin \perp lin$ and σ^+-σ^-, referring to the state of polarization of the counter-propagating laser beams. In $lin \perp lin$ molasses, each counter-propagating laser beam is linearly polarized, but perpendicular to each other. The laser beams in a σ^+-σ^- molasses have circular polarization of opposite handedness. The sub-Doppler cooling

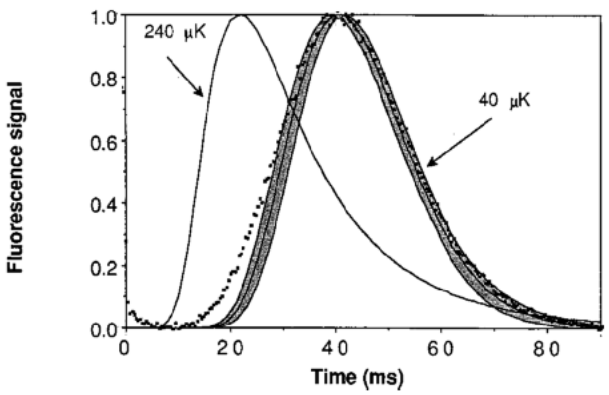

Figure 2.9: Time-of-flight fluorescence data and calculations (40 μK and 240 μK) for atoms released from a 3D optical molasses. The shaded region about 40 μK is the uncertainty due to system geometry (from Ref. [32]).

mechanisms differ but both arise from light shifts and optical pumping.

Counterpropagating laser beams in the $lin \perp lin$ arrangement establishes a rotating polarization pattern when the electric fields add together as shown in Fig. 2.10. Over a distance of half a wavelength of light (along z), the electric fields of each beam add up in a pattern that shifts from linear (at an angle 45° from x in $x-y$ plane) to circular (σ^+) to linear (90° from original) to circular (σ^-). The transition selection rules dictate that within the region where the polarization appears to be σ^+ (σ^-), $\Delta\mathbf{J} = +1$ (-1). However, when the atoms decay from the excited state, $\Delta\mathbf{J}$ can be ± 1 or 0. The rotating polarization also results in ground-state energy shifts due to interactions between the atom and the light field (Fig. 2.10). The ground state atomic energy shifts by an amount

$$\Delta\varepsilon_1 = \frac{\hbar\Delta S_0 C_{12}^2}{1 + (2\frac{\Delta}{\Gamma})^2} \tag{2.42}$$

where C_{12} is the Clebsch-Gordon coefficient for the transition from the ground state to the excited state. The Clebsch-Gordon coefficient depends on the po-

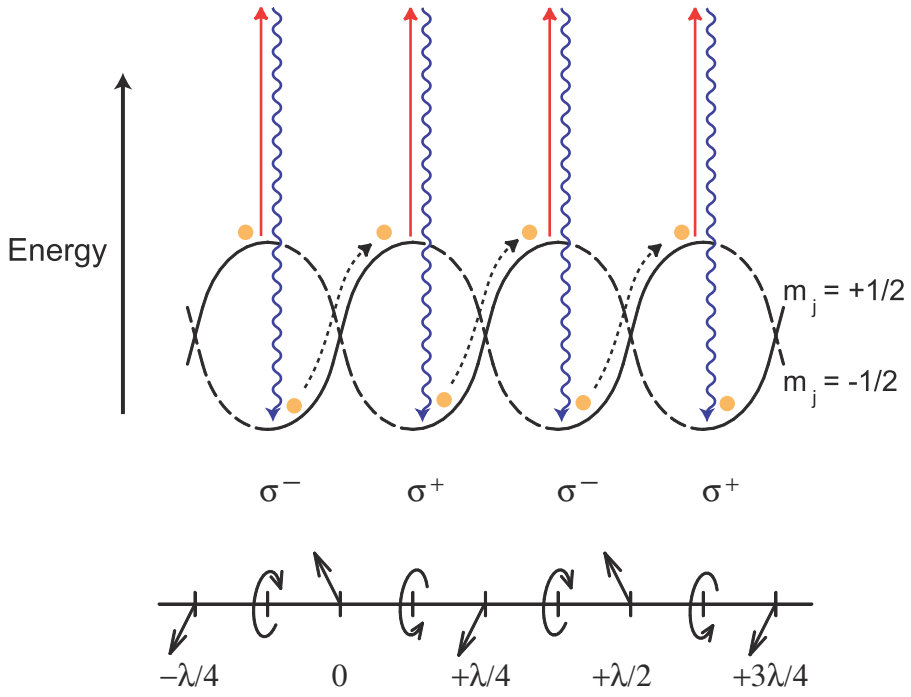

Figure 2.10: *Lin* $\perp$ *lin* cooling mechanism. The rotating polarization introduces spatially dependent light shifts for the different ground states. Fast atoms are optically pumped to a lower energy state and the extra energy is carried away with the decaying photon, slowing the atoms in the process.

larization of the field as well as the initial and final states in the transition. The simplest model for *lin* $\perp$ *lin* cooling is an atom with a ground state $|1, \mathbf{J}_1 = \frac{1}{2}\rangle$ and excited state $|2, \mathbf{J}_2 = \frac{3}{2}\rangle$. Because of the changing polarization and the effect it has on C_{12}, the ground state energy shifts periodically for each magnetic sublevel, $M_1 = \pm\frac{1}{2}$ as shown in Fig. 2.10. Consider an atom in the $M_1 = 1/2$ state; if it has sufficient kinetic energy to move to the position of its local energy maximum, it may absorb a photon from the σ^- polarized field, populating the excited state $M_2 = -1/2$. The states allowed to be populated by decay

are $M_1 = +1/2$, with no net change in energy, or $-1/2$, where the atom emits a photon of greater energy than it absorbed. The difference in photon energy comes at the expense of atomic kinetic energy. A similar cycle occurs for an atom in the $M_1 = -1/2$ state. The climbing of the hills and losing energy via optical pumping to a different ground state continuously removes energy from the ensemble and slows down the atoms. The process is called Sisyphus cooling, as it is reminiscent of the mythological figure of Sisyphus, who was condemned to push a boulder up a hill, only to have it roll back to the bottom when he reached top.

While the details of the theory are beyond the scope of this thesis, it can be shown that the average force for atoms near zero velocity is

$$\overrightarrow{F}_{lin\perp lin} \simeq -\alpha' \overrightarrow{v} \tag{2.43}$$

where the $lin \perp lin$ friction coefficient α' is $-3\hbar k_L^2(\Delta/\Gamma)$. For a typical 1D optical molasses in sodium (with $\Delta = -1.5\Gamma$ and $S_0 = 10$), the $lin \perp lin$ friction coefficient α' is 15 times larger than the radiation pressure damping constant α. But, the velocity for the maximum $lin \perp lin$ force is

$$v_{\max} = \frac{\Gamma}{9k_L} \frac{S_0}{(2\Delta/\Gamma)^2 + 1} \tag{2.44}$$

and equals 0.65 m/s, indicating that the atoms must be precooled by the radiation pressure force before sub-Doppler $lin \perp lin$ cooling occurs.

The theoretical minimum momentum in 1D $lin \perp lin$ cooling equals the momentum from the recoil of a single photon $\hbar \left| \overrightarrow{k_L} \right|$, corresponding to a recoil temperature T_R given by

$$T_R = \frac{\hbar^2 \left| \overrightarrow{k_L} \right|^2}{2mk_B}. \tag{2.45}$$

For sodium, T_R equals 1.2 μK. However, in real atoms the typical 3D molasses temperatures are usually a factor of $5-20$ greater than T_R because of the higher dimensionality and more complicated atomic structure.

The other arrangement for optical molasses, σ^+-σ^-, has similar cooling processes that rely on combinations of light shifts and polarization effects, but is beyond the scope of this thesis. The force again has a linear dependence on velocity for atoms near $v = 0$:

$$\overrightarrow{F}_{\sigma^+-\sigma^-} \approx -0.8\hbar k^2 v \tag{2.46}$$

for $\Delta \simeq \Gamma$. While the ultimate temperature of σ^+-σ^- is nearly the same as $lin \perp lin$, a $lin \perp lin$ molasses cools atoms in a shorter amount of time because the damping coefficient is approximately a factor of four larger. This will become an important point when using a optical molasses to collimate an atomic beam. It is difficult to characterize a capture velocity for the σ^+-σ^- cooling process because it connects smoothly with the radiation pressure force as the velocity moves away from zero.

2.5 Discussion of Laser Cooling

Here we have discussed four different radiation induced forces: the dipole trapping force, the radiation pressure force, and the two sub-Doppler forces: $lin \perp lin$ and σ^+-σ^-. Table 2.1 summarizes the details of these forces. At this point, they have been presented in very simple terms: typically in one dimension and with the angular momentum states chosen to simplify the mathematics. Real atoms are by far more involved: hyperfine structure, scattered light, stray magnetic fields, polarization impurities, and other effects complicate the cooling process. Some

Force	Nature	Characteristic Velocity	Frictional Coefficient
Dipole	Conservative	$< \sqrt{\frac{2}{m}U_{trap}}$	-NA-
Scattering	Non-conservative	$\left\lvert\frac{\Delta}{k_L}\right\rvert$	$\frac{8\hbar k^2\lvert\Delta\rvert S_0}{\Gamma\left[\left(\frac{2\Delta}{\Gamma}\right)^2+S_0+1\right]^2}$
$Lin \perp lin$	Non-conservative	$\frac{\Gamma}{9k_L}\frac{S_0}{(2\Delta/\Gamma)^2+1}$	$3\hbar k_L^2(\frac{\lvert\Delta\rvert}{\Gamma})$
σ^+-σ^-	Non-conservative	-NA-	$0.8\hbar k_L^2$

Table 2.1: Summary of radiation forces: dipole, scattering (1D optical molasses), $lin \perp lin$, and σ^+-$\sigma-$. The characteristic velocity for the dipole is the maximum trapped velocity while for the other forces it is the velocity at which the force is maximum.

of these effects will be mentioned in more detail in Section 3.2 in the following chapter.

Chapter 3

Experimental System

Critical to any experiment involving laser cooling is the laser system, which is described in Section 3.1. Section 3.2 describes the structure of atomic sodium and how it, as a real atom, is laser cooled. Several spectroscopic techniques used to tune and reference the laser frequency are described in Section 3.3. Electro-optic elements used to shift laser frequencies are presented in Section 3.4 The high vacuum system that contains the experiment is discussed in Section 3.5. Section 3.6 summarizes the detection techniques used during the experiments.

3.1 Laser and Optical System

The work described in this thesis depends critically on the lasers; as many as four lasers are used at any time during any of the experiments. All of the lasers used in this experiment are continuous wave (cw) lasers, meaning that the output from the laser is not pulsed. To obtain an output frequency bandwidth $\delta\omega_L$ less than 1 MHz, only cw lasers can be used because the Fourier transform limited

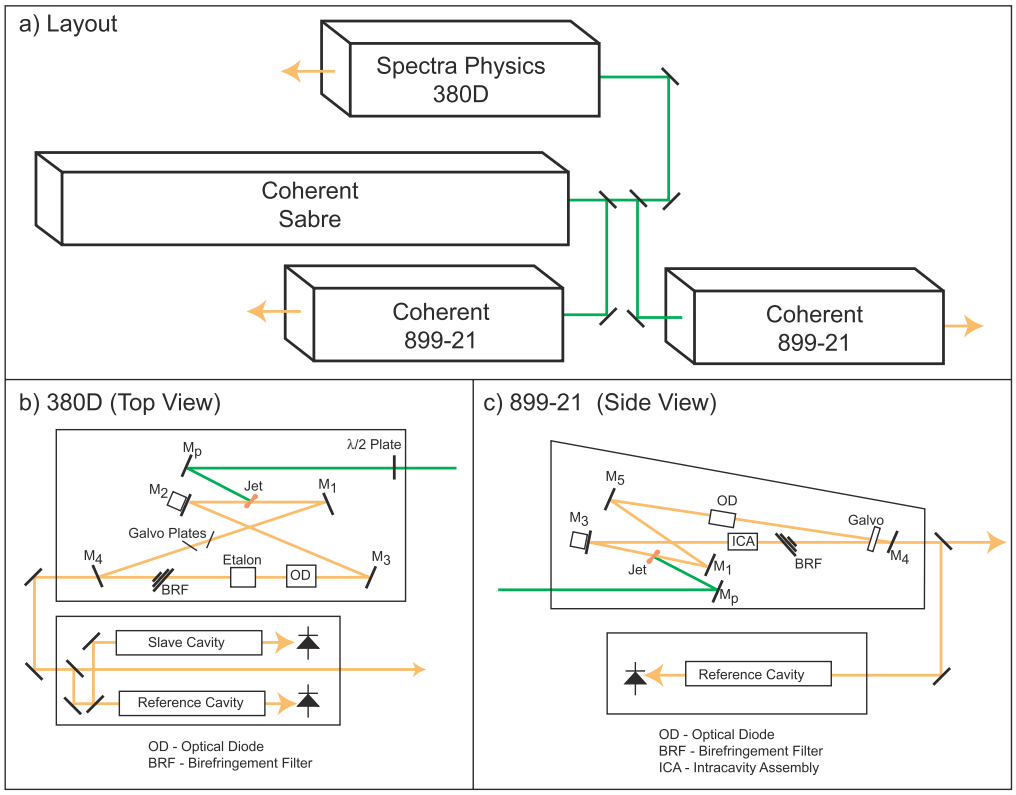

Figure 3.1: Laser system for the experiment. The argon-ion laser pumps the three dye lasers used in this work. One of the ring dye lasers is a Spectra-Physics 380D ring dye laser with a horizontal ring alignment. The other two dye lasers are Coherent 899-21 ring dye lasers. All lasers run with Rhodamine 6G solution (2×10^{-3} molar in ethylene glycol).

bandwidth of pulsed lasers

$$\delta\omega_L \approx \frac{4\pi}{\tau_{pulse}} \tag{3.1}$$

greatly exceeds the 1 MHz limit. For a 1 ns pulse (a rather long pulse compared to state of the art femtosecond lasers), $\delta\omega_L$ is on the order of several hundred MHz. However, cw lasers do not passively operate at the desired 1 MHz bandwidth, multiple cavity modes may simultaneously lase and intracavity jitter broadens $\delta\omega_L$. Mode selecting elements, typically etalons, and active stabilization techniques are needed to narrow the laser bandwidth. Of the four lasers used, three are single frequency ring dye lasers. The forth is an argon-ion laser, which powers the dye lasers.

We use a Coherent Sabre argon-ion laser providing up to 25 W of continuous output of light, primarily at wavelengths of 514 and 488 nm (nominally 50% and 45%, respectively) as the dye-pumping laser. A ceramic tube containing argon gas is ionized by an anode and cathode mounted on opposite ends of the tube. After the tube ionizes, a nominal voltage of 505 V maintains the ionization. A closed loop water cooling system dissipates the heat generated by the plasma. The output power is controlled by adjusting the current through the tube up to the maximum tube current of 55 A; usually 49 A are required to produce the 22 W needed to power the three dye lasers. The argon-ion laser beam quality is crucial to the performance of the dye lasers, a TEM_{00} transverse mode is essential for dye laser stability. The quality of the mode improves as the diameter of an intracavity aperture is reduced, but is accompanied by a drop in output power. Failure to maintain clean optics within the laser prevents TEM_{00} output. Internal systems stabilize the output power and pointing stability after a brief warm-up period ($\sim$ 1 hour). Dielectric coated beamsplitters and mirrors distribute the

output light from the argon laser to the dye lasers as shown in Fig. 3.1a.

Two different models of ring dye lasers are used. The Spectra-Physics 380D is a ring dye laser oriented with the ring in a horizontal configuration (Fig. 3.1b). The gain medium is a solution of rhodamine 6G (R6G) dye dissolved in ethylene glycol ($\sim 2 \times 10^{-3}$ molar). The dye circulates through a chiller that cools the solution to 10° C before passing through a high pressure jet within the cavity. The jet is perpendicular to the laser oscillation plane. Cooling the dye decreases the frequency of stability reducing air bubbles. The argon ion beam is focused by a curved mirror onto a vertically oriented dye jet, and oscillation occurs in a "figure-8" pattern between the cavity mirrors, with a beam propagating in each direction. Placing an optical diode (OD) in the path rotates the field polarization for one direction. The rotated polarization leads to cavity loss for and suppresses oscillation for the rotated beam. A birefringent filter (BRF) is the course tuning element that selects the center wavelength λ_L with a bandwidth $\delta\omega_L \sim 25$ GHz. A low-finesse intra-cavity etalon reduces the linewidth to a single longitudinal mode that is broadened to about 10 MHz because of intracavity jitter. The laser operates in single frequency by actively stabilizing the cavity to remove this jitter. A portion of the output beam passes through a pair of thermally stabilized, low-finesse cavities (10 GHz and 500 MHz). A servo-loop monitoring the cavity fringe voltage locks the laser to a single frequency by adjusting the voltage applied to a piezo upon which one of the cavity mirrors is mounted. The laser is scanned (up to 20 GHz) by electronically controlled rotation of a pair of galvo plates to increase the optical pathlength, thereby shifting the laser frequency. Typical output for the 380D, pumped with 5.5 W from the argon ion laser, is 300 mW at 589 nm with a 1 MHz bandwidth.

The remaining two dye lasers are Coherent 899-21 lasers, operating with similar R6G dye solutions. The 899-21 employs a vertical cavity (Fig. 3.1c), also in a figure-8 pattern. The cavity elements are similar, an optical diode limits the oscillation to a single direction and a birefringent filter ($\delta\omega_L \sim 2$ GHz) provides the course tuning of the laser. An intracavity assembly (ICA) contains pair of etalons that reduce the linewidth to a single longitudinal mode with a linewidth of 10 MHz. Active stabilization and single frequency operation are obtained by locking the laser to the fringes of an external reference cavity via feedback to a piezo-driven mirror in the cavity. A single galvo plate is used to scan the laser (up to 30 GHz). Output power of $400 - 500$ mW at 589 nm ($\delta\omega_L \sim 1$ MHz) is possible when pumped with 6 W from the argon-ion laser.

3.2 Atomic Sodium

Sodium is one of the most studied atomic species (it was the first species to be cooled and trapped) because of its simple structure, abundance in nature, and the availability of commercial single frequency lasers at the resonant transition. The only stable isotope is ^{23}Na, although unstable isotopes produced from accelerators have also been cooled and trapped [1]. An understanding of the structure of sodium is fundamental to understanding how real atoms with multiple levels are optically cooled.

3.2.1 Atomic States

The ground state configuration is a closed shell surrounded by a single valence electron in an s-state, [Ne]$3s^1$. The single electron structure is similar to hydro-

gen, but interactions between the electron core and the valence electron break the degeneracy within the shells defined by the principle quantum number n. Each n shell splits into $n-1$ subshells, each one characterized by the orbital quantum number l. The subshells order with increasing value of l, hence $l=0$ is lower in energy than $l=1$. The levels are named with spectroscopic notation

$$n\ ^{2\mathbf{S}+1}\mathbf{L_J} \tag{3.2}$$

where $\mathbf{S}$ is the total electron spin, $\mathbf{L}$ is the total orbital angular momentum (historically labeled by $\mathbf{L}=S,P,D,\ldots$ for $\sum l=0,1,2,\ldots$), and $\mathbf{J}$ is the total electronic angular momentum. The possible values of $\mathbf{J}$ are the vector sums of $\mathbf{L}$ and $\mathbf{S}$: $\mathbf{J}=|\mathbf{L}-\mathbf{S}|,|\mathbf{L}-\mathbf{S}+1|,\ldots,|\mathbf{L}+\mathbf{S}|$. The *core* electrons have total spin and orbital angular momentum equal to zero, and therefore $\mathbf{S}$ and $\mathbf{L}$ are given solely the single valence electron: $\mathbf{S}=1/2$ and $\mathbf{L}=l$. The spectroscopic labels are $3\ ^2S_{1/2}$ for the ground state and $3\ ^2P_{1/2,3/2}$ for the first excited level. The energy between the levels is 2.1 eV, requiring a photon with wavelength $\lambda=589$ nm to drive the transition.

Interactions between the electron spin and orbital angular momentum further perturb the system. The orbiting electron generates a magnetic field that, in turn, interacts with the electron spin

$$U_{so}=-\overrightarrow{M_{\mathbf{S}}}\cdot\overrightarrow{B} \tag{3.3}$$

where $\overrightarrow{M_{\mathbf{S}}}$ is the magnetic moment of the electron (which is proportional to the spin operator) and $\overrightarrow{B}$ is the field produced by the moving electron. After evaluating the first order perturbation contribution of the spin-orbit coupling, a level with total angular momentum $\mathbf{J}$ and orbital momentum $\mathbf{L}$ shifts by an

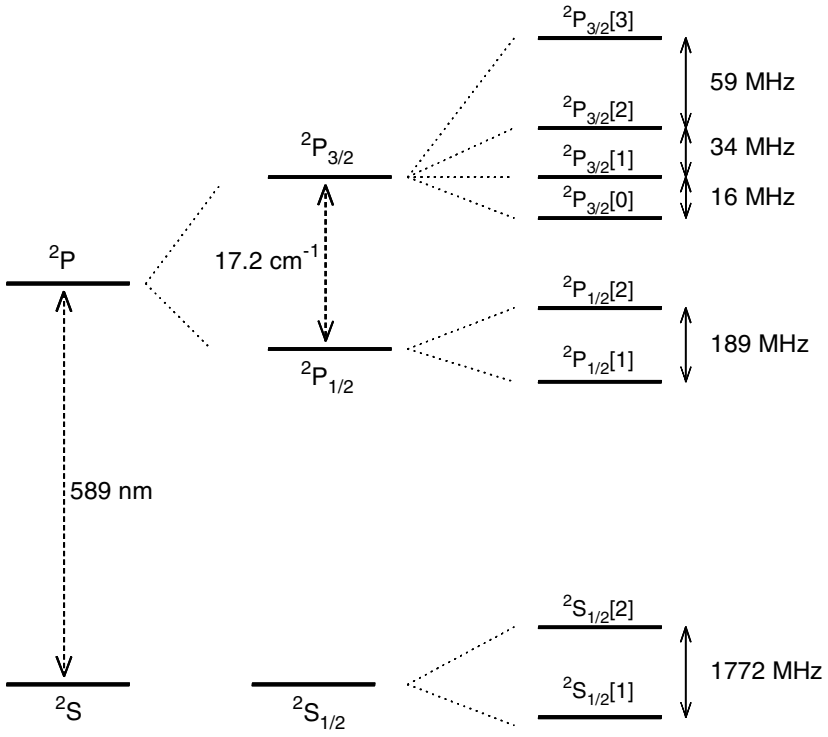

Figure 3.2: Atomic energy level diagram for ^{23}Na.

amount equal to

$$\Delta\varepsilon_{SO,J} = \xi_{n,l}(\mathbf{J}^2 - \mathbf{L}^2 - \mathbf{S}^2) \tag{3.4}$$

where $\xi_{n,l}$ is a constant proportional to $\left\langle n,l|\frac{1}{R^3}|n,l\right\rangle$ [34]. The spin-orbit shift breaks the degeneracy of the $\mathbf{L}$ levels by dividing them into levels labeled by the total angular momentum $\mathbf{J}$. The radial dependence of $\xi_{n,l}$ indicates that spin-orbit splitting is larger for low lying levels nearer the nucleus. In sodium, the lower the value of $\mathbf{J}$, the lower the energy (for a common $\mathbf{L}$). Therefore, 3 $^2P_{1/2}$ is lower in energy than 3 $^2P_{3/2}$, as seen in Fig. 3.2. The energy difference between the 3 ^2P levels is 17.2 cm^{-1}. The splitting between these levels is the

source of the D1 ($3\ ^2S_{1/2} \longrightarrow 3\ ^2P_{1/2}$) and D2 ($3\ ^2S_{1/2} \longrightarrow 3\ ^2P_{3/2}$) lines in the doublet emission of sodium lamps.

The nucleus of ^{23}Na, made of 11 protons and 12 neutrons, has a total nuclear spin $\mathbf{I} = 3/2$. Hyperfine splitting $\Delta\varepsilon_{HF}$ arises from interactions between the nuclear spin $\mathbf{I}$ and the electronic angular momentum $\mathbf{J}$; $\mathbf{I}$ and $\mathbf{J}$ sum as vectors to the total angular momentum $\mathbf{F}$: $\mathbf{F} = |\mathbf{J} - \mathbf{I}|, \ldots, |\mathbf{J} + \mathbf{I}|$). While the splitting between hyperfine levels is much smaller in magnitude (< 0.1 cm^{-1}) than the fine structure splitting, the hyperfine structure is well within the resolution of single frequency lasers and plays an important role in laser cooling and trapping. Because of the need to identify hyperfine states, we modify spectroscopic notation to include $\mathbf{F}$

$$n\ ^{2\mathbf{S}+1}\mathbf{L}_{\mathbf{J}}\ [\mathbf{F}]. \tag{3.5}$$

The notation of Eqn. 3.5 will be used throughout this thesis, and will be modified only by the inclusion of the angular momentum projection $M_{\mathbf{F}}$ inside the brackets $[\mathbf{F}, M_{\mathbf{F}}]$ in the cases where it is important to the physics. The commonly used cycling transition for laser cooling is $3\ ^2S_{1/2}\ [2] \longrightarrow 3\ ^2P_{3/2}\ [3]$, for zero magnetic field. The labeling of the levels becomes more complicated in the presence of magnetic fields when the levels split due to the Zeeman effect.

3.2.2 Zeeman Splitting

While the Zeeman effect is treated as an atomic perturbation, the importance of the splitting of levels is not to be taken lightly. Seemingly mild magnetic fields ($B \sim 50$ G) induce shifts that overwhelm the hyperfine structure. For this reason, one must proceed carefully when calculating Zeeman shifts, the appropriate basis

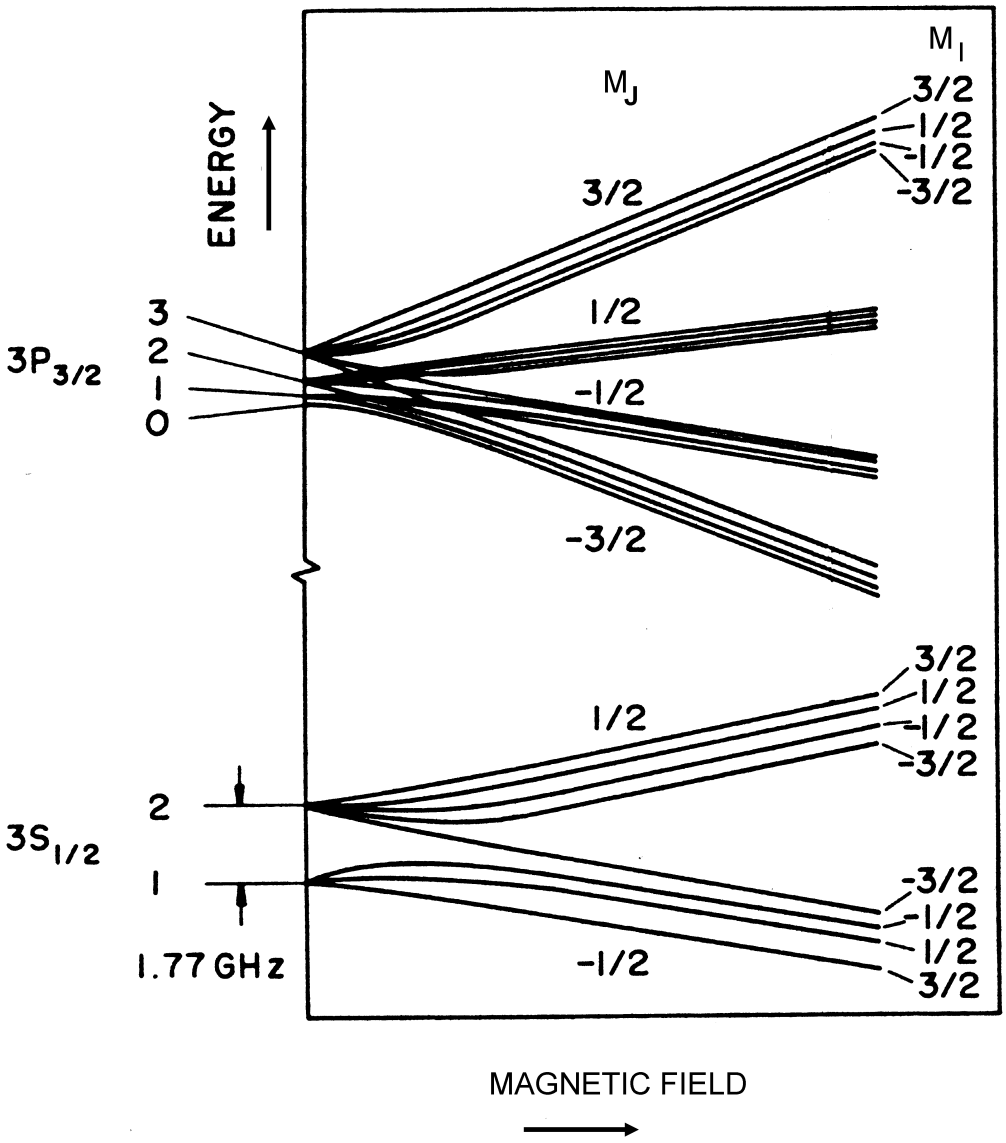

Figure 3.3: The Zeeman effect on the 3 $^2S_{1/2}$ ground state and 3 $^2P_{3/2}$ excited state of atomic sodium. For weak fields, the hyperfine states degeneracy is broken as the states are shifted by an amount proportional to $M_{\mathbf{F}}B$. As the field increases, $M_{\mathbf{F}}$ fails to be a good quantum number and the states become proportional to $M_{\mathbf{J}}B$.

set is important. Recall the general form of the Zeeman shift of energy levels given by Eqn. 2.25

$$\Delta\varepsilon_M = gM\mu_B B. \tag{2.25}$$

Assume a magnetic field that is sufficiently weak that the Zeeman shifts $\Delta\varepsilon_{M_\mathbf{F}}$ are much smaller than the hyperfine shifts $\Delta\varepsilon_{HF}$. For such a field, $\mathbf{F}$ and $\mathrm{M_F}$ are good quantum numbers. In this case the Landé factor g equals $g_\mathbf{F}$ where

$$g_\mathbf{F} = g_\mathbf{J}\frac{\mathbf{F}(\mathbf{F}+1)+\mathbf{J}(\mathbf{J}+1)-\mathbf{I}(\mathbf{I}+1)}{2\mathbf{F}(\mathbf{F}+1)} \tag{3.6}$$

and

$$g_\mathbf{J} = 1+\frac{\mathbf{J}(\mathbf{J}+1)+\mathbf{S}(\mathbf{S}+1)-\mathbf{L}(\mathbf{L}+1)}{2\mathbf{J}(\mathbf{J}+1)}. \tag{3.7}$$

For the $3\ ^2P_{3/2}$ [3] state, $g_\mathbf{F} = 2/3$ and $g_F = 1/2$ for $3\ ^2S_{1/2}$ [2] in atomic sodium. The splitting of the hyperfine levels in sodium is shown in the left hand edge of Fig. 3.3. The energy for the $3\ ^2S_{1/2}$ $[2, M_{\mathbf{F}_1}]$ to $3\ ^2P_{3/2}$ $[3, M_{\mathbf{F}_2}]$ transition equals (from Eqn. 2.26)

$$\Delta E = \hbar\omega_0 + \left(3\cdot M_{\mathbf{F}_2} - 2\cdot M_{\mathbf{F}_1}\right)\mu_B B \tag{3.8}$$

where the weak-field magnetic frequency shift $\frac{\mu_{12}}{\hbar}$ (in units Hz/G) equals $\frac{\mu_B}{\hbar}\left(3\cdot M_{\mathbf{F}_2} - 2\cdot M_{\mathbf{F}_1}\right)$.

As the magnetic field strength increases, the Zeeman shifts become comparable to and then exceed the hyperfine shifts and the basis set must be changed such that $\mathbf{J}$ and $M_\mathbf{J}$ are good quantum numbers and the hyperfine splitting is a secondary perturbation. For the sake of clarity, fields of this magnitude are defined as moderate. For moderate fields, the Landé factor $g = g_\mathbf{J}$ and $M_\mathbf{J}$ are used to calculate the Zeeman shifts $\Delta\varepsilon_{M_\mathbf{J}}$. The values of $g_\mathbf{J}$ are 2 and 4/3 for

the $3\ ^2S_{1/2}$ and $3\ ^2P_{3/2}$ states, respectively. Hyperfine structure perturbs the Zeeman split levels as a function of $M_{\mathbf{I}}$. The right hand side of Fig. 3.3 shows this regime. For this moderate field, the $3\ ^2S_{1/2}\ [M_{\mathbf{J}}] \longrightarrow 3\ ^2P_{3/2}\ [M_{\mathbf{J}}]$ transition energy equals

$$\Delta E = \hbar\omega_0 + \left(\frac{3}{2}\cdot M_{\mathbf{J}_2} - \frac{1}{2}\cdot M_{\mathbf{J}_1}\right)\mu_B B = \hbar\omega_0 + \mu_{12}B. \tag{3.9}$$

The transition from the weak regime to moderate regime is smooth as the different basis sets mix together as seen in the middle of Fig. 3.3.

3.2.3 "Real" Laser Cooling

In Chapter 2, laser cooling theory is presented in terms of a "two-level" model. While we introduced angular momentum and Zeeman splitting, the possibility of atoms populating more than the two levels in the cooling cycle was excluded. However, in real atomic systems, additional energy levels play an important role. The Zeeman splitting of real atoms becomes complicated. A discussion of the physics involved in real laser cooling is presented here.

There is a significant probability that atoms will populate levels outside of the cooling cycle in an optical molasses. The molasses laser beam is typically detuned -15 MHz below the $3\ ^2S_{1/2}\ [2] \longrightarrow 3\ ^2P_{3/2}\ [3]$ atomic resonance. As shown in Fig. 3.2, this frequency is only 45 MHz from the $3\ ^2S_{1/2}\ [2] \longrightarrow 3\ ^2P_{3/2}\ [2]$ transition. Because of the high intensity of the optical field in the molasses region ($\sim$ 150 mW/cm^2 total intensity for the molasses described herein), the transitions are significantly power broadened and the off-resonance absorption probability increases. The relative absorption probability of the two excited states can be estimated using a two-level model for each transition. With the laser tuned 15 MHz below the desired transition, the probability of excitation to

the $3\ ^2P_{3/2}$ [2] level is only one third of that for the desired $3\ ^2P_{3/2}$ [3] level. From the $3\ ^2P_{3/2}$ [2] level, the atom decays to either the $3\ ^2S_{1/2}$ [2] or the $3\ ^2S_{1/2}$ [1] manifold. If it decays to $3\ ^2S_{1/2}$ [2], it remains in the cooling cycle. However, if it decays to $3\ ^2S_{1/2}$ [1], 1.7 GHz below $3\ ^2S_{1/2}$ [2] (Fig. 3.2), the atom exits the cooling cycle because the cooling laser frequency is well off of resonance. Left unchecked, all the atoms in the ensemble will eventually be optically pumped into this "dark" state by this process.

To prevent atoms from populating the dark ground state in optical molasses, a second laser frequency (1.7 GHz above the cooling frequency) added along with the cooling laser frequency *repumps* atoms from $3\ ^2S_{1/2}$ [1] to $3\ ^2P_{3/2}$ [2] as shown in Fig. 3.4a. Once in the $3\ ^2P_{3/2}$ [2] state, the atom can decay to $3\ ^2S_{1/2}$ [2] and re-enter the cooling cycle. The intensity of the repumper needs to be only about 10% of the cooling laser intensity. Figure 3.4b shows photographs of the fluorescence from two stages of optical molasses that collimate a sodium beam. In the upper photo, the repumper is on and the intensity of the upstream and downstream molasses stages are nearly equal. However, in the lower image where the repumper is turned off, the fluorescence downstream decreases, indicating that population is building up in the dark $3\ ^2S_{1/2}$ [1] state where they are out of the cooling (and fluorescence) cycle. A repumper must also be added to the laser beams in a MOT.

The Zeeman effect also plays an important role in real laser cooling. As discussed in Section 3.2.2, the basis set of atomic states depend upon the strength of the magnetic field. The typical laser cooling transition for the condition of a weak magnetic field is $3\ ^2S_{1/2}\ [2, M_{\mathbf{F}} = 2] \longrightarrow 3\ ^2P_{3/2}\ [3, M_{\mathbf{F}} = 3]$. This is a good transition because the σ^+ polarization of the cooling laser optically pumps

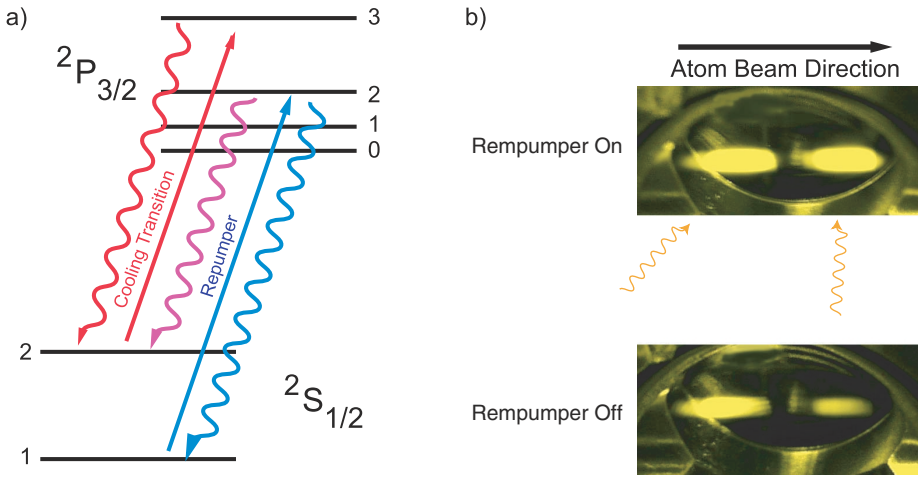

Figure 3.4: a) The level diagram of the repumping scheme. The repumper prevents population of the dark 3 $^2S_{1/2}$ [1] state. b) Photograph of fluorescence from optical molasses, with and without repumper, impinging on a sodium beam. The beam moves to the right and the flourescence seen comes from the x- and y-axis molasses beams as shown. The decrease in downstream molasses is the result of populating the 3 $^2S_{1/2}$ [1] state.

all the atoms to these states because the $\Delta M = +1$ selection rule drives the atoms to the stretched state ($|M_{\mathbf{F}}| = \mathbf{F}$). With the exception of the possibility of exciting the atom to the 3 $^2P_{3/2}$ [2] level, this cooling cycle is as close to a real two level system that exists. The magnetic frequency shift $\frac{\mu_{12}}{\hbar}$ for this transition in sodium is 1.4 MHz/G.

However, for moderate magnetic fields, $\mathbf{F}$ and $M_{\mathbf{F}}$ are bad quantum numbers, and $M_{\mathbf{J}}$ emerges as the good label. If σ^+ polarization is used in a moderate field environment the atoms will be pumped to the 3 $^2S_{1/2}$ $[M_{\mathbf{J}} = 1/2] \longrightarrow$ 3 $^2P_{3/2}$ $[M_{\mathbf{J}} = 3/2]$ stretched state cooling cycle. The frequency shift $\frac{\mu_{12}}{\hbar}$ is 1.4 MHz/G for this transition, the same as for the low field case. The equality of the shifts is not coincidental, the two transitions are equivalent but in different basis sets: the

Clebsch-Gordon coefficient connecting ${}^2S_{1/2}$ $[M_{\mathbf{J}} = 1/2]$ and ${}^2S_{1/2}$ $[2, M_{\mathbf{F}} = 2]$ is 1 (similarly for the ${}^2P_{3/2}$ excited states). The transition between the weak and moderate field cases is simple, a continuous linear response over both regions and can be seen in Fig. 3.3. Because the equality holds for the stretched state cooling cycle, a field dependent force can be changed from moderate to weak without fear of pumping the atom to a dark state. For the case of moderate fields, there is no need for a repumper laser because the cooling transitions are shifted well away from other possible transitions.

3.3 Frequency References

Laser cooling and collision studies critically depend on the laser frequencies, necessitating accurate frequency measurements. In the work presented in this thesis, all the frequencies are within a few GHz of the D2 sodium transition, so the sodium atom itself serves as the primary frequency standard. Because the transverse velocity of atoms within a beam is very low, a laser beam perpendicularly crossing the atom flux is a popular technique for high-resolution, fluorescence spectroscopy. The cross-beam spectra is used, in turn, to calibrate sodium saturated absorption spectra and molecular iodine fluorescence spectra that we use as secondary frequency standards. In the experiments described in Chapters 4 and 5, the secondary standards enable us to lock lasers to specific frequencies or scan them across a range of frequencies.

3.3.1 Crossed Beam Spectroscopy

An ensemble of atoms with a velocity distribution $n(v)$ leads to a heterogeneous spectral line-broadening because the laboratory frame laser frequency observed by each moving atom is Doppler shifted [7, 35] by an amount

$$\Delta\omega_D = -\overrightarrow{k_L} \cdot \overrightarrow{v_A}, \tag{2.21}$$

yielding a Doppler broadened absorption lineshape $D(\omega)$ of width $\delta\omega_D$ that increases with the velocity distribution. For a non-divergent laser beam, only atomic velocity components along the laser propagation axis lead to a Doppler shift $\Delta\omega_D$, the dot product in Eqn. 2.22 ensures zero broadening for orthogonal velocity components. Therefore, atoms in a collimated atom beam, with a narrow transverse velocity distribution, probed by a perpendicular laser beam exhibit significantly reduced Doppler broadening [7].

After aligning the laser beam perpendicular to the atom beam, the laser is scanned around the sodium D2 line. The atoms absorb when the laser is resonant with a transition, and the fluorescent decay is collected by a photomultiplier tube (PMT) mounted above crossing region. To reduce noise in the fluorescence signal, an optical chopper modulates the laser beam and the signal from the PMT is fed into a lock-in amplifier to extract the modulated signal, which in turn is logged into a laboratory computer (PC). The spectra of allowed transitions in the D2 manifold are shown in Fig. 3.5.

3.3.2 Saturated Absorption Spectroscopy

To set the frequency of the laser with high resolution, a high precision frequency standard must be used. During an experiment, the sodium beam is unavailable so

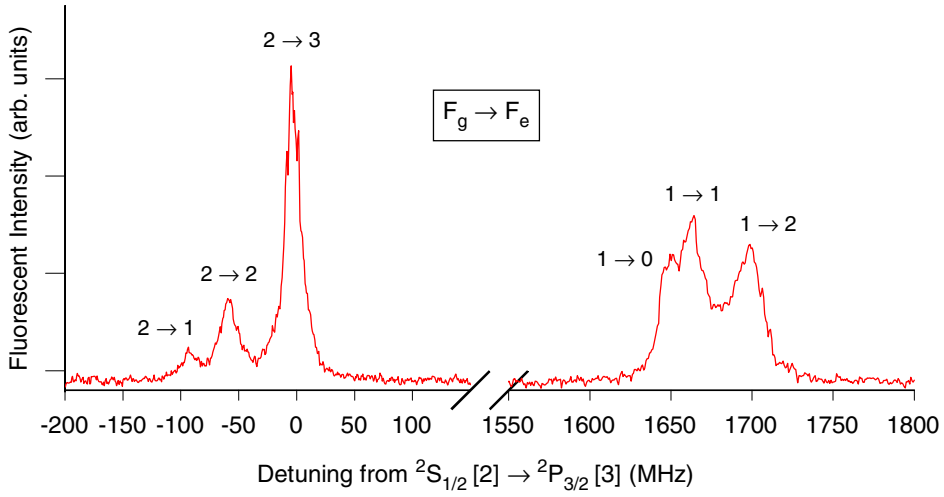

Figure 3.5: Fluorescence from cross beam spectrum. The allowed transitions in the D2 manifold are all visible.

a secondary is used; the signal from a saturated absorption cell containing sodium metal vapor is the obvious choice. A Pyrex cell, with background pressure $\sim 10^{-6}$ torr, contains sodium metal that is heated to $\sim 80°$C, increasing the sodium vapor pressure to $\sim 10^{-3}$ torr. At this pressure, the absorption lineshape is significantly Doppler broadened ($\delta\omega_D \sim 1.4$ GHz) and the center of the transition lineshape has an uncertainty greater than the precision to which the laser must typically be known (~ 1 MHz). However, by using the Doppler-free technique of saturated absorption spectroscopy [7], the transition linewidth can be reduced toward the natural linewidth ($\Gamma \approx 10$ MHz). A brief description of saturated absorption spectroscopy is presented here.

A high intensity laser beam ($S_0 > 1$) of frequency ω_L, nearly resonant with the transition frequency ω_0, drives atoms to the excited state when the detuning of the laser Δ is compensated by the Doppler shift $\Delta\omega_D$. The width of the

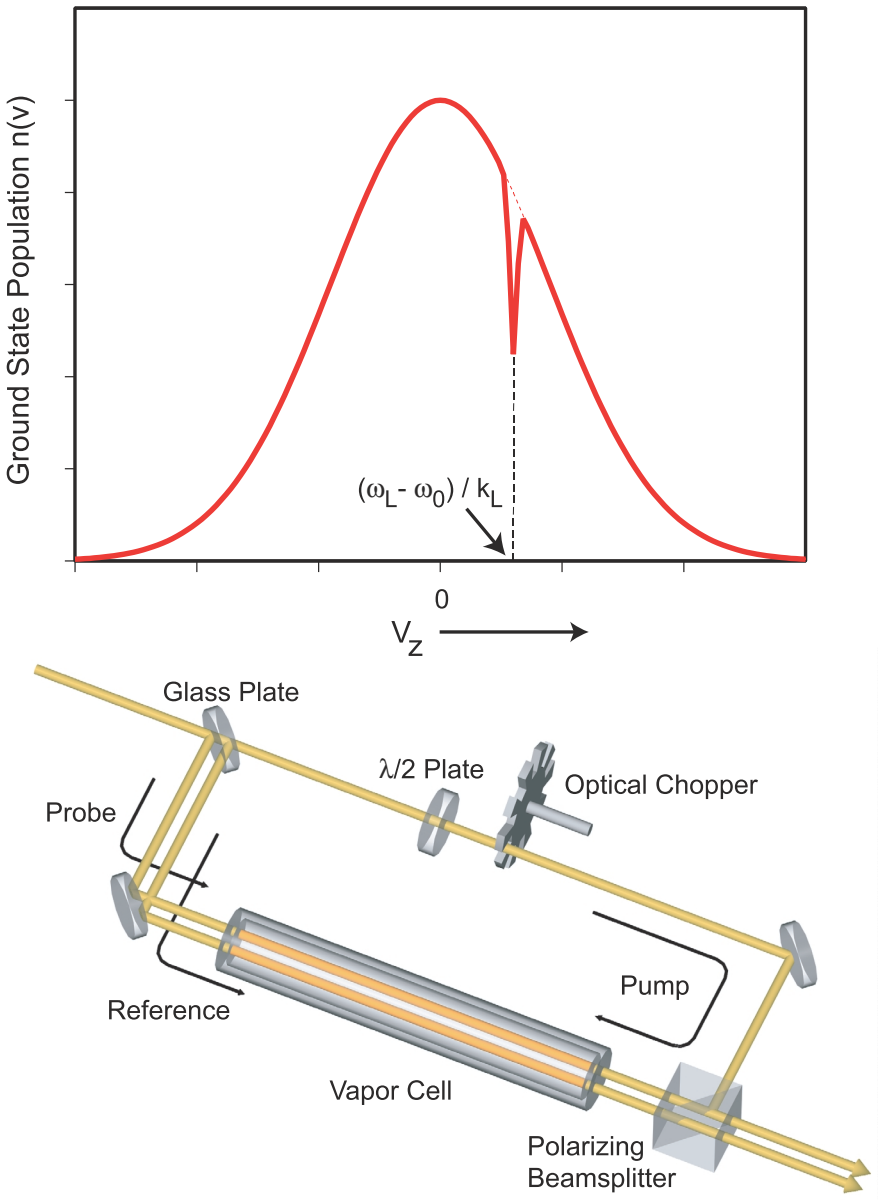

Figure 3.6: a) Perturbed ground state population caused by high intensity pump beam at $\Delta = v_z k_L$. b) Setup for saturated absorption spectroscopy used to lock laser frequency.

Doppler broadened lineshape $\delta\omega_D$ is very broad, compared to the power broadened natural width $\Gamma' = \Gamma(1 + S_0)$. Thus, only a portion of the ground-state velocity distribution $n(v)$, with velocity component v_z along the laser axis equal to Δ/k_L, is resonant with the laser. Because the beam has a high intensity, a significant fraction of the population with the resonant velocity class can be driven from the ground state distribution $n(v)$ as seen in Fig. 3.6a [7]. Atoms with velocity v_z such that the Doppler shift does not equal the detuning Δ, to within the power broadened linewidth are unaffected and remain in the ground state. In other words, the high intensity field saturates the transition for atoms within Doppler resonance with the frequency of the laser, henceforth to be called the pump laser.

A weak beam ($S_0 < 1$) is attenuated by resonant atoms according to Beer's law

$$I'(z) = I_0 e^{-n(v)\sigma_{12}(\omega)z} \tag{3.10}$$

where I_0 is the initial intensity, z is the propagation distance and $\sigma_{12}(\omega)$ is the absorption cross-section for the laser with frequency ω. If the weak probe beam passes through the cell, overlapping the pump beam, and scans over the entire Doppler lineshape, a near Gaussian absorption profile is obtained by measuring the intensity of the probe leaving the cell with a photodiode. The profile deviates from a Gaussian profile at the frequency where the high intensity laser has saturated the transition and the ground-state population is significantly reduced. The decrease in population causes an easily detectable decrease in absorption.

By producing the pump and probe beams from the same laser, the transition center ω_0 can be isolated. Introducing the pump and probe in a coaxial, but counter-propagating, arrangement causes the pump to saturate the transition

with atoms of velocity class v_z, but the probe is resonant with those with velocity $-v_z$. If the laser is tuned more than a power-broadened natural linewidth Γ' away from ω_0, the probe does not detect any population change caused by the pump. However, when the frequency is within Γ' of ω_0, the decrease in population results in a reduced attenuation of the probe laser intensity detected by the photodiode. If the laser scans across the entire Doppler profile, the measured lineshape is a Gaussian absorption profile with a sharp decrease in attenuation at the atomic resonance ω_0 [7]. To remove the Gaussian background, a second weak beam, passing through the cell, but not overlapping the saturating beam, is monitored with a photodiode to provide a reference lineshape. The optical layout for this system is shown in Fig. 3.6b. The reference signal is subtracted from the probe by connecting the photodiodes with opposite polarity so that the difference signal is collected directly, as shown in Fig. 3.7. The quality of the spectra depends on the overlap of the pump and probe beams. To ensure maximum overlap, the pump beam polarization is rotated 90° by a $\lambda/2$ plate and reflected into the vapor cell using a polarizing beamsplitter that passes the probe laser. Modulating the signal by placing an optical chopper in the pump beam path and feeding the amplified signal to a lock-in amplifier, the noise in the signal is reduced. The signal extracted by the lock-in amplifier is fed to an oscilloscope next to the laser controls so the frequency can be monitored as the laser scans. Similarly, the signal can be fed directly to a PC via a DAQ program to collect a spectra.

Figure 3.8a shows the saturated absorption spectrum and a crossed beam spectrum for sodium as a function of frequency, the crossed beam is the frequency reference used to calibrate the frequency scale. It is important to note the additional features that appear in the saturated absorption spectra that are not in

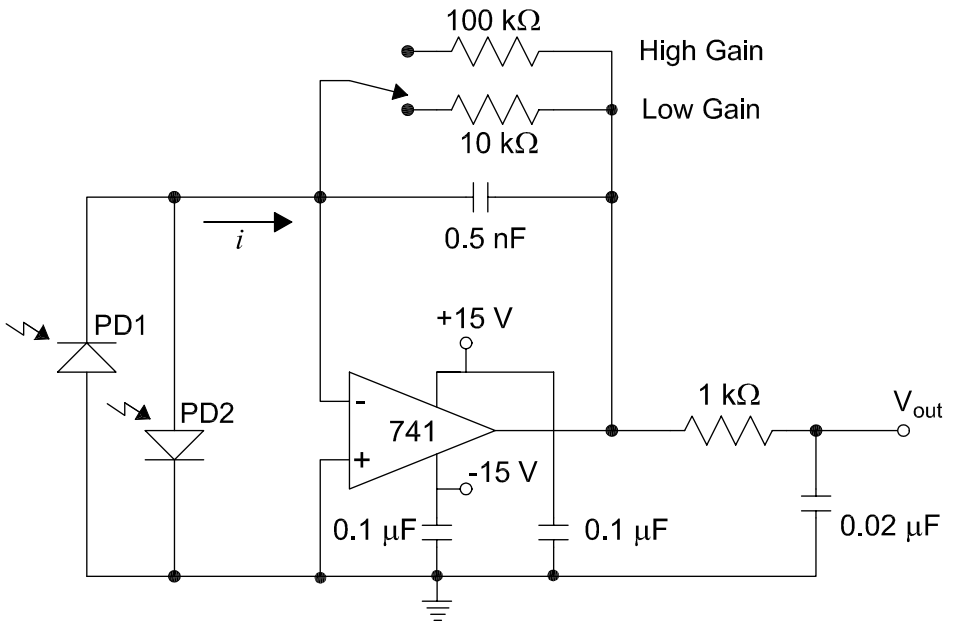

Figure 3.7: Circuit for amplifying saturated absorption spectroscopy signal.

the crossed beam spectra. These features, called cross-overs, occur at frequencies midway between transitions that have either a common upper or lower level [7]. Because of the broad velocity distribution of atoms, it is possible for the pump laser to depopulate a state via one transition and the probe laser to probe that same state with a different transition. Because there is a decreased population in the ground state, the absorption of the probe drops. Transitions with common upper levels also lead to cross-overs, but with enhanced absorption. Because the cross-over features are as reproducible as the transitions themselves, they can also be used as frequency markers. In some instances, the cross-overs are better frequency markers than the transitions because of a convenient frequency at which they occur. In the case of sodium, the cross-overs are typically stronger than the actual transitions. Figure 3.8b shows the saturated absorption spectrum

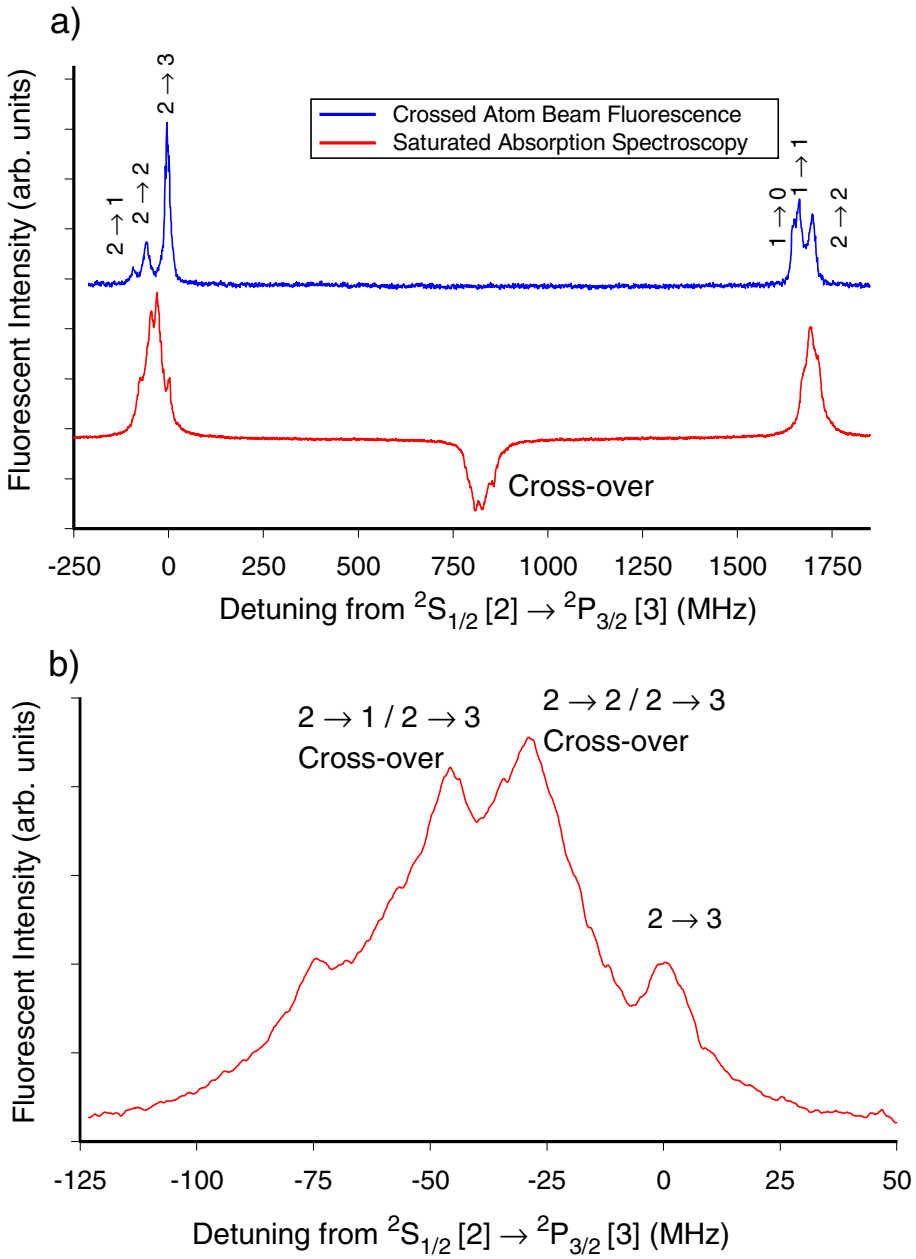

Figure 3.8: a) Sodium saturated absorption spectrum and crossed beam spectra for Na. The saturated absorption spectra shows the crossover halfway between the transitions from the two hyperfine ground state levels. b) The saturated absorption spectra near the cooling transition showing the dominance of the cross-over features.

with cross-overs near the cooling transition.

3.3.3 Molecular Iodine

The spectrum of molecular iodine is probably the best known of all spectra in the visible and near infrared [36]. By coincidence, there are four strong transitions of molecular iodine near the sodium D2 transition. These convenient transitions are used as frequency markers on broadly scanned spectra, such as those needed in calculating the velocity distribution of the atomic beam. A thin glass plate picks off a small fraction of the laser beam and directs the light through a sealed Pyrex cell containing iodine. At room temperature, sufficient partial pressure of iodine exists for laser induced fluorescence to occur if the laser is on resonance. A photodiode detects the fluorescence and drives a current proportional to the light power. An amplifier converts the signal to a voltage that is collected by a PC. The iodine signal is Doppler broadened at room temperature $\delta\omega_D \sim 0.4$ GHz, much narrower than in sodium because the mass is eleven times larger ($\delta\omega_D \propto m^{-\frac{1}{2}}$). While the Doppler width is still significant, it is still possible to use iodine in cases when small uncertainties in frequency are tolerable. Figure 3.9 shows a typical iodine signal.

3.4 Electro-optics

Due to the extreme cost of individual single frequency lasers, the ability to produce multiple frequencies out of a single laser head is desirable. In the work described in this thesis, acousto-optic modulators and electro-optic modulators shift lasers for frequency tuning purposes and to generate sideband frequencies

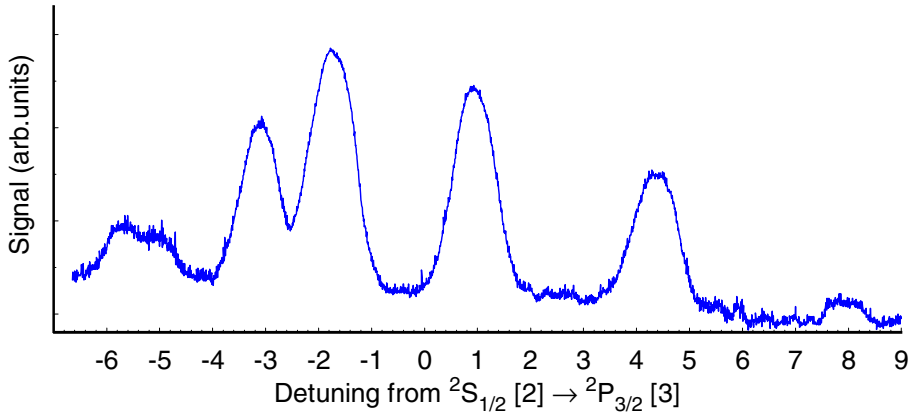

Figure 3.9: Iodine fluorescence spectrum near sodium D2 line.

for optical repumping.

3.4.1 Acousto-optic modulators

To set the dye lasers to their proper frequencies, different features within the saturated absorption spectrum are used. However, rarely is a feature exactly at the desired frequency. Shifting the frequency of the sampled portion of the laser beam passing through the saturated absorption cell by a known amount technique is used to shift the spectrum. We use acousto-optic modulators (AOMs) to shift, and simultaneously deflect, part of the laser beam [37]. A transducer applied to the crystal applies an rf acoustic standing wave with frequency ω_{AOM}. The laser photons and acoustic phonons mix and a produce spatially separated laser sidebands with integer multiples of the phonon frequency $\omega_d = \omega_L \pm m\omega_{AOM}$. The separation of the sidebands arises from the conservation of momentum, the matching conditions for the wavevectors are $\overrightarrow{k}_d = \overrightarrow{k}_L + \overrightarrow{k}_{AOM}$ [37]. The crystal

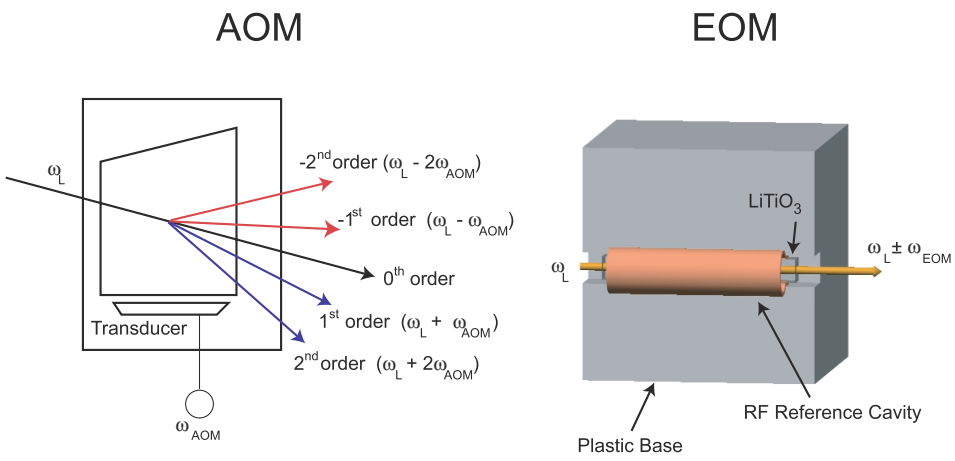

Figure 3.10: Diagrams of acousto-optic modulator (AOM) and electro-optic modulator (EOM). The AOM deflects the frequency shifted components out of the carrier, while the shifted frequencies remain within the beam after passing through the EOM.

is rotated with respect to the laser to optimize specific sidebands. The amplified output from a voltage controlled oscillator provides the rf frequency that drives the acoustic wave producing transducer mounted on the crystal. Attenuating the rf power applied to the crystal, typically less than 1 W, decreases the intensity of the diffracted beams. AOMs function at specific acoustic frequencies, as determined by the size of the crystal, and have a narrow bandwidth. Three different AOMs are used in this work, each with different acoustic centers: 260 MHz (Isomet, 1250C-829A), 80 MHz (Isomet, 1205C-1) and 40 MHz (Isomet, 1201E-1).

An AOM can also be "doubled passed" to double the frequency shift by reflecting the first order back through the AOM. The first order of the second pass

overlaps the initial beam, but by rotating the polarization of the beam prior to retroreflection (with a half wave plate), a polarizing beam splitter can separate the beams.

3.4.2 Electro-optic modulators

To prevent optical pumping to a dark state, it is necessary to include a repumping frequency to optical molasses or a MOT. Rather than using a second laser, we use an electro-optic modulator to add frequency sidebands to the carrier frequency. We apply a high power sinusoidal rf electric field with frequency ω_{EOM} across a crystal to vary its index of refraction. The varying index within the crystal mixes the laser frequency ω_L with the rf to produce evenly spaced sidebands shifted by the rf frequency ω_{EOM} around the incoming laser frequency $E \sim E_i \sin(\omega_L t) + E'_m \sin(\omega_L \pm m\omega_{EOM})t$ [37]. Unlike the AOM, where the phonons and photons travel in different directions, the rf electric field oscillates in the same plane as the laser beam and the sidebands are not deflected. We use a "homemade" EOM [38] made from a lithium tantalate ($LiTiO_3$) crystal. Mounted within a plastic base, the crystal is sandwiched within an rf resonance cavity formed from a piece of copper foil. The resonant frequency of the cavity depends critically on its shape; if the cavity is not resonant with the rf field, insufficient power is coupled into the crystal and modulation of the beam ceases. The rf signal, generated by amplifying the output from a rf synthesizer (Gigatronics, 6061A), is coupled into the cavity with an antenna formed with a loop of copper wire.

3.5 Vacuum System

Experiments with laser cooled and trapped species are performed in high, or ultrahigh, vacuum. The reduction of interactions between the species of interest, sodium in this case, and background atoms is critical. Interactions between sodium and background are either elastic, where the species bounce off of each other in a billiard ball fashion, or inelastic or reactive collisions. Beam experiments require special effort in design due to the continuous flux of atoms added to the chamber. Figure 3.11 shows the vacuum system for the experiments described in this thesis. There are four main regions in the chamber: the thermal beam source, optical collimation, longitudinal slowing, and interaction zone. A brief description of the system is provided here.

The thermal source developed for this thesis is described in detail in Chapter 4. A diffusion pump removes atoms exiting the oven but rejected by the beam skimmer. A water-cooled copper coil provides additional pumping speed by acting as a primitive cryopump upon which hot sodium atoms condense. Just downstream from the skimmer, an annular liquid nitrogen trap isolates the beam source from the rest of the chamber. The collimation region is formed by a stainless steel six-way cross with four viewports, through which optical collimation laser beams are passed. A 1.5 m stainless steel tube forms the longitudinal slowing stage which feeds the atoms to the interaction chamber. The interaction chamber is a homemade brass cross with multiple viewports for directing laser beams and detecting fluorescence with an externally mounted photomultiplier tube. A channel electron multiplier and charged particle optics are mounted inside. A diaphragm pump backed turbo pump (Pfeiffer, TSU065D) is connected to the top of the interaction chamber, as is a Bayard-Alpert ionization gauge for

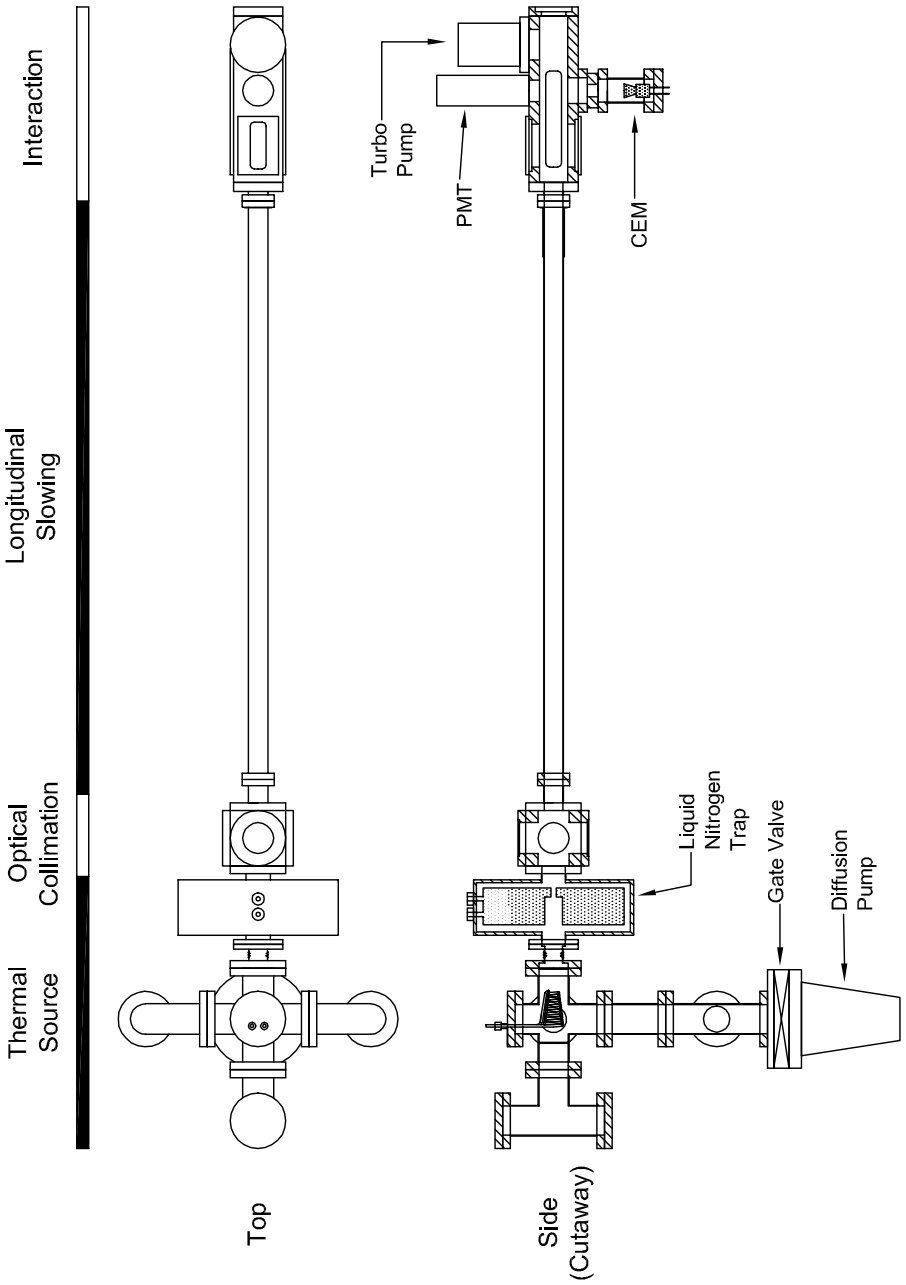

Figure 3.11: Sketch of vacuum system from above (left) and a cutaway view from the side (right).

measuring the chamber pressure.

Typical pressure for the vacuum chamber under experimental conditions is 1×10^{-6} torr. The pressure is limited by the common use of o-rings as well as the outgassing rate of the brass interaction chamber.

3.6 Signal Detection and Data Acquisition

3.6.1 Charged Coupled Device Cameras

Two different charge coupled device (CCD) cameras (Spectrasource, Teleris II and Pelco, MC5700-2) are used to monitor and measure the quality of the sodium beam. The cameras are oriented nearly parallel with the atomic beam and have lenses mounted on them to focus on a narrow field. Usually the cameras focus on a point in the interaction region, but in some situations, the beam is imaged at a position upstream. Orienting the cameras slightly off the beam axis not only allows a clear path for the longitudinal slowing laser beam, but also reduces the amount of background infrared radiation incident on the CCD from the hot oven at the upstream end of the vacuum system.

The Pelco camera output is directed to a close-circuit TV to monitor the beam profile when changes are made to the atom beam collimation. We monitor the atom beam in real-time using this technique. The Spectrasource camera is a complete video capture system, containing a framegrabber card connected to a PC where images are directly acquired. Images of the beam are taken by capturing the fluorescence from atoms induced by a resonant probe beam. Images are also taken with the probe laser beam tuned off the atomic resonance to capture the background light present from ambient sources and scattered laser

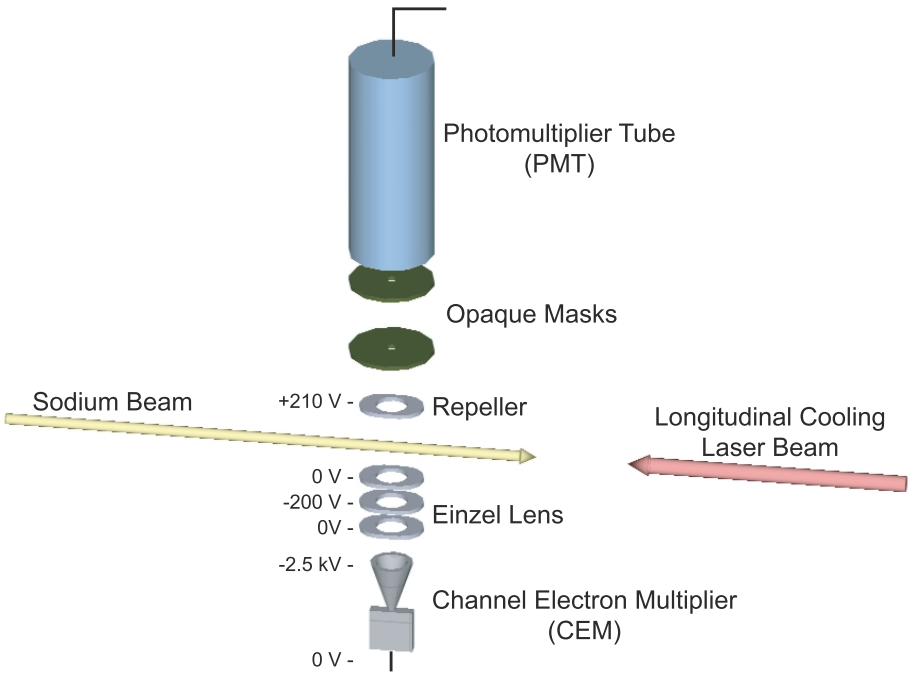

Figure 3.12: Schematic of detection devices around the interaction region, with the vacuum chamber removed for clarity. The PMT detects fluorescence and the CEM detects ions.

light. Scattered light is the reason why the probe is not simply blocked, this would eliminate scattered background. After subtracting the background image from the one with the beam plus background, the beam profile remains. Care must be taken to ensure that the camera is not saturated for either image and that the conditions for the images are exactly the same. Good practice is to take the images within a few seconds of each other to ensure that nothing changes. The image acquisition software performs averaging of multiple exposures as well as the image subtraction. The final figure can be exported into several file formats, including the graphical .tif and tab-delimited ascii .txt, useful for exporting to a graphics package for producing contour and surface plots.

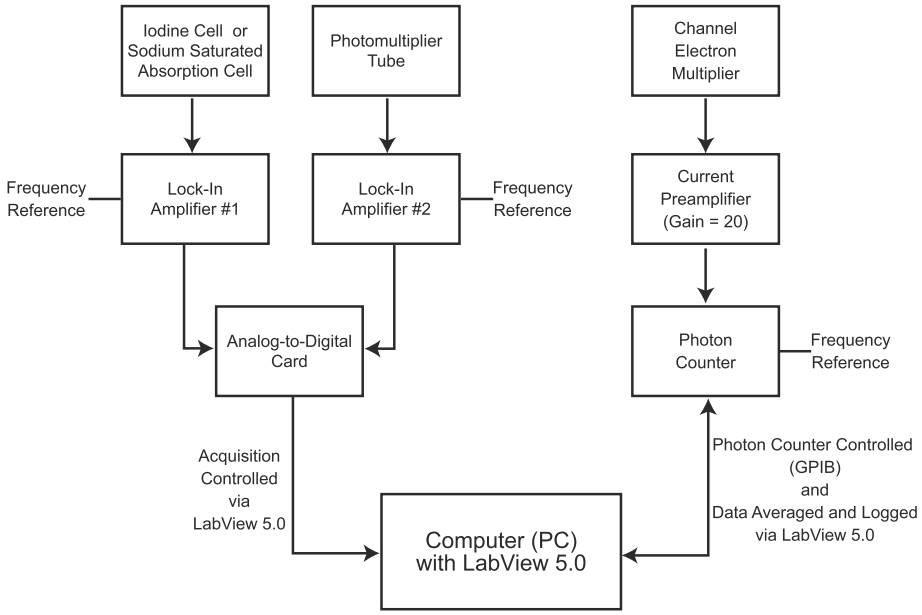

Figure 3.13: Block diagram of data acquisition. Fluorescence collected by the PMT is calibrated by a simultaneously scanning a known frequency reference. The data is read off the A-D card with a LabView 5.0 program. Ion signals from the CEM are preamplified and counted with a photon counter. The counter is controlled via GPIB by LabView which also averages and logs the ion production rate.

3.6.2 PMT

Fluorescence measurements in the beam are made with a Electron Tubes Inc. (Model 9658) photomultiplier tube (PMT). The PMT is biased with a voltage of -1.8 kV. Two opaque masks mounted in front of the PMT with 1 mm clear apertures that define a clear view directly to the fluorescence region reduce the background signal as seen in Fig. 3.12. Signal noise is eliminated using modulation techniques. The probe laser is chopped at 150 Hz with a homemade optical

chopper. The PMT signal and squarewave signal at the chopping frequency are then fed into a lock-in amplifier to extract the modulated signal and convert it to a DC voltage. The output from the lock-in amplifier is collected by an analog-to-digital data acquisition card in a PC. A program written in LabView reads inputs on several channels at a user controlled frequency. The multiple channel capability allows simultaneous collection of data from several sources, including the PMT and frequency reference signals. Figure 3.13 diagrams the acquisition process.

3.6.3 Ion Detection

A Dr. Sjuts channel electron multiplier (CEM) is the ion detector used in the suppression experiments. The detector has a gain of 10^7 with an operating voltage at -2.5 kV. A positively charged ion strikes the activated glass surface of the CEM and ejects a cloud of electrons. The electrons accelerate towards the back of the CEM, enlarging the cloud each time it strikes the surface as secondary electrons are generated. A collector plate at the end of the CEM collects the current from the electron cloud which is amplified by a non-inverting current preamplifier with a gain of 20 (EG&G, VT120C). The signal from the preamplifier feeds into a photon counter (Stanford, SR400) controlled with a remote PC via a program in LabView. The LabView program controls the counting period, frequency, and discrimination level on the SR400 in addition to logging the data as seen in Fig. 3.13.

To improve the detection efficiency, a combination of a ion repeller and an Einzel lens are used. The repeller is biased with a voltage of $+210$ V while the center plate of the Einzel lens is biased -200 V and is surrounded by two grounded

plates 0.8 cm on either side of the center plate. The Repeller is mounted 2 cm above the interaction region of the chamber, and the center of the Einzel lens is 5 cm below the interaction region. Figure 3.12 shows the layout of the CEM and ion optics with respect to the atom beam. The ion detection elements are mounted coaxial with the fluorescence detection elements.

Chapter 4

A Bright, Cold Sodium Beam

4.1 Introduction

In recent years much effort has been devoted to high performance atom beam sources. Bright beams, characterized by high density and narrow divergence, are useful in improving the efficiency of the loading of atom traps [2–4], for nanolithography [8, 12], atom interferometry [5], and cold collision studies [39–41]. Liouville's theorem [42] states that under the influence of conservative forces, the phase-space density of particles in a beam remains constant. Thus, spatially compressing a beam increases the momentum spread. The focusing of a collimated laser beam provides an excellent example. A convex lens "bends" the light toward the center axis, *decreasing* the beam diameter, however the transverse component of the photon momentum distribution *increases* as the photons pick up a transverse momentum component. But, the scattering force described in Chapter 2, Section 2.3 is frictional rather than conservative. Because of the dissipative nature of the radiation pressure, using optical cooling to collimate and compress a beam increases the phase-space density of neutral atom beams.

A variety of schemes have been developed over the last decade that use optical

forces to generate bright beams. Some of these techniques start with a cold or ultracold ensemble of atoms previously collected and generate a beam by breaking the symmetry of the confinement [2, 43–45]. Other schemes start with a hot thermal beam and use optical forces to increase the brightness [8, 10, 30, 46–49]. After introducing a several definitions used to quantify the performance of atom beams, a review of several sources is presented for comparison. Following the review is a detailed description of the multistage system developed as part of the original work presented in this thesis. The system renders a continuous thermal source into a continuous cold beam suitable for atomic collision studies. The diagnostic techniques used to characterize the beam follows the system description.

While the rate constants of cold and ultracold collisions can be measured in the "reaction bulb" environment of a magneto-optic trap (MOT) [39], the isotropic distribution of collision axes limits these studies to spatially averaged quantities. However the cold collision regime, where only a few partial waves participate, is just where alignment and orientation effects can be especially marked. A highly collimated atom beam therefore provides an ideal environment for studying favorable classes of collision kinematics. In particular inelastic or reactive processes proceeding through a two-step interaction sequence, the first occurring at long range and the second at short range, results in a very narrow acceptance angle along the molecular collision axis of the approaching atoms. Examples of these kinds of collisions are photoassociative ionization [39] and harpooning collisions [50]. If the divergence angle of the atom beam is also highly restricted, the molecular collision axis nearly superposes on the laboratory axis, providing a collision reference axis accessible to laboratory manipulation.

In this work, the combination of a simple effusive source, optical collimation of transverse velocity component $v_\perp$, Zeeman cooling of longitudinal velocity component $v_\parallel$, and a simple technique for sharply decoupling the atoms from the cooling cycle generates a bright beam. Under typical conditions, a sodium beam with 7×10^8 atoms cm^{-3} in a solid angle Ω of 2×10^{-6} sr with a longitudinal velocity of $\sim$ 350 m/s and longitudinal velocity spread of 5 m/s is obtained. This beam has been used to perform studies of the polarization dependence of the optical suppression of photoassociation ionization collisions in sodium [40] and of the polarization dependence of photoassociation [41].

4.1.1 Beam Performance Measures

The Liouville phase-space density is given by

$$\Lambda = \frac{N_A}{\tau} \tag{4.1}$$

where N_A is the number of atoms within the phase-space volume τ defined in Cartesian coordinates by

$$\tau = \Delta x \Delta y \Delta z \Delta p_x \Delta p_y \Delta p_z \tag{4.2}$$

where the Δ's are the distribution widths. For a system with cylindrical symmetry, such as a beam, the longitudinal $(\Delta x_\parallel, \Delta p_\parallel)$ and transverse components $(\Delta x_\perp, \Delta p_\perp)$ separate and the phase-space density is

$$\Lambda = \frac{N_A}{\pi(\Delta x_\perp \Delta p_\perp)^2 \Delta x_\parallel \Delta p_\parallel}. \tag{4.3}$$

After substituting the density $n = \frac{N_A}{\pi \Delta x_\perp^2 \Delta x_\parallel}$ and converting to the dimensionless definition $\widetilde{\Lambda} = \Lambda h^3$, the phase-space density for a beam is given by [49]

$$\widetilde{\Lambda} = \frac{n h^3}{m^3 \Delta v_\perp^2 \Delta v_\parallel} \tag{4.4}$$

where m is the atomic mass. The dimensionless definition of the phase-space density $\widetilde{\Lambda}$ is useful because when it approaches the order of unity, Bose-Einstein condensation occurs.

Optically brightened beams have been characterized in different ways, making the comparison of performance difficult. A recent work by Lison, *et al.* [49] addresses this issue and defines brightness

$$R = \frac{\Phi}{\Omega} \tag{4.5}$$

and brilliance

$$B = R\frac{v_{\|}}{\Delta v_{\|}} \tag{4.6}$$

to characterize the performance of different beams where the solid angle Ω is $\pi\left(\Delta v_{\perp}/v_{\|}\right)^2$ and the average atom flux Φ (atoms $\mathrm{s}^{-1}\mathrm{m}^{-2}$) is the product of the density n and the longitudinal velocity $v_{\|}$. The average beam current J (atoms s^{-1}) equals the product of the flux Φ and the atom beam cross-section $\pi\Delta r^2$ and is a common measure of the number of atoms within a beam. The brilliance B measures the velocity dispersion within the beam as well as the divergence. Because cold collision studies require low longitudinal velocity dispersion, the brilliance is an important measure of the beam quality.

The brightness and brilliance of the cold, collimated atom beam used in this work are, respectively, 1.2×10^{23} $\mathrm{s}^{-1}\mathrm{m}^{-2}\mathrm{sr}^{-1}$ and 8.6×10^{24} $\mathrm{s}^{-1}\mathrm{m}^{-1}\mathrm{sr}^{-1}$ with a dimensionless phase-space density $\widetilde{\Lambda}$ of 1.2×10^{-8}.

4.2 Review of Beam Sources

Riis, et al. [43] developed an "atomic funnel" source, essentially an extended length 2D-MOT, with optical molasses along the third axis. The counter-

propagating pair optical molasses beams, coaxial to the field zero on the axis of the 2D-MOT, have slightly different detunings. Because the photon scattering rate along this axis is not equal for atoms moving with equal but opposite velocities, they preferentially absorb from one beam until they reach a velocity v_z such that the rate balances, all the while being compressed by the 2D MOT. A frequency chirp-cooled beam loads the funnel with a 10% loading efficiency. The funnel generates a beam with density n of 10^8 cm^{-3} at velocity $v_z = 2.7$ m/s. The authors report a longitudinal temperature T_{long} of 180 μK and a transverse temperature T_{trans} of 300 μK, from which the brightness R and brilliance B are calculated to be 3×10^{15} m^{-2}s^{-1}sr^{-1} and 2×10^{16} m^{-2}s^{-1}sr^{-1}, respectively. While the low temperature in the longitudinal direction indicates a low relative velocity along the beam axis, the T_{trans} exceeds T_{long}. Because the transverse velocity spread is larger than the longitudinal, the solid angle subtended by the beam is large ($\Omega \sim 5$ sr). To study collisional orientation and alignment effects a beam must have narrow laboratory divergence. The divergence of this beam does not provide an axis to which a collisional axis can be referenced.

Nellessen, et al. [46] developed a scheme to transversely compress a monoenergetic sodium beam. Atoms slowed from a thermal source via chirp-cooling are deflected from the hot background gas using the radiation pressure force from a near resonant laser beam. The length of the radiation pressure deflector limits the bending of the beam to only the slow atoms; the unslowed atoms are not affected in the short time they subject to the force. The slow, pulsed atom beam enters a region with a 2D-MOT, which transversely cools and compresses the flux, reducing the beam diameter from 3 mm to 43 μm. The density of the compressed beam is on the order of 10^9 cm^{-3}. The chirp-cooling method

limits the longitudinal velocity spread to the velocity capture range ($\sim$ 15 m/s for sodium), and they report a transverse velocity near the Doppler limit of 40 cm/s. The peak density of this beam slightly exceeds the work presented here, but is not continuous because of the chirp-cooling technique. The *peak* value of the brightness is 5×10^{21} $m^{-2}s^{-1}sr^{-1}$ and the brilliance is 1×10^{23} $m^{-2}s^{-1}sr^{-1}$, however the pulsed nature of the beam results in a 10% duty cycle, reducing linear signal rates proportionally. The short time duration of the bright beam "on" cycle reduces the average signal in experiments with low count rates, such as far-detuned ($\Delta > 500$ MHz) photoassociative ionization, but the removal of the cooled atoms from the hot atoms is advantageous because of the reduction in collisions between the cold atoms and hot background flux.

A multi-stage collimation and brightening technique developed by Hoogerland, et al. [47] increases the density of a metastable neon beam. The system consists of the optical collimation of a thermal beam, followed by optical compression and secondary optical collimation stages. Because metastable noble gas beam sources are not as efficient as thermal alkali sources, the authors sacrifice mechanical divergence of the thermal beam to obtain more atoms within the beam by enlarging the skimmer diameter. The larger skimmer diameter results in larger transverse velocities, the largest exceeding the Doppler capture range for a standing wave molasses. A curved wavefront technique [51] increases the transverse velocity capture range, thereby enhancing the number of atoms within the collimated beam. The collimated beam then passes through a 2D-MOT that focuses toward the center of the trap, transverse velocity gained in the compression stage is eliminated with a second collimation stage. Because the longitudinal velocity distribution of atoms is broad, chromatic aberration limits

the density as the atoms are focused to different points. The brightness and brilliance are 1×10^{21} $\mathrm{m^{-2}s^{-1}sr^{-1}}$ and 6×10^{21} $\mathrm{m^{-2}s^{-1}sr^{-1}}$. The large longitudinal velocity spread (100 m/s) of the beam makes it unsuitable for cold collision studies. However, recent proposals [48] add a longitudinal slowing stage between the initial collimation and the compression stage that improves the prospects for cold collision study in metastable beam, but has not yet been realized.

Lison *et al.* [49] recently demonstrated a very bright cesium beam. An effusive cesium beam is optically collimated and longitudinally cooled. A set of permanent magnets produce a large magnetic-field gradient that decouples the atoms from the cooling cycle (see Section 4.3.4), producing a narrow longitudinal velocity distribution. The atom beam then passes through a magnetic lens formed with a hexapole arrangement of permanent magnets. The lens focuses the atoms, via interaction with the atomic magnetic dipole, to a point further downstream, where a near resonant optical deflecting beam directs the atoms off axis and into a collimating optical molasses stage. The longitudinal velocity is $35-120$ m/s with a velocity spread of about 1 m/s. The brightness and brilliance are measured to be 7×10^{21} $\mathrm{m^{-2}s^{-1}sr^{-1}}$ and 7×10^{23} $\mathrm{m^{-2}s^{-1}sr^{-1}}$. Deflecting the cold beam off the original beam axis removes the atoms from the hot background flux and also from the influence of the longitudinal cooling laser.

The brightness and brilliance of the atom beams summarized in this section as well as the one described in the following section are plotted as a function of phase-space density in Fig. 4.1. The brightness and brilliance of a sodium beam exiting the thermal beam source is also shown for comparison.

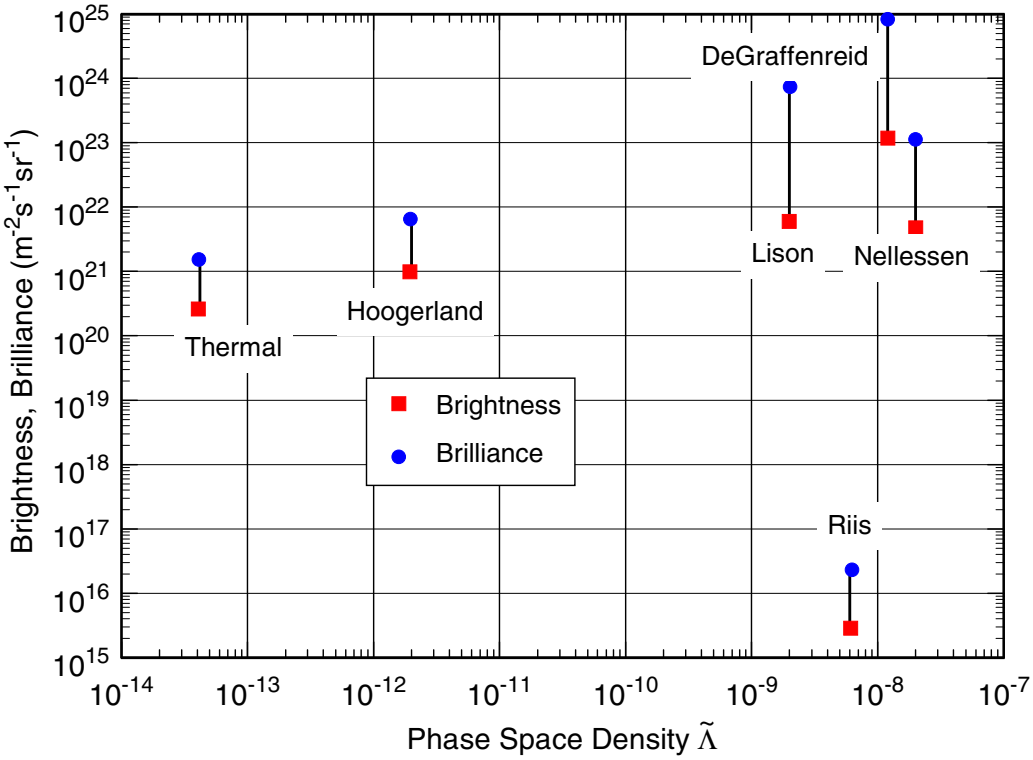

Figure 4.1: Comparison of the performance of several beam sources: Riis *et al.* [43], Nellessen, *et al.* [46] Hoogerland *et al.* [47], Lison *et al.* [49], and DeGraffenreid [this work]. Also shown is a thermal beam [this work] for comparative purposes. Adapted from [49].

4.3 Experiment

4.3.1 Résumé

We produce the brightened sodium beam using a multiple step process. Atomic flux emanating from a novel, externally heated beam source is collimated using transverse optical molasses. After collimation, a counter-propagating laser beam cools the atoms by slowing the longitudinal velocity; at a velocity near 350 m/s, an assembly of magnetic shielding rapidly terminates the slowing cycle, resulting

in a narrow longitudinal velocity distribution ($\sim$ 5 m/s). Figure 4.2a is a cartoon summary of the system and Fig. 4.2b shows the origin and distribution of the laser beams.

4.3.2 Thermal Beam Source

An externally heated oven assembled primarily from off-the-shelf UHV components generates the thermal beam as shown in Fig. 4.3. High-temperature custom fitted heating mantles [52] heat sodium metal inside a reservoir made from a standard CF tee to about 400°C, increasing the sodium vapor pressure to $\sim$ 0.5 torr. The reservoir connects to a standard six-way CF cross with a thin plate welded into the arm. A centered 1.25 mm diameter hole acts as a nozzle for the exiting flux. A 1.25 mm diameter skimmer, formed from a plate welded into the arm opposite the nozzle and positioned 16 cm downstream, mechanically defines and precollimates the flux. The mounting of the nozzle and skimmer within the same six-way CF cross ensures a stable and rigid atom beam axis. A separate heating mantle enveloping the cross heats the nozzle and skimmer to 400°C to prevent clogging. Type K thermocouples mounted between the chamber wall and the heating mantle measure the temperature of the oven and collimation region to monitor stable operating conditions.

The skimmer rejects the majority of atoms exiting the nozzle. To prevent pressure from building up in the region between the nozzle and skimmer, atoms must be pumped away. Failure to pump atoms out of region results in performance degrading effects. The free mean path between atoms within the mechanically defined beam and the background vapor decreases, resulting in increased collision rates that eject atoms from the beam path. As a consequence,

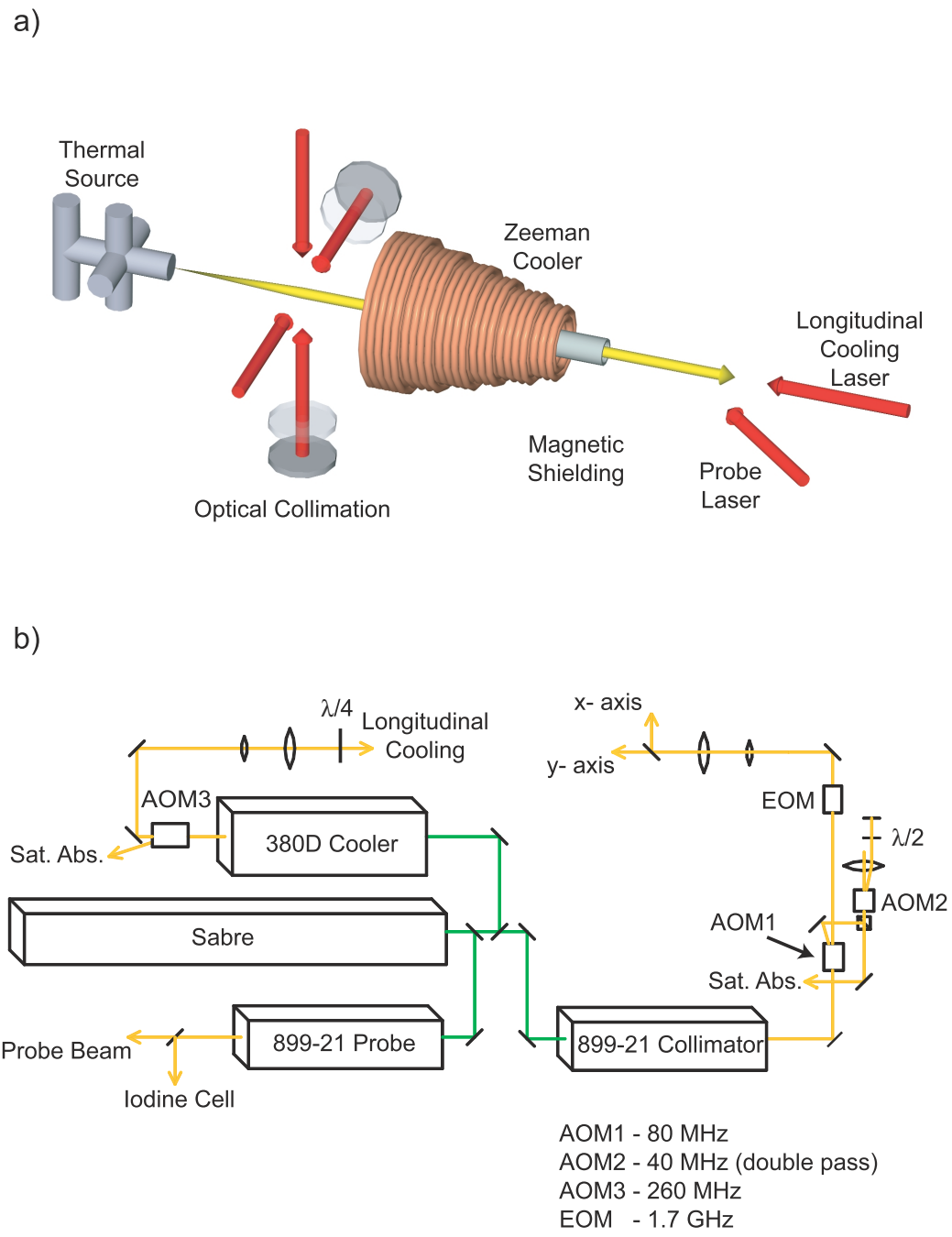

Figure 4.2: a) Schematic diagram of apparatus that produces a cold, bright sodium beam. b) Lasers used in experiment.

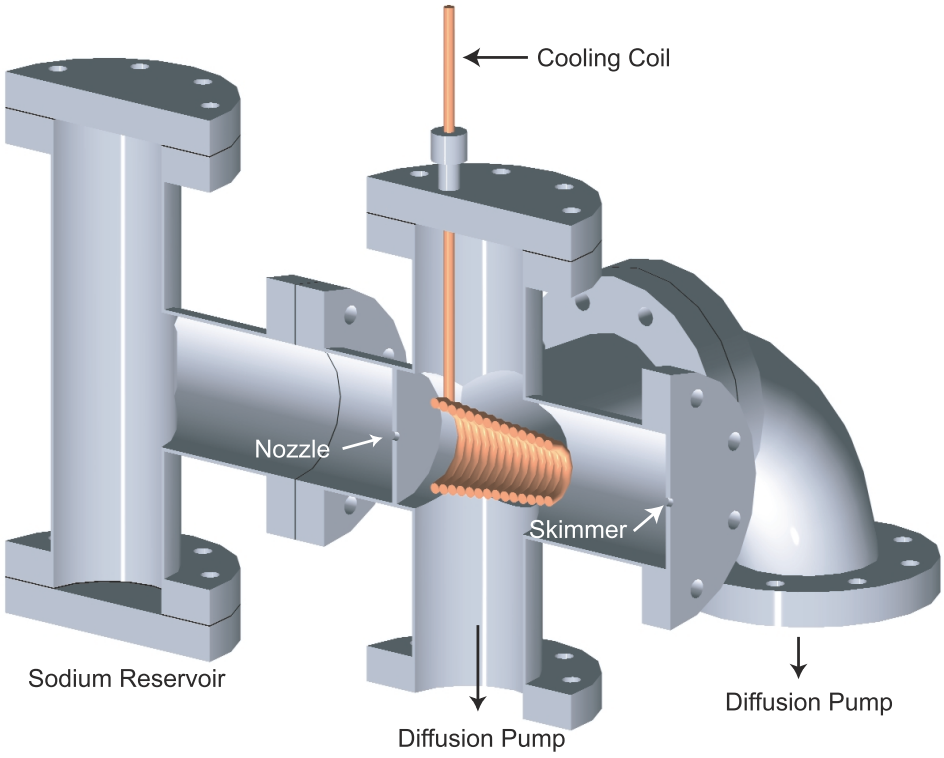

Figure 4.3: Cutaway diagram of thermal sodium beam source. Sodium metal stored in the reservoir is heated with custom shaped heating mantles (not shown) and effuses from the nozzle. The skimmer defines the beam and excess flux is removed by the diffusion pump and the coaxial cooling coil.

the region between the nozzle and skimmer begins to act as a second reservoir and poorly collimated atoms exit the skimmer and degrade the pressure downstream. A diffusion pump (nominal 4 inch diameter with pumping speed 800 L/s) removes the skimmed sodium vapor from the region between the nozzle and skimmer on three sides of the cross. A coiled solenoidal structure surrounding the atom beam axis and formed from 3/16 inch diameter commercial copper refrigeration tubing increases the pumping speed between nozzle and skimmer by acting as a primitive cryopump. It is introduced through the top arm of the cross. Simply running cold tap water in this cooling coil suffices to lower the vapor pressure of sodium to slightly below ambient temperature ($\sim 10^{-10}$ torr at 25°C). The cooling coil passes into the chamber via compression o-ring fittings. The o-rings require replacement each time the vacuum system is brought to atmospheric pressure because, despite the continuous flow of cooling water, the high temperature gradient across the o-rings causes the Viton to flow. The deformed o-rings seal the coil when the chamber is evacuated, but they shift and leak after breaking vacuum.

The skimmer-nozzle configuration mechanically restricts the atomic beam to a divergence of 8 mrad. The longitudinal velocity components (along the axis defined by the assembly) of the flux exiting the nozzle are below 1500 m/s. Therefore, the 16 cm distance from the nozzle to skimmer, together with the diameter of the holes, limits the transverse component which clears the skimmer to less than 10 m/s.

Mounting the sodium source external to the main vacuum chamber and surrounding it with the custom-fitted heating mantles provides a major benefit of uniform source temperature. Wrapping the heating mantles with aluminum foil

and several layers of fiberglass tape distributes the heat evenly around the oven and prevents turbulent instabilities in the beam flux. Another benefit of the external source is the ease with which the reservoir is recharged. The top flange on the tee is removed and small lumps of sodium metal are dropped in.

A welded aluminum frame supports the beam source and diffusion pump assembly and connects to the downstream portion of the chamber with a flexible UHV bellows. The frame has independent horizontal and vertical adjustments to control the beam orientation with respect to the rest of the vacuum chamber. Adjacent to the bellows, an annular-shaped liquid nitrogen trap with a hole diameter of 7.5 mm separates the collimation region from the longitudinal Zeeman cooling tube, providing further isolation of the down-stream stages from background sodium vapor.

4.3.3 Optical Collimation

The laser beams used for the transverse cooling (Section 2.2.3) are produced with a single frequency ring dye laser (Coherent, 899-21) with Rhodamine 6G dye solution pumped by an argon ion laser (Coherent, Sabre). The laser is tuned about 15 MHz below the $3\ ^2S_{1/2}$ [2] $\longrightarrow$ $3\ ^2P_{3/2}$ [3] atomic transition by referencing the laser to a feature in the sodium saturated absorption signal. A pair AOMs shift the frequency of the light passing through the saturated absorption cell such that when the saturated absorption signal is peaked on the cross-over at -29 MHz, the laser is operating at the desired -15 MHz as shown in Fig. 4.2b. To prevent populating the dark $3\ ^2S_{1/2}$ [1] state, the laser beam passes though an electro-optic modulator (EOM) to gain 1.7 GHz sidebands (approximately 15% in each first order sideband). A telescope assembly expands the beam diameter

to 2.5 cm which is divided into two beams of equal intensity (~ 75 mW/cm^2).

The beams enter the vacuum chamber, with the electric field polarized vertically in the laboratory frame, through antireflection coated viewports on orthogonal faces of a six-way cross located 10 cm downstream from the skimmer. After passing through the sodium beam, each laser exits the chamber, passing through a quarterwave plate before retroreflection back through the atom beam as seen in Fig. 4.2a. The double pass through the waveplate rotates the polarization of the laser beam 90° to horizontal polarization, setting up the optical molasses in a $lin \perp lin$ configuration [27].

In practice, we find that if the two pairs of molasses beams are overlapped, a significant number of atoms become trapped in a pattern of small light field potentials in the plane of the molasses beams, symmetrically displaced about the atom beam axis. We presume that these potentials are due to some laser beam interference pattern, but we did not attempt to analyze the phenomena in detail. Spatially offsetting the pair of molasses laser beams, creating *two* 1D molasses rather than *one* 2D molasses, as seen in Fig. 4.4, prevents these interference patterns. Figure 4.5 shows the atom beam profiles for the two possible molasses configurations. The "star-like" beam profile disappears and the average density increases by nearly a factor of two when the molasses beams are offset.

To prevent Zeeman effects from interfering with the sub-Doppler cooling mechanisms, stray magnetic fields in the optical collimation region must be less than 1 G. The tapered solenoid (used to longitudinally cool the flux), located downstream of the optical collimation region, produces the most significant source of stray magnetic flux. The fringe field is approximately 30 G at the center of the collimation region. Several sheets of high permeability magnetic shielding

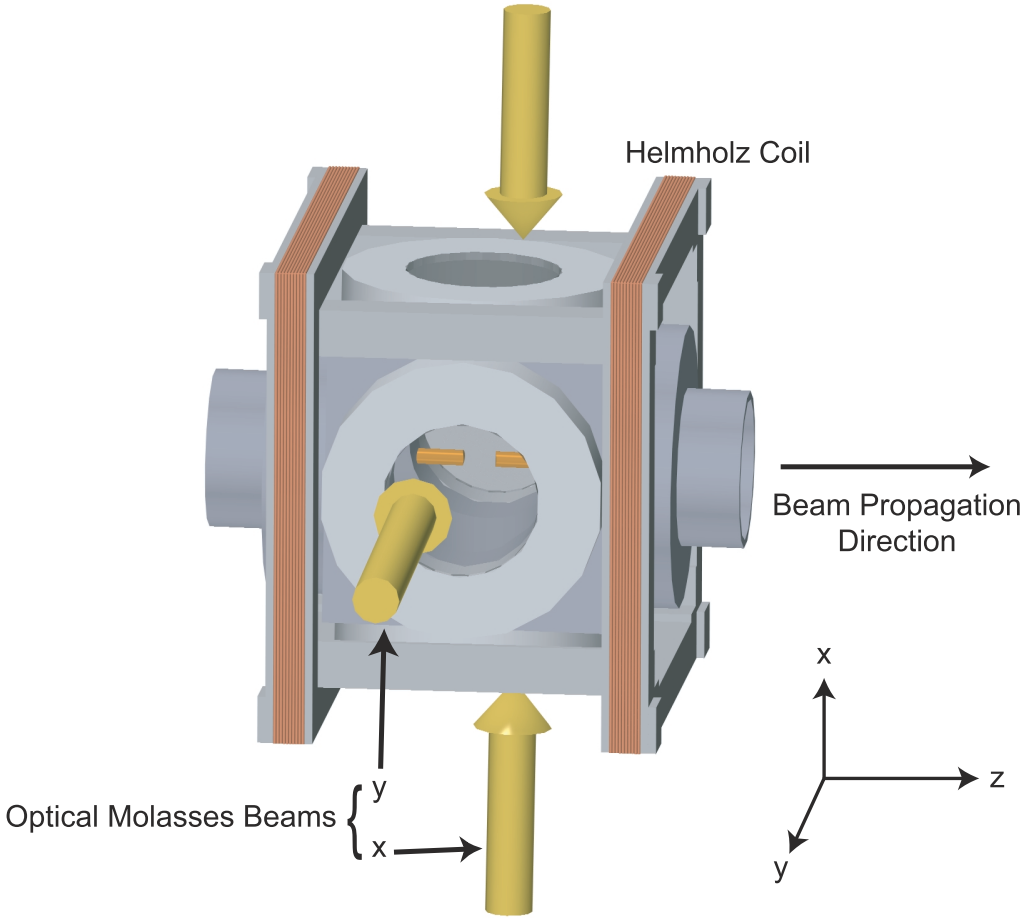

Figure 4.4: The collimation portion of the vacuum chamber with x- and y-axis collimation beams offset. The Helmholz coils cancel stray magnetic field from the upstream end of the Zeeman cooler.

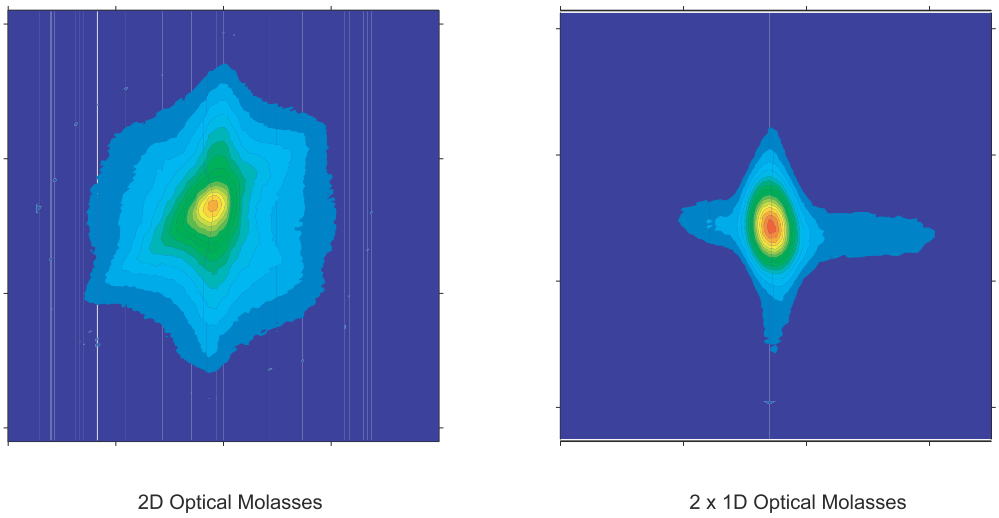

Figure 4.5: The collimation improves when the optical collimation beams are offset rather than overlapped. This forms two 1D optical molasses, rather than one 2D molasses.

(Magnetic Shield Corp., Co-Netic AA Alloy) placed perpendicular to the atom beam axis, between the collimation and longitudinal slowing regions, attenuates the magnetic field to 5 G. A pair of Helmholtz coils coaxial to the atom beam provides the means of canceling out ($|B| < 0.1$ G) the remaining stray field from the solenoid. The Helmholz current required to cancel the residual fringe field is shown in Fig. 4.6.

The optical collimation laser beams are aligned by monitoring the beam profile at the interaction region, 1.5 m downstream. Fluorescence from an on-resonance laser beam aligned perpendicular to the atom beam axis is collected with a CCD camera (Pelco, MC5700-2) and projected onto a television monitor for viewing.

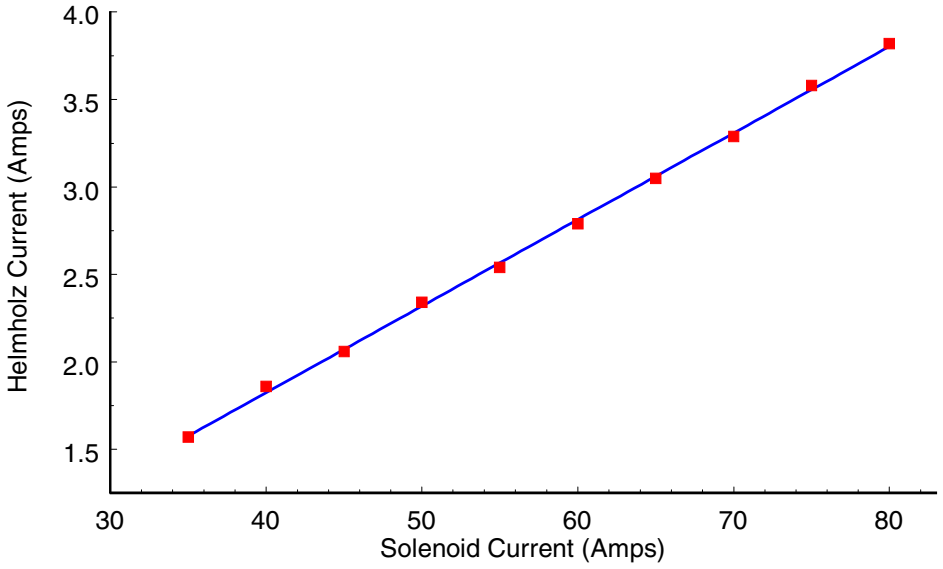

Figure 4.6: Helmholz current required to cancel the fringing magnetic field at the center of the collimation region as a function of the current in the tapered solenoid.

4.3.4 Longitudinal Cooling

The optically collimated sodium beam, with thermal longitudinal and sub-Doppler transverse velocity distributions, enters the region where cooling along the atom beam axis occurs. Atoms absorb photons from the counter-propagating laser beam and slow by momentum transfer. As the atoms slow, the absorption rate in the moving-atom-coordinate reference frame decreases as the Doppler shift of the photon frequency moves to the red, outside the range of the atomic absorption profile. The changing Doppler shift is compensated by a magnetic field that varies spatially such that magnetic sublevels stay in resonance with the optical field as the atoms slow [26]. To calculate the necessary field shape, we consider an atom moving with an initial velocity $\overrightarrow{v}_0$ subjected to a counter-propagating

laser beam with wavevector $\overrightarrow{k}$, detuned an amount Δ from the atomic transition, and saturation parameter $S_0 > 1$. We assume that as the atom moves down the beam axis z, it remains resonant with the field (i.e. Eqn. 2.29 hold), so the maximum acceleration can be calculated (see Eqn. 2.30):

$$\overrightarrow{a}_{\max} = \frac{\hbar\Gamma\,\overrightarrow{k}}{2}. \tag{4.7}$$

The atomic velocity v along z is therefore given by ($z = 0$ is arbitrary):

$$v(z) = \sqrt{v_0^2 - 2\,|a|\,z}. \tag{4.8}$$

Because the magnetic field is designed to keep the atom within resonance, we work backwards to calculate $B(z)$ by inserting Eqn. 4.8 into Eqn. 2.29:

$$\Delta + |k|\sqrt{v_0^2 - 2\,|a|\,z} + \frac{\mu_{12}B(z)}{\hbar} = 0 \tag{4.9}$$

where μ_{12} is the Bohr constant for the transition and equals $2\pi \times 1.4$ MHz/G. From Eqn. 4.9 $B(z)$ must have a shape given by $B(z) = B_0 + B_1(1 - z/z_\circ)^{1/2}$ for the atoms to remain resonant. A tapered solenoid with the high field at the upstream end satisfies this form, the measured field is shown in Fig. 4.7 Many turns of 1/4 inch diameter commercial refrigeration tubing form our solenoid. A high-current power supply (Sorenson, DCR 80-125T) provides the total DC current of 60 A required to generate the magnetic field on the field axis. Cooling water runs through the tubing to prevent overheating of the copper.

The maximum acceleration given by Eqn. 4.7 is the upper limit to the acceleration rate: $a_{\|} \leq a_{\max}$ where $a_{\|}$ is given by Eqn. 2.28. The condition where the atom remains perfectly resonant (Eqn. 2.29) with the Doppler-shifted light field as it slows is called "adiabatic following". Under the conditions of adiabatic

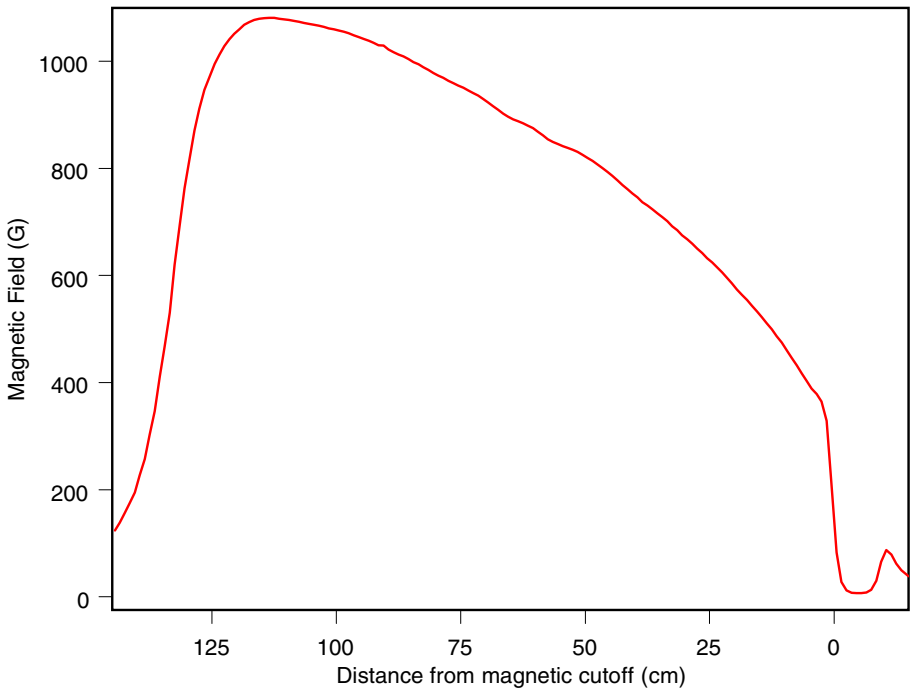

Figure 4.7: The magentic field inside the Zeeman cooler as a function of position. The origin is defined to be the edge of the magnetic shielding used to extract the atoms from the cooling cycle.

following, the rate of cooling is given by [53]:

$$\frac{v_{||}(z)}{k_L}\mu_{12}\frac{dB(z)}{dz} \leq a_{||} \tag{4.10}$$

and the field gradient required to maintain the condition is given by [53]:

$$\left.\frac{dB(z)}{dz}\right|_{crit} = \frac{1}{v_{||}(z)}\frac{\Gamma\hbar k^2}{2\mu_{12}m}\frac{S_0}{S_0+1}. \tag{4.11}$$

So long as the position dependent field is at the critical value, the atoms slow with maximum efficiency. A field gradient below the critical value will also cool the atoms, but will require a longer distance to do so because the cooling process is less efficient because the rate of absorption decreases. If the atoms reach

a position where field gradient exceeds the limit in Eqn. 4.11, the adiabatic condition fails and the atoms exit the cooling cycle because they are unable to absorb photons fast enough to remain resonant [53].

The Spectra-Physics 380D ring dye laser provides the light used for longitudinal cooling. The cooling laser is typically detuned 220 MHz below the atomic resonance; the frequency is set using the first order sideband from a 190 MHz AOM (Isomet, 1250C-829A) and tuned to the -29 MHz cross-over of the sodium saturated absorption spectrum. The intensity of the longitudinal cooling beam as it enters the vacuum chamber is 150 mW/cm^2. Just before entering the vacuum chamber, the laser beam passes through a quarter wave plate that produces the σ^+-polarization required for the stretched state cooling transition. Atoms move freely down the cooler until the Doppler-shifted frequency of the laser equals the Zeeman field-dependent $3\ ^2S_{1/2}\ [2, M_F = 2] \longrightarrow 3\ ^2P_{3/2}\ [3, M_F = 3]$ transition energy. Once in the cooling cycle, the atoms continue to decelerate and pick up slower atoms as they proceed down the cooler [26].

The increased density of the atom beam due to the collimation increases the optical thickness of the sodium beam. We developed a simple two-level model that calculates the intensity of the cooling laser as a function of position, taking into account the absorption of photons from the cooling laser by resonant atoms. We use a spatially dependent ground state distribution to model the resonant absorbing ground state population determined by the combination of the varying Doppler and Zeeman shifts. The model indicates that when the ground state density exceeds 2×10^8 atoms/cm^3, the intensity falls below the saturation intensity ($I_0 = 6$ mW/cm^2) for the cooling transition at the upstream end of the cooling region. Figure 4.8 shows the intensity of the cooling laser for

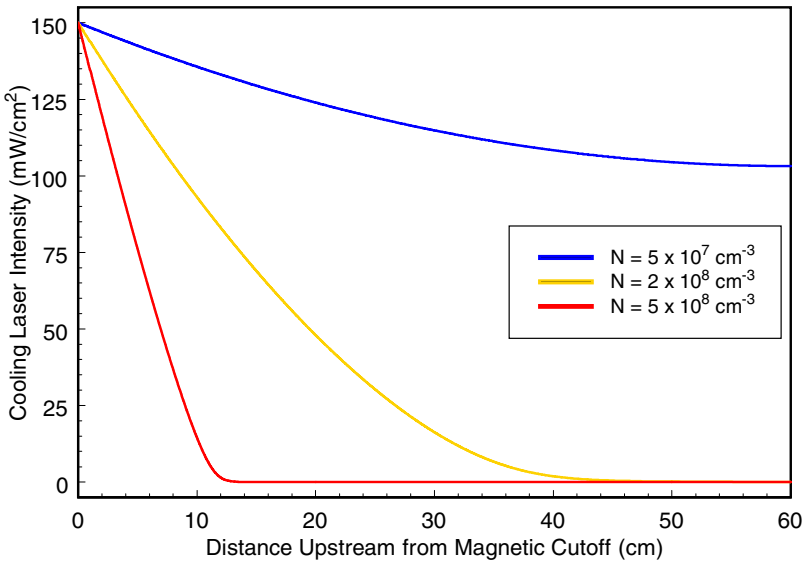

Figure 4.8: Model intensity for longitudinal slowing laser as a function of upstream distance. As the density of the beam increases, the intensity decreases by absorption, limiting the cooling efficiency of the fastest atoms.

several ground state densities as a function of distance upstream from the cooling cut-off. Cooling laser intensity below the saturation intensity at the upstream end of the chamber prevents the fastest atoms from being cooled, resulting in an increased percentage of hot atoms superimposed with a flux of coaxial fast atoms (there will always be a fraction of uncooled atoms that are not captured in the cooling cycle). To increase the intensity of the cooling laser at the upstream end, we focus the laser beam with a pair of lenses in a "near telescope" configuration that overcomes the loss in optical power by decreasing the laser beam cross-section. The focus of the cooling laser is adjusted with the lenses to get the

highest flux of cooled atoms at the exit of the solenoid.

Focusing the cooling laser also aids in preventing the beam from being optically pumped to the $3\ ^2S_{1/2}$ [1] state. The high laser intensity in the region between the optical collimation and the onset of the magnetic field power-broadens the cycling transitions between the ground-state and excited-state manifolds. Because the light is circularly polarized and subject to a weak magnetic field, the population cycles to the $3\ ^2S_{1/2}$ [2] ground-state.

4.3.5 Extraction

In order to study cold collisions, the relative velocity between pairs of atoms must be low ($v_r < 5$ m/s). To produce an ensemble of coaxially moving atoms with small relative speed, the laboratory distribution of longitudinal velocities must be narrow. Slowing the atoms to near zero velocity in the laboratory frame with the Zeeman slowing technique actually increases the distribution because of the field at the end of the tapered solenoid does not exactly match the field shape needed for cooling. Additionally, as the atoms are slowed to zero, the longitudinal and transverse velocity components become comparable in magnitude and the beam becomes unacceptably divergent. For these reasons, a beam with a narrow longitudinal velocity spread about a non-zero central velocity is desirable. Rapid removal of atoms from the Zeeman cooling cycle with velocity near 350 m/s produces an atom beam with these characteristics.

As discussed in Section 4.3.4, in order to maintain the condition of adiabatic following, the field gradient change must follow the atomic deceleration rate. By tailoring the magnetic field such that the gradient exceeds the critical value given by Eqn. 4.11, atoms are removed from the cooling cycle. By maximizing the

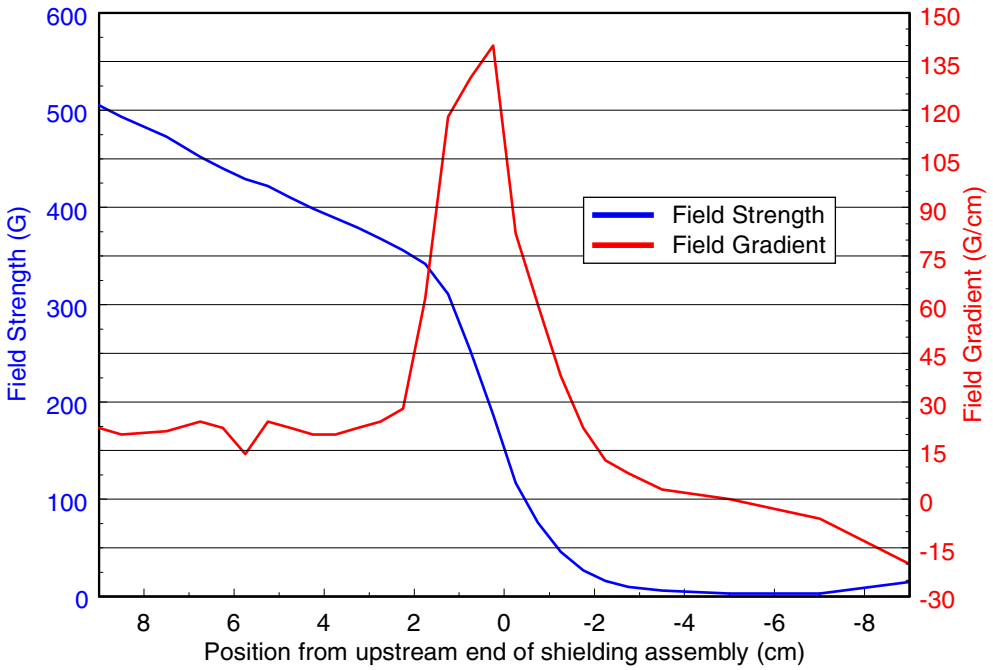

Figure 4.9: Magnetic field and field gradient at the end of the Zeeman slower. The field is attenuated to nearly 0 G within the shielding. The field gradient exceeds the critical field gradient for efficient longitudinal cooling.

curvature of the field at the point where the critical gradient is met enhances the rate at which the atoms decouple from the cooling cycle.

An assembly of magnetic shielding tailors the sharp magnetic gradient. Multiple layers of a high-permeability nickel alloy foil (McMaster-Carr), wrapped into a cylindrical tube 10 cm in length and wall thickness of 2 mm, form the assembly. The structure, mounted between the vacuum chamber tube and inner diameter of the tapered solenoid, shields the atoms from the Zeeman cooling magnetic field. By adjusting the position of the shielding, with respect to the end of the

solenoid, the position of the sharp cutoff can be changed, aiding in the ability to tune the central velocity of the atoms. Positioning the assembly further inside the solenoid will decouple the atoms at a higher magnetic field. If the detuning of the laser remains unchanged, a higher field at decoupling will result in a faster beam flux (recall that the resonant condition given by Eqn. 2.29). We position the shielding so that for a total solenoid current of 60 A, the longitudinal velocity at the cutoff location is 350 m/s. For $v_{\|} = 350$ m/s, the critical field gradient $\frac{dB}{dz}\big|_{crit}$ is calculated (Eqn. 4.11) to be ~ 32 G/cm. As seen in Fig. 4.9, the measured magnetic field drops to near 0 G while the gradient increases to a maximum value of 140 G/cm at the edge of the shielding, well above the critical value. Once decoupled from the cooling cycle, the slowed atoms continue moving downstream to the interaction portion of the vacuum chamber where it is characterized and used in cold collision experiments.

4.4 Beam Diagnostics

The atom beam density, velocities, and divergence must be characterized. The second Coherent 899-21 dye laser serves as the probe for all of the techniques described below. A molecular iodine cell is the frequency marker for this laser. The parameters described within this section were measured for a variety of operating conditions (laser frequency, intensity, solenoid current, polarization, oven temperature, etc.) but the results described here are for typical conditions for cold collision studies.

4.4.1 Atom Beam Size and Density

The diameter and density are critical to the characterization of the atom beam. We measure the spatial profile of the flux with a laser-induced fluorescence technique. Perpendicularly crossing the atom beam, a weak ($I \sim 1$ mW/cm^2), thin ribbon of light (~ 1 mm) excites atoms from the $3\ ^2S_{1/2}$ [2] to the $3\ ^2P_{3/2}$ [3] level by tuning the laser to the transition. We use a narrow ribbon to minimize the number of absorption cycles (~ 1175 photons) so minimize the influence of the laser on the beam shape. A CCD camera system (Spectrasource, Teleris II) captures the decaying fluorescence and background light. The background is subtracted as described in Section 3.6.1. Figure 4.10 show the fluorescence profiles for the uncollimated and collimated atom beams (the intensity of the uncollimated beam is scaled by a factor of 10 so it can be seen on the same scale as the collimated beam). By taking an image of a target grid at the same distance, the pixel size is calibrated so the beam diameter (FWHM) d can be extracted from the images. Analysis of the images in Fig. 4.10 reveals d equal to 2.5 ± 0.3 cm for the uncollimated beam and 0.2 ± 0.1 cm for the cold, collimated beam.

By measuring the absorption of a weak ($S_0 \ll 1$), resonant probe laser with circular polarization and diameter $d_{probe} \sim 1$ mm, we determine the ground state density n. As the probe laser with initial intensity I_0 passes through the atom beam with average density n and diameter d, the final intensity I' is

$$I' = I_0 \exp\left[-n\sigma_{12}d\right] \tag{4.12}$$

where the absorption cross-section σ_{12} is calculated by integrating over the spectral linewidth $\Delta\omega_L$ of the laser

$$\sigma_{12} = \frac{\gamma_e}{\gamma_g}\lambda^2\frac{\Gamma}{8\pi}\int_{\omega_0-\frac{\Delta\omega_L}{2}}^{\omega_0+\frac{\Delta\omega_L}{2}} \frac{d\omega}{\left(\omega-\omega_0\right)^2+\left(\frac{\Gamma}{2}\right)^2} \tag{4.13}$$

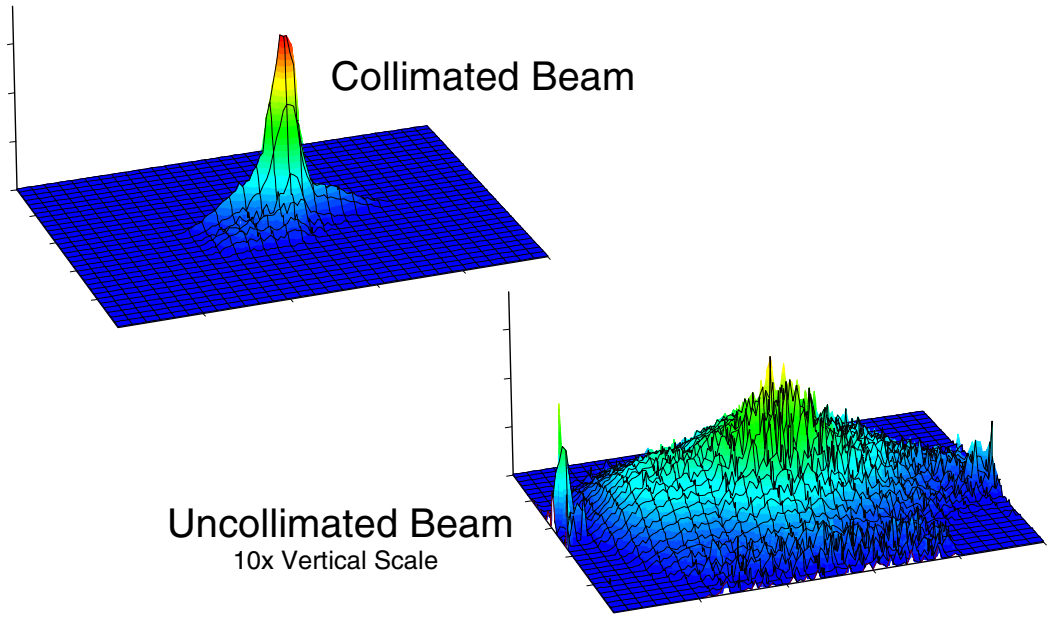

Figure 4.10: Fluorescence profiles of the collimated and uncollimated atom beams. The intensity of the uncollimated beam has been multiplied by a factor of 10 so the size of the beam is evident on the same scale.

because $\Delta\omega_L$ is less than the natural linewidth Γ. Because the Doppler broadening of the lineshape is insignificant due to the sub-Doppler transverse velocity, the ground-state velocity distribution $n(v)$ has been replaced by the density n in Eqn. 4.12. In Eqn. 4.13, γ_e and γ_g are the degeneracy factors for the excited and ground state and λ is the resonant wavelength. The circular polarization of the laser drives the stretched state transition so that γ_g and γ_e equal unity. Assuming a spectral linewidth of 1 MHz for the 899-21 laser that serves as the probe, the absorption cross-section is 8×10^{-11} cm^2. Using the cross-section, the measured intensities I_0 and I', and the beam diameter d calculated from the images described earlier, the density is determined. The density n at the interaction region increases from $(3 \pm 2) \times 10^7$ cm^{-3} for the thermal beam to $(7 \pm 3) \times 10^8$

cm^{-3} for the optically prepared beam, nearly a 25-fold density increase.

4.4.2 Longitudinal Velocity Distribution

To measure the longitudinal velocity of the atom beam, a weak probe beam ($I < I_{sat}$), introduced at an angle ϕ with respect to the atom beam (Fig. 4.11) and chopped at 150 Hz, scans near the rest frame atomic resonance. Because the atom flux is moving, there is a Doppler shift of the frequency of the light in the atomic frame of reference. Using Eqn. 2.22, we calculate the longitudinal and transverse contributions to the frequency shift:

$$\Delta\omega_D = v_{\parallel} |k_L| \cos\phi - v_{\perp} |k_L| \sin\phi \tag{4.14}$$

which reduces to

$$\Delta\omega_D = \frac{2\pi v_{\parallel}}{\lambda} \cos\phi \tag{4.15}$$

when $v_{\perp} \approx 0$ m/s. As the probe laser scans near the atomic resonance, when sum of the detuning Δ and the Doppler shift $\Delta\omega_D$ equals zero (Eqn. 4.15 for $B = 0$), the atoms will be resonant and will absorb photons from the laser. The photomultiplier tube (PMT) mounted on the interaction region collects the light emitted as the atoms decay from the excited state; the PMT signal is fed into a lock-in amplifier to extract the modulated signal from background light. The laser simultaneously scans across the molecular iodine cell to provide a reference for the frequency of the laser. Figure 4.11 shows the fluorescence signal collected as a function of detuning for both cooled and uncooled (no longitudinal slowing) atomic beams. The scale of the hot beam is magnified by a factor of 10 to show detail on the same scale. The second peak appearing at "blue" detunings arises

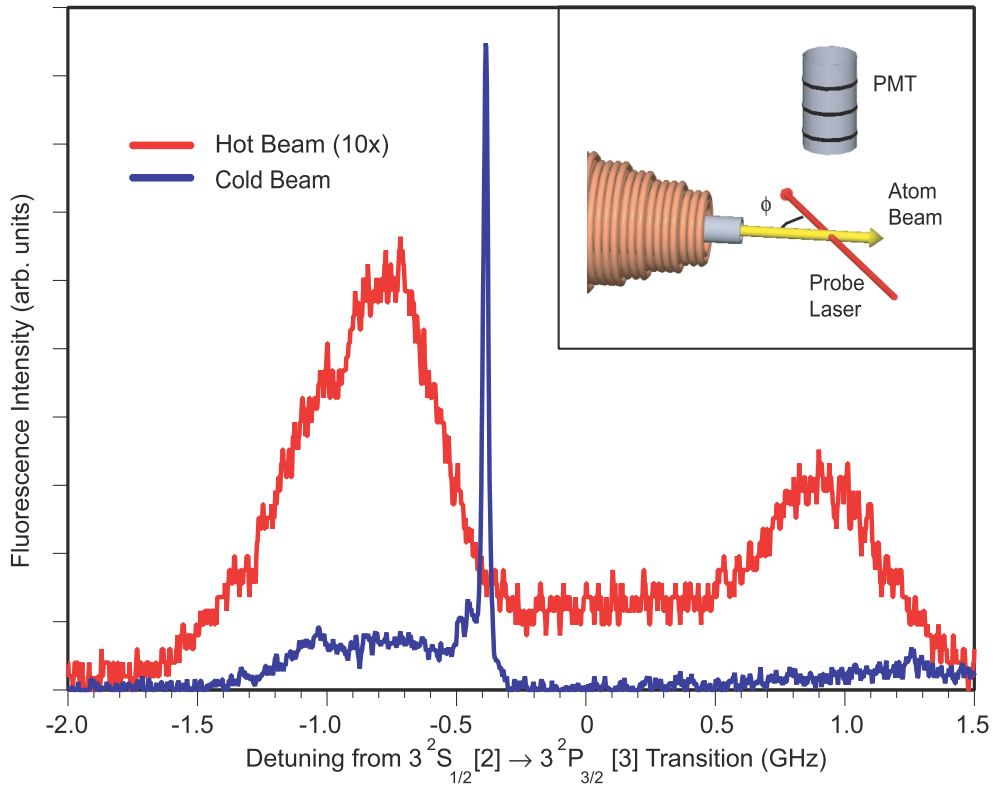

Figure 4.11: Fluorescence collected by PMT as laser crossing the atom beam with angle ϕ is scanned near the atomic resonance. The frequency scale is proportional to the velocity. The hot beam, scaled by a factor of 10, exhibits two fluorescence regions, due to population in both hyperfine ground states. The cooling process optically pumps all the atoms to the $F = 2$ ground state. The inset shows the setup.

from population in the $3\ ^2S_{1/2}$ [1] state that is optically pumped away during the Zeeman slowing.

We convert the frequency scale of the spectra to a velocity scale using

$$v_{\|} = -\frac{\Delta\lambda}{2\pi\cos\phi} \tag{4.16}$$

to determine the center velocity of the distribution as seen in Fig. 4.12. The spectral feature linewidth includes Doppler broadening arising from laboratory velocity distribution

$$f(v) = f_0 e^{-\left(2\sqrt{\ln 2}\frac{\left(v_{\|}-v\right)}{\Delta v_{\|}}\right)^2}, \tag{4.17}$$

centered about velocity $v_{\|}$ with a distribution $\Delta v_{\|}$, and the power-broadened natural linewidth projected into velocity space

$$g(v) = \frac{g_0\sqrt{1+S_0}}{v^2 + \left(\frac{\lambda\Gamma}{4\pi\cos\phi}\sqrt{1+S_0}\right)^2}. \tag{4.18}$$

The Doppler width and the power broadened natural linewidth are the same magnitude, so the observed width is a convolution of the two lineshapes, a Voigt profile $L(v)$. The Voigt profile sums up the natural linewidths of each possible Doppler shifted velocity center

$$L(v) = L_0 \int f(v')g(v-v')dv' \tag{4.19}$$

where the normalization constant L_0, the center velocity $v_{\|}$, and the velocity width $\Delta v_{\|}$ are variable parameters used to fit the experimental data. In this analysis we have treated the laser frequency distribution as a delta function. We can justify this simplification because the absorption linewidth for both the hot and cold beams are much wider than the laser linewidth ($\delta_l \sim 1$MHz) A typical

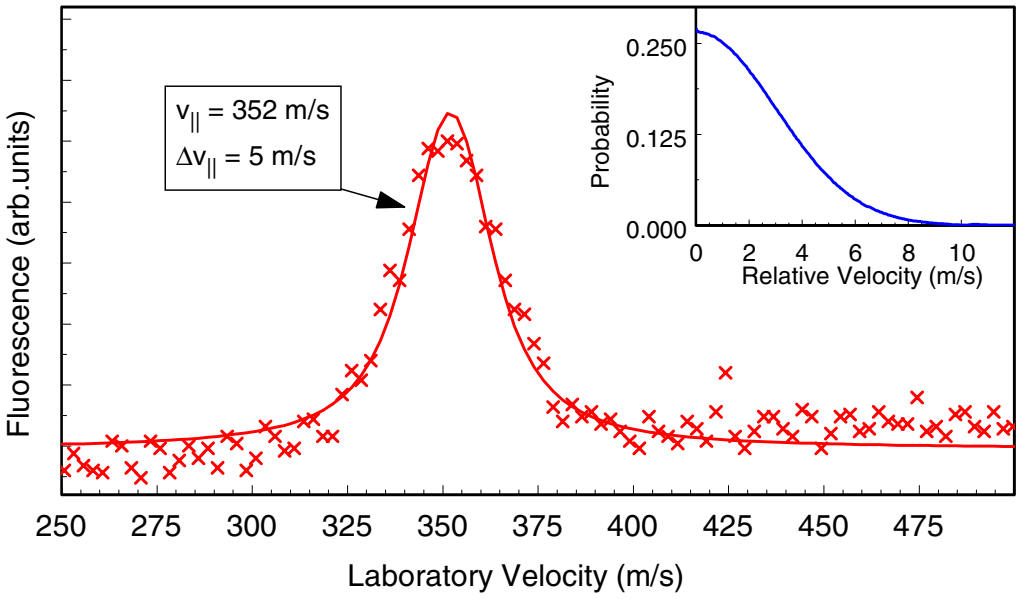

Figure 4.12: Fluorescence data converted to velocity scale and fit with a Voigt profile to extract the velocity width. Inset shows relative velocity distribution for atoms within the velocity group.

fit, with a laboratory velocity width $\Delta v_{||}$ equal to 5 m/s, is shown in Fig. 4.12. This corresponds to a longitudinal temperature $T_{long} \sim 17$ mK.

Recall that the collision temperature T_{coll} for a pair of atoms depends on the relative velocity v_r:

$$T_{coll} = \frac{1}{2k_B}\mu \langle v_r \rangle^2 . \tag{2.10}$$

An autocorrelation of the laboratory distributions, $f(v_1)$ and $f(v_2)$, for two atoms

$$\begin{aligned} P(v_r) &= \int_0^\infty \int_0^\infty f(v_1) f(v_2) \delta(v_r - |v_1 - v_2|) dv_1 v_2. \\ &= 2\int_0^\infty f(v_1) f(v_1 + v_r) dv_1 \end{aligned} \tag{4.20}$$

extracts the relative velocity distribution $P(v_r)$ of pairs of atoms in the beam. The inset of Fig. 4.12 shows $P(v_r)$ for two atoms in the atom beam. We calculate

the average relative velocity from the relative velocity distribution

$$\langle v_r \rangle = \int_0^\infty P_r(v_r) v_r dv_r. \tag{4.21}$$

For the data shown in Fig. 4.12, the mean relative velocity $\langle v_r \rangle$ is 2.4 m/s and the collision temperature T_{coll} is 4 mK.

4.4.3 Transverse Velocity Estimation

Measuring the transverse velocity distribution is not as exact as the longitudinal case. We estimate the residual transverse velocity of the sodium beam using a time-of-flight technique. The Spectrasource Teleris II CCD camera images the fluorescence from the atoms at the collimation chamber by focusing on the atoms from an on-axis angle looking directly up the vacuum chamber, in the absence of the longitudinal cooling laser. After subtracting off the background light, and comparing the image to that of a target grid taken at the same distance, the beam diameter is extracted. A second image of the beam, taken downstream at the interaction chamber (approximately 2.0 m downstream from the collimation region), allows us to calculate the increase in diameter. The difference in beam diameter Δd is measured to be approximately 0.08 cm and is due to the residual transverse velocity $v_\perp$. The average velocity $v_{\parallel,hot}$ of the atoms in the uncooled beam is 850 m/s and the separation between the two images z_{sep} is 2 m. We estimate the rms transverse velocity $v_\perp$

$$v_\perp \approx \frac{(\Delta d/2)}{\left(z_{sep}/v_{\parallel,hot}\right)} \tag{4.22}$$

to be 17 ± 5 cm/s. Using the definition from Chapter 2, this corresponds to a transverse temperature $T_\perp$ of 40 μK. If we assume a Boltzman-like velocity

Characteristic	Thermal Beam Source	Brightened Beam
$\Delta v_\perp$	5 ± 1 m/s	25 ± 5 cm/s
$v_\parallel$	850 m/s	350 m/s
$\Delta v_\parallel$	150 ± 50 m/s	5 ± 1 m/s
Ω	$(1 \pm 0.5) \times 10^{-4}$ sr	$(2 \pm 1) \times 10^{-6}$ sr
n	$(3 \pm 2) \times 10^{7}$ cm^{-3}	$(7 \pm 3) \times 10^{8}$ cm^{-3}
Φ	2.6×10^{16} m^{-2}s^{-1}	2.5×10^{17} m^{-2}s^{-1}
B	$(2.6 \pm 1) \times 10^{20}$ m^{-2}s^{-1}sr^{-1}	$(1.2 \pm 1) \times 10^{23}$ m^{-2}s^{-1}sr^{-1}
R	1.4×10^{21} m^{-2}s^{-1}sr^{-1}	9×10^{24} m^{-2}s^{-1}sr^{-1}
$\widetilde{\Lambda}$	$(4.2 \pm 2) \times 10^{-14}$	$(1.2 \pm 1) \times 10^{-8}$

Table 4.1: Beam performance.

distribution for this temperature, the transverse velocity spread $\Delta v_\perp$ can be shown to be 25 ± 5 cm/s.

4.5 Conclusions

By optically collimating, longitudinally slowing, and extracting the atoms in a narrow longitudinal velocity group, the flux exiting a novel thermal source is greatly brightened. Density at the interaction region increases from 3×10^7 cm^{-3} to 7×10^8cm^{-3}, while the solid angle Ω subtended decreases from 1×10^{-4} sr to 2×10^{-6} sr. Zeeman compensated cooling reduces the average longitudinal velocity from 850 ± 150 m/s to 350 ± 5 m/s. The brightness and brilliance of the final beam are $(1.2 \pm 1) \times 10^{22}$ s^{-1}m^{-2}sr^{-1} and $(8.6 \pm 4) \times 10^{24}$ s^{-1}m^{-2}sr^{-1},

respectively; factors of 460 and $6,000$ times larger than the thermal source. Table 4.1 summarizes the beam performance. The beam is suitable for nanolithography and orientational collision studies, but $v_\perp$ is too large for this beam source to be suitable for trap loading.

Chapter 5

Polarization Dependence of the Optical Suppression of Photoassociation

5.1 Introduction

Laser cooling techniques allow scientists to study a unique realm of atomic and molecular physics where wave mechanical behavior dominates. The study of collisions between slowly moving atoms, cold collisions, has become a broad and active area of research [39]. In this realm, the deBroglie wavelength of the atoms exceeds atomic sizes and becomes comparable to or greater than chemical bond lengths. Collision frequencies exceed excited state lifetimes (tens of nanoseconds). Because the centrifugal barriers of the partial waves in the collision become higher than the collisional energy, only the first few partial waves contribute to the dynamics of a collision. In this chapter, the polarization dependence of optical suppression of photoassociation is presented.

Most cold collision experiments use alkali metal or metastable noble gas atoms and are performed in a magneto-optic trap (MOT) or a slowed atomic beam. The choice of these species for study is the simplicity of their hydrogen-like structure,

closed electronic transition for laser cooling, and the availability of commercial lasers at the required wavelengths.

Because of the long interaction time and large deBroglie wavelength characteristic of cold atomic collisions, the scattering event is particularly sensitive to the details of the interaction potentials of the atom pair. The presence of near-resonant optical fields can influence the collision. Optical excitation to a different molecular potential will affect the dynamics of the collision due to changes in the forces exerted on the atomic pair. In fact, the presence of non-resonant optical fields may influence the collision, as we will see later in the case of high field optical suppression.

5.1.1 Long-range Internuclear Potentials

When properly tuned, a laser beam can stitch a pair of free atoms together to form an excited molecular state, a process called photoassociation. Because the atoms are initially greatly separated, the long-range nature of the molecular potentials is important. The long-range ground-state potential is always attractive at long range and arises from the instantaneous charge distributions in the atoms [54–56]. After expanding the charge distribution into a series of multipole moments, the long-range ground-state potential $V_{gr}(R)$ can be shown to be

$$V_{gr}(R)_{R\longrightarrow\infty} \simeq -\frac{C_6}{R^6} - \frac{C_8}{R^8} - \frac{C_{10}}{R^{10}} + \cdots , \tag{5.1}$$

where R is the internuclear separation and the series of coefficients C_i go as the square of the multipole polarizabilities for homonuclear collisions. The first coefficient C_6 is from the dipole-dipole interaction, C_8 is the dipole-quadrupole interaction, and C_{10} comes from both the dipole-octupole and quadrupole-quadupole interaction [54–56]. In this series, the largest term is the dipole-dipole and many

authors only mention this term. However, experiments can detect the higher order terms in the expansion, as well as the retardation effect [55] caused by the finite time it takes for information to transfer between the two atoms. In the limit as $R \longrightarrow \infty$, the potential correlates to a pair of ground-state $3\ ^2S_{1/2}$ atoms, the S + S asymptotic limit.

The excited-state molecular potential $V_{ex}(R)$ correlates to a ground state ($^2S_{1/2}$) atom and an excited ($^2P_{3/2}$) atom, the S + P limit, for large interatomic separation. For a homonuclear diatom, a resonant dipole interaction between the atoms produces the long-range potential [55, 57, 58]

$$V_{ex}(R)_{R\longrightarrow\infty} \simeq \hbar\omega_0 \pm \frac{C_3}{R^3} \pm \frac{C_5}{R^5} + \alpha_{FS}^2 \frac{W}{R^4} + \cdots \tag{5.2}$$

where $\hbar\omega_0$ is the asymptotic energy for the excited state molecule, C_3 arises from the resonant dipole interaction between the excited and ground state atom, C_5 is the resonant quadupole interaction, and the last term comes from retardation. Higher order terms included, but not shown, in Eqn. 5.2 include the electrostatic dispersion energies that arise from the charge distribution expansion, as in Eqn. 5.1. The retardation effect is scaled by the square of the fine structure coefficient α_{FS} ($\simeq \frac{1}{137}$) [55, 58] and cannot be ignored for accurate comparison between theory and experiment. As in the case of the ground state potential, usually only the dipole term is mentioned by authors because it is the dominant term. The force may be either attractive ($-C_3$) or repulsive ($+C_3$), depending on the whether the dipole exchange is in phase or out of phase.

Fine and hyperfine structure further complicates the system because of the many level crossing and interactions within the "spaghetti" of potentials. These effects, while important in quantitative models, are not necessary to qualitatively understand photoassociation.

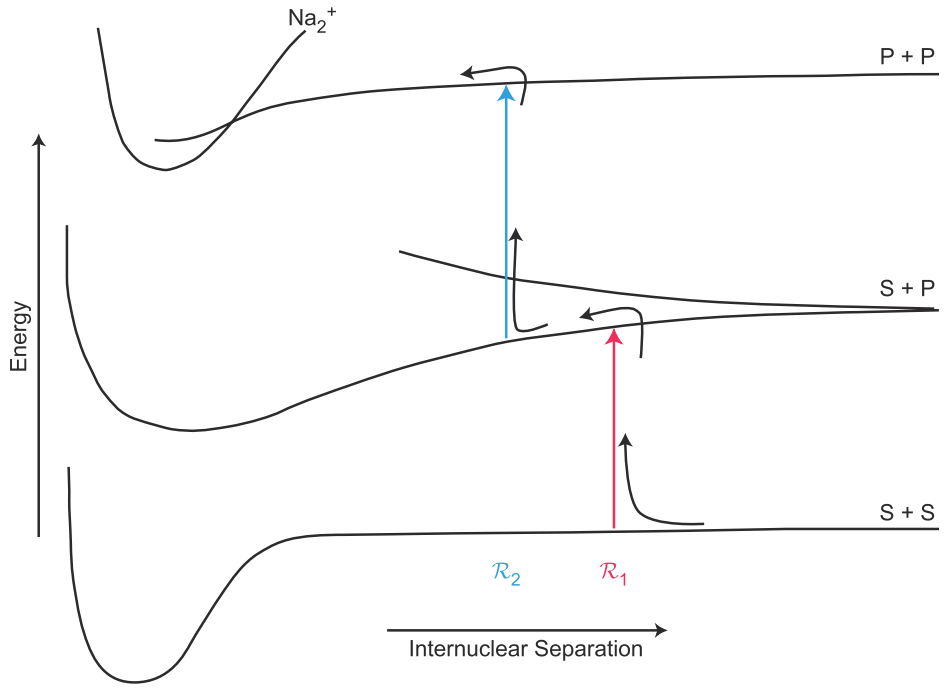

Figure 5.1: Photoassociative ionization in sodium. Absorption of a red detuned photon (ω_1) promotes a pair of atoms separated by $\mathcal{R}_1$ to an excited attractive level. After absorbing a second photon, as separation $\mathcal{R}_2$, the pair is promoted to the autoionizing, doubly excited level.

5.1.2 Photoassociative Ionization

A semi-classical model, seen in Fig. 5.1, presents the highlights of photoassociation, but must be followed with some comments about issues more founded in quantum mechanics that are ignored by the model. As a pair of cooled, ground state atoms approach each other under the influence of the attractive force arising from the potential from Eqn. 5.1. As a result of the optical cooling, the atoms have a kinetic energy distribution ($\sim k_B T_{rel}$) on the same order of magnitude of transition linewidths ($\hbar\Gamma$). As the atoms approach with relative velocity v_r in the

presence of an optical field tuned the red ($\Delta < 0$) of the atomic resonance, one of the atoms may absorb a photon from the field if the photon energy $\hbar\omega_L$ equals the difference between the ground- and excited-state potential energy. The radius of excitation, called the Condon point $\mathcal{R}_1$, depends on the laser detuning

$$\mathcal{R}_1 = \left[\frac{-C_3}{\hbar\Delta}\right]^{1/3} \tag{5.3}$$

where only positive and real values of $\mathcal{R}_1$ are physically realistic. Absorption of a photon promotes the pair to the excited attractive level via a free-to-bound transition:

$$\mathrm{Na} + \mathrm{Na} + \hbar\omega_L \longrightarrow \mathrm{Na}_2^* \tag{5.4}$$

this process is called photoassociation (PA). The atoms in the bound state accelerate towards each other because of the attractive force governed by the $-C_3$ coefficient. On average, the dimer remains in the excited state for a time on the order of the $3\ ^2P$ lifetime τ prior to spontaneous decay.

If the bound, excited molecule is subjected to additional optical fields prior to decay, other molecular states may be populated. In photoassociative ionization (PAI), a ground-state molecular ion is produced after the additional absorption of one or more photons. The ionization process occurs in sodium in a single step if a second photon excites the pair, at Condon point $\mathcal{R}_2$, to the doubly excited potential that correlates to two $3\ ^2P$ atoms in free atom limit; this level crosses the ground-state molecular ion potential and autoionizes to form the molecular ion:

$$\mathrm{Na}_2^* + \hbar\omega' \longrightarrow \mathrm{Na}_2^{**} \longrightarrow \mathrm{Na}_2^+ + e. \tag{5.5}$$

Other alkali metals do not have this autoionization channel and must be pho-

toionized via direct ionization (usually through an intermediate step):

$$\begin{aligned} \mathrm{Rb}_2^* + \hbar\omega' &\longrightarrow \mathrm{Rb}_2^{**} \\ \mathrm{Rb}_2^{**} + \hbar\omega'' &\longrightarrow \mathrm{Rb}^+ + \mathrm{Rb} + e. \end{aligned} \tag{5.6}$$

Detecting the ions poses no difficulty and therefore they are the usual signal detected to monitor the collision.

In reality, transitions only occur to the first excited state when there exists a vibrational state in the excited potential that has an energy $\hbar\omega_L$ above the ground-state atoms. Scanning the frequency of the photoassociation laser and monitoring the production of molecular ions shows ro-vibrational series in the first excited state. The intensity of the series depends on the intensity of the optical field, the density of ground-state atoms and the strength of the coupling between the levels. The coupling strength depends upon the overlap, or Franck-Condon, factor for the transitions. Because the position of the atoms does not change significantly during the transition (i.e. the transitions are "vertical"), there must be significant overlap between the ground- and excited-state wavefunctions. The Franck-Condon factor F_{ge} is given by [24]

$$F_{ge} \simeq D_{ge}^e \langle 1|2\rangle^2 \tag{5.7}$$

where D_{ge}^e is the electronic transition moment. When F_{ge} approaches zero, there is no overlap between the ground- $|1>$ and excited-state $|2>$ wavefunctions and a transition allowed by energy conservation does not appear in the spectra.

The semiclassical model also neglects hyperfine structure and angular momentum. The above mentioned spaghetti of potentials leads to long-range molecular potentials in the with Hund's case (c) angular momentum coupling [59]. The long-range, bound 0_g^- and 1_u potentials have *inner* turning points larger than the

ground state Na_2 molecule separation. To develop accurate models, these states can not be ignored.

High resolution PA measurements have been used to determine the atomic excited-state lifetime ($\tau \propto C_3^{-1}$) [60–62], s-wave scattering length (an important parameter for the formation of Bose-Einstein condensation in dilute atomic gases) [63–65], and molecular dissociation energies [66].

5.1.3 Optical Suppression

While early experiments concentrated on studying the frequency and laser intensity dependence of PA, recent years have seen significant progress in studying the phenomena of optical suppression. Collisions between a pair of atoms are suppressed by subjecting the atoms to a laser beam tuned above ($\Delta > 0$) the atomic resonance. We again turn to a semiclassical model to get a feel for the phenomena. For weak fields, when the period of the Rabi frequency Ω is long compared to the collision time, the semiclassical theory is a reasonable model. At higher field intensities, the collision time becomes comparable to the Rabi period so that stimulated emission and multiple absorptions complicate the model and will be treated in more detail later. When the atomic separation reaches the Condon point $\mathcal{R}_S$, where the photon energy equals the difference between the ground- and repulsive excited-potentials, the atoms are promoted to a repulsive level

$$\mathrm{Na} + \mathrm{Na} + \hbar\omega_L \longrightarrow \mathrm{Na}^* + \mathrm{Na}. \tag{5.8}$$

The force exerted on the atoms by the repulsive potential, given by Eqn. 5.2, slows the approach of the atoms and reroutes the pair from the inner regions of the potential as shown in Fig. 5.2, suppressing the rate of collisions occurring within

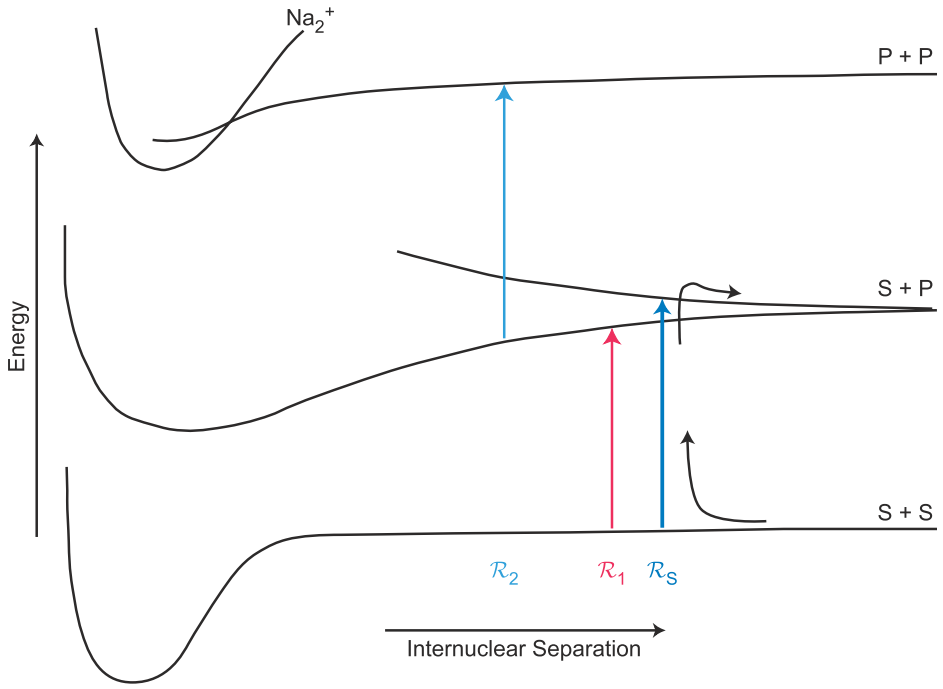

Figure 5.2: Optical Suppression of PAI. If the atom absorbs a photon tuned to the blue of the atomic resonance that couples the pair to the excited, repulsive state at a larger Condon radius ($\mathcal{R}_S$) than the photoassociation radius ($\mathcal{R}_1$), the flux is routed away from the inner region.

the suppression Condon point $\mathcal{R}_S$ Incomplete optical shielding can occur if the flux does not get excited to the repulsive level or if the excited atom spontaneously decays prior to complete deceleration of the relative approach because of the remaining velocity.

An example of a suppressible collision is photoassociative ionization. By setting the laser frequencies such that $\mathcal{R}_S$ is larger than $\mathcal{R}_1$, the rate of excited-state molecules is decreased by the rerouting of the atoms from the inner part of the potential. The suppression of the photoassociative ionization rate by a factor

of over an order of magnitude [67–70] has been observed. Trap loss collisions have also been suppressed with blue-detuned light in MOTs [71–73].

5.2 Early Suppression Experiments

5.2.1 Experimental Investigations

Most investigations of optical suppression have been performed with sodium [67–70, 73]. A few experiments in suppressing Penning ionization in metastable noble gases [71, 72] have been performed, but these systems have not been studied in as much detail. Presented here is an overview of recent experimental studies of optical suppression of photoassociative ionization (PAI) in laser cooled sodium.

Marcassa, *et al.* [67] in 1994 first demonstrated the suppression of PAI in a sodium MOT. A MOT containing sodium atoms cooled to approximately the Doppler limit T_D. A probe laser with scanning frequency ω_p scanned over several GHz near the $3\ ^2S_{1/2}$ [2] $\longrightarrow 3\ ^2P_{3/2}$ [3] atomic resonance. When $\omega_p < \omega_0$, i.e. to the red of the resonance, Na_2^+ ions were produced by PAI. The rate of ion production was measured as a function of the probe frequency. An optical suppression laser beam with frequency ω_S, with detuning $\Delta_S \approx +600$ MHz, was then passed through the MOT and the ion rate was again measured. The two scans are shown in Fig. 5.3a. When the probe frequency was tuned so that the internuclear separation corresponding to the Condon point for the suppression laser ($\mathcal{R}_S$) was larger than the photoassociating probe ($\mathcal{R}_P$), the ion rate decreased. But when $\mathcal{R}_P$ exceeded $\mathcal{R}_S$, an increase in ion production occurred because more atomic flux was delivered to the doubly excited state.

In a follow-up to the initial paper on suppression in sodium, Marcassa, *et*

al. [68] measured the suppression of PAI collisions as a function of the suppression laser intensity. As in the earlier suppression experiment [68], the ionization rate decreases when the Condon point for suppression exceeded that for photoassociation. The suppression and photoassociation lasers were tuned 600 MHz to the blue and 1 GHz to the red of the atomic resonance, respectively. The penetration measure $P_S(I)$, the ratio of ion production rate with the suppressor on to the rate with it off, was calculated as the intensity of the suppression laser was decreased over several steps. The ionization rate was strongly dependent upon the intensity of the laser, as shown in Fig. 5.3b.

Zilio, *et al.* [69] investigated the polarization dependence of suppression in a sodium MOT. The fractional ionization rate was measured for two different polarization cases, circular and linear, of the suppression laser beams. The suppressor beam, tuned 590 MHz above the atomic resonance, was stepped through several intensities. Circularly polarized light suppressed the ionization rate more than linearly polarized light at high suppression intensities, but the two cases converged at low optical field intensity. Figure 5.4a shows $P_S(I)$ for the two different polarization cases.

Optical suppression also reduces trap loss collisions within optical traps. Two colliding atoms can undergo a hyperfine-changing collision where one of the ground-state atoms changes state $3\ ^2S_{1/2}\ [2] \longrightarrow 3\ ^2S_{1/2}\ [1]$. For a weak optical trap, the kinetic energy released by this collision exceeds the trap depth and both atoms are ejected from the trap. Muniz, *et al.* [73] showed that the introduction of an optical suppression laser reduced the loss rate. Figure 5.4b shows the trap loss suppression factor $\Theta(I)$ as a function of suppression laser intensity. The suppression factor $\Theta(I)$ equals $1 - P_S(I)$. Similar to the suppression of PAI,

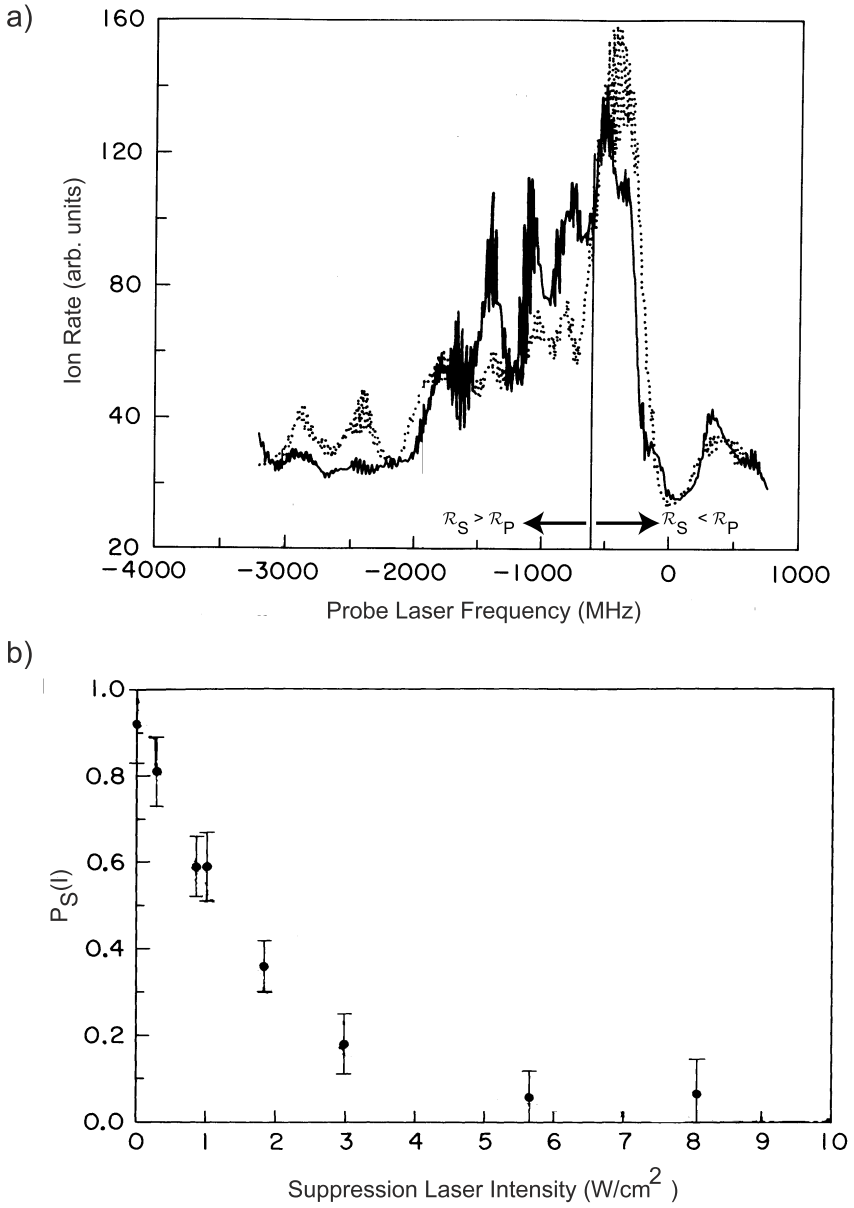

Figure 5.3: a) Ion rate as a function of frequency with suppressor laser on (dotted) and off (solid). The line indicates the frequency when the ordering of the Condon points change. Adapted from [67]. b) Penetration measure $P_S(I)$ as a function of intensity in a sodium MOT. Adapted from [68].

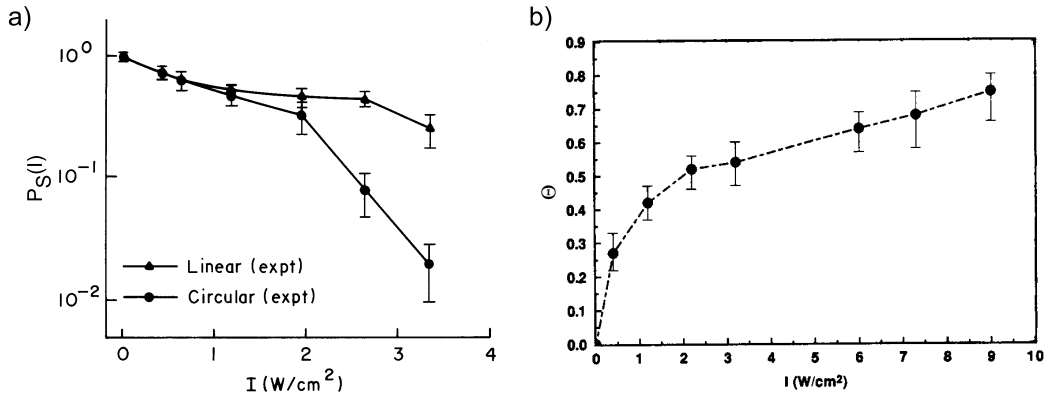

Figure 5.4: a) Penetration measure $P_S(I)$ for suppression of PAI as a function of intensity for circular (closed circles) and linear (closed triangles) polarizations. Adapted from [69]. b) Suppression factor $\Theta(I)$ for hyperfine-changing collisions in a weak sodium MOT as a function of intensity. Adapted from [73].

higher intensities lead to greater suppression of collisions.

The polarization dependence of suppression observed by Zilio, *et al.* [69] was insensitive to orientational effects because atoms in a MOT spatially average the collision axis due to the isotropic nature of the environment. To probe the polarization dependence further, the collision axis must be fixed in the laboratory frame, a highly collimated beam provides such an environment, as discussed in Chapter 1. Tsao, *et al.* [70] measured $P_S(I)$ as a function of intensity and polarization and is shown in Fig. 5.5. A longitudinally cooled sodium beam, with transverse velocity $v_\perp$ much less than the longitudinal velocity $v_\parallel$, restricts the collision axis to within a few milliradians of the beam axis. The suppression laser polarization $\overrightarrow{\varepsilon}$ was either parallel or perpendicular to the collision axis. Parallel polarization suppressed PAI less effectively than perpendicular polarization, particularly at high suppression laser intensities.

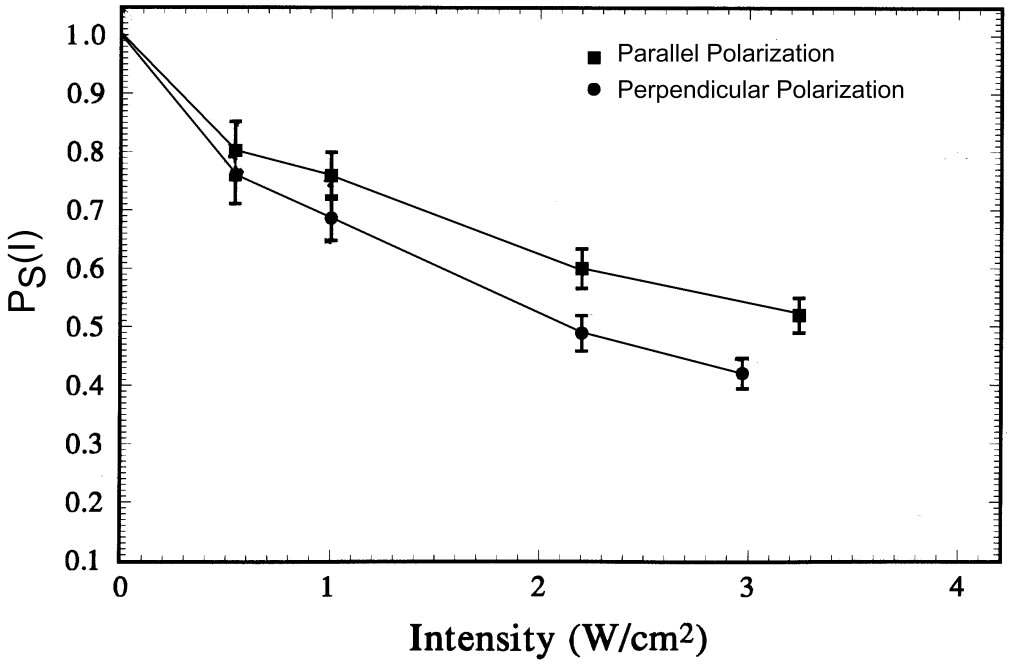

Figure 5.5: Penetration measure $P_S(I)$ as a function of intensity and of angle between collision axis and suppression field axis. For the parallel case (squares) the collision and suppression field axes are aligned. The axes are orthogonal for the perpendicular case. The lines are drawn to guide the eye. Adapted from [70].

5.2.2 Theoretical Investigations

While the picture of optical suppression presented above qualitatively explains the phenomena, it does not actually model the process. Two approaches to modeling optical suppression exist, semiclassical and quantum. The simplest to understand, the semiclassical approach, developed out of a one-dimensional (1D), two-state Landau-Zener model of avoided crossing [74]. Subsequent corrections to the model add angular momentum and polarization effects not considered in 1D [75, 76]. Quantum models developed at roughly the same time frame,

initially in 1D [74] and later expanded to three dimensions (3D) to include angular momentum and polarization [69, 77]. The different models are summarized in Table 5.1.

The 1D, two-state Landau-Zener model (1D L-Z) is a semiclassical way of treating the probability of penetrating through a potential crossing. In a dressed state picture [20], the suppression light field couples with the molecular potentials as shown in Fig. 5.6, leading to an avoided level crossing at the suppression Condon radius $\mathcal{R}_S$. Incoming scattering flux enters the collision on the ground state and the probability of penetrating through the crossing to the inner region where inelastic collisions occur (either PAI or trap loss collisions) is given by

$$P_{gr} = \exp\left(-\frac{2\pi\hbar\Gamma^2}{\upsilon_r(\mathcal{R}_S)\,|D(\mathcal{R}_S)|}\frac{I}{I_0}\right) \tag{5.9}$$

where $\upsilon_r(\mathcal{R}_S)$ is the relative velocity for the pair of atoms at the Condon point and $D(\mathcal{R}_S)$ is the slope of the difference between the ground and excited potentials at the Condon point. Because the ground state potential ($\propto R^{-6}$) is essentially flat compared to the excited state ($\propto R^{-3}$), $D(\mathcal{R}_S)$ simplifies to

$$\begin{aligned} D(\mathcal{R}_S) &= \left.\frac{\partial\left[V_{ex}(R) - V_{gr}(R)\right]}{\partial R}\right|_{R=\mathcal{R}_S} \\ &\simeq -\frac{3C_3}{\mathcal{R}_S^4}. \end{aligned} \tag{5.10}$$

The probability of population transfer to the excited state and rerouting scattering flux away from the inner regions and exiting on the repulsive excited state, is P_{ex} $(= 1 - P_{gr})$. Assuming the suppression laser has no other influence on the system, there is a fixed probability of an inelastic collision occurring within the separation $\mathcal{R}_S$. As a consequence, the experimental penetration measure $P_S(I)$ equals the penetration probability P_{gr} from the 1D L-Z model. Within the 1D L-Z, the suppression is more efficient at low collision temperatures (low relative

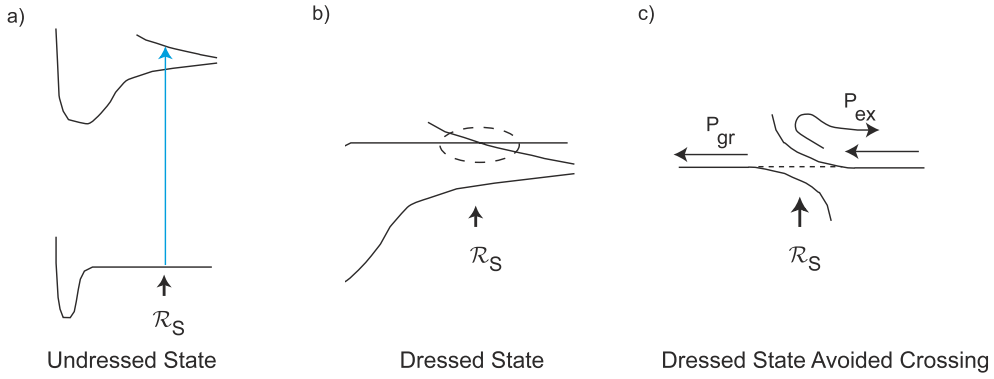

Figure 5.6: 1-D Landau Zener model of optical suppression. The suppression process in a) undressed and b) dressed state pictures. In the dressed state, the energy of the photon is added to the ground state energy. c) An avoided crossing occurs at the Condon point $\mathcal{R}_S$ that broadens with increased laser intensity.

velocity) and at high optical field intensity as shown in Fig. 5.7. For low suppression laser intensities, the model agrees with experimental results. However, in the high field case, the 1-D L-Z model diverges from the experimentally measured penetration that is clearly non-exponential [68–70, 73]. This model also fails to predict the polarization dependence of suppression [69, 70].

Yurovsky and Ben-Reuven have presented a multidimensional Landau-Zener model (3D L-Z) with multiple levels and crossings due to the inclusion of partial waves $\widetilde{\mathbf{J}}$ in the scattering process [75, 76]. By adding angular momentum, polarization effects can also be studied. The colliding pair may penetrate to the inner region of the potential on different channels than the entrance channel, as shown in Fig. 5.8, because of multiple potential crossings. In addition to penetrating through a crossing unperturbed, there are intuitive and counterintuitive pathways. In the intuitive pathways, the atoms always move towards each other

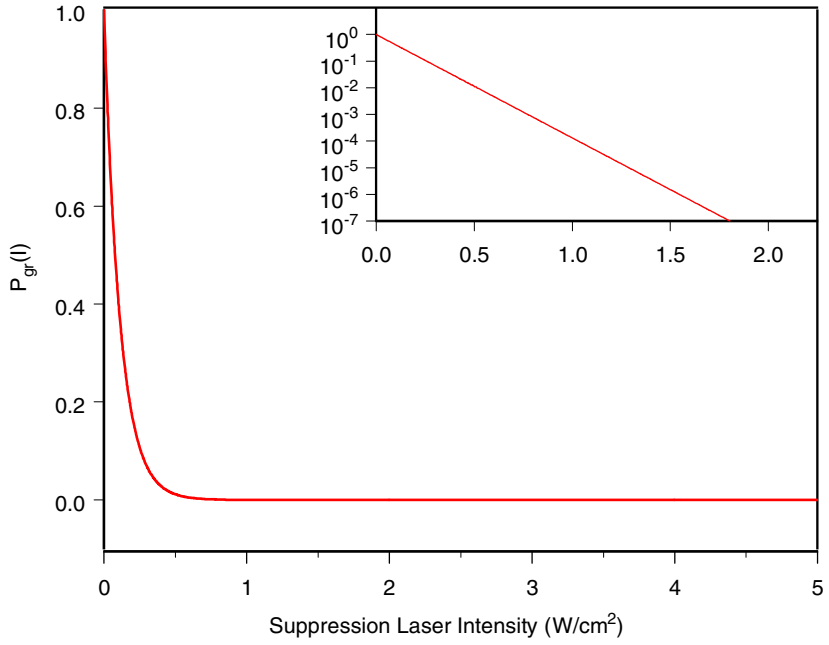

Figure 5.7: Intensity dependent penetration probability, in 1D L-Z model, for sodium ($\mathcal{R}_S = 625a_0$, $v_r = 3$ m/s).

and result in an increasing partial wave contribution:

$$\left|1, \widetilde{\mathbf{J}}\right\rangle \longrightarrow \left|2, \widetilde{\mathbf{J}}' = \widetilde{\mathbf{J}} + 1\right\rangle \longrightarrow \left|1, \widetilde{\mathbf{J}} + 2\right\rangle . \tag{5.11}$$

The relative velocity for atoms following a counterintuitive pathway changes twice as the atoms briefly move away from each other. The partial wave of the collision decreases for a counterintuitive pathway:

$$\left|1, \widetilde{\mathbf{J}}\right\rangle \longrightarrow \left|2, \widetilde{\mathbf{J}}' = \widetilde{\mathbf{J}} - 1\right\rangle \longrightarrow \left|1, \widetilde{\mathbf{J}} - 2\right\rangle . \tag{5.12}$$

Yurovsky and Ben-Reuven propose that the multiple pathways, to the region where inelastic collisions occur, interfere due to a phase shift between the competing pathways. The interference leads to a saturation of the suppression at high intensity and polarization dependence of suppression not present in the 1D

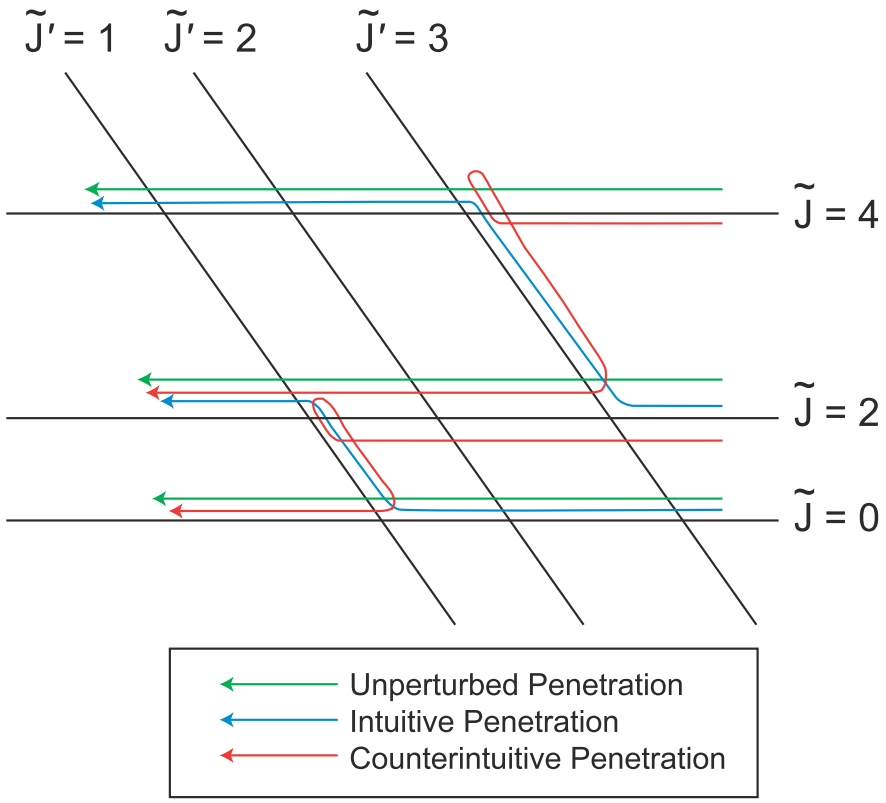

Figure 5.8: 3-D Landau Zener model of optical suppression.

L-Z model. With a "properly chosen" phase shift, the 3D L-Z qualitatively agrees with the intensity and polarization results of Tsao, *et al.* [70, 76], but no independent criteria for the phase shift exists.

Suominen, *et al.* [74], proposed a quantum close coupling (QCC) model of optical suppression. The QCC uses three channels, the ground-state, excited-state, and an artificial loss channel (the artificial channel serves as a detection probe at close range), coupled by a light field treated as a perturbation in the weak coupling regime. The angular dependence of the physics was not considered

in this one-dimensional model: the Clebsch-Gordon coefficients were averaged over all $\mathbf{J}$ and $M_{\mathbf{J}}$. At low field intensities, the QCC agrees with the 1D L-Z model. At higher intensities, the agreement begins to fade as the 1D L-Z predicts slightly more efficient suppression than QCC. However, the QCC model still predicts practically complete shielding of the atoms, contrary to experimental measurements [68–70, 73].

It became clear that the failure of the QCC model to predict the incomplete shielding and polarization dependence was the result of the limitation of the model to a single dimension. Napolitano, *et al.* [77] developed a simplified three-dimensional quantum close coupling (3D QCC) model of optical suppression. The 3D QCC model employs five states and uses accurate sodium molecular potentials including multiple partial waves on each potential. Like the one-dimensional QCC model, an artificial channel at small atomic separation serves as a probe. The electric field treatment in the 3D QCC model is exact, considering the intensity and polarization of the suppression laser beam without approximation. For the calculations to remain tractable, spin and hyperfine structure are ignored.

The amount of suppression predicted by the 3D QCC model depends upon the suppression laser polarization because the light couples to the different channels with a strength that varies as the laser polarization changes. In the isotropic environment of a MOT, the 3D QCC model agrees with the results of Zilio, *et al.* [69], where a circular polarized laser beam suppresses penetration to the inner region more efficiently than linear polarization as shown in Fig. 5.9a. In an environment where a well defined collision axis permits the alignment of the suppression field to be studied, an anisotropy in the strength of suppression is

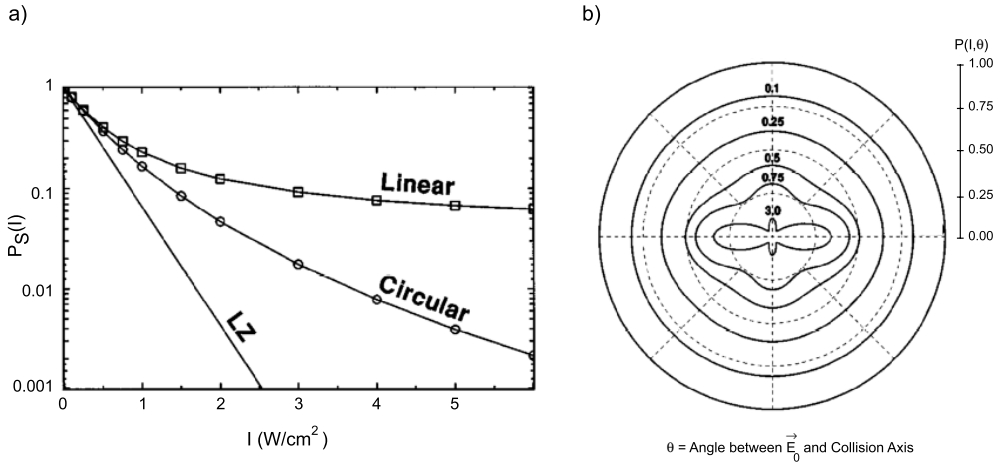

Figure 5.9: 3-D Quantum Close Coupling model. a) Optical suppression in a sodium MOT is more efficient for circular polarization than for linear polarization. Both polarization cases shield predict less suppression than the 1D L-Z model. b) The degree of suppression as a function of the angle between the suppression laser field ($\overrightarrow{E_0}$) and the collision axis. The suppression is anisotropic at high laser intensities (numbers along vertical axis). Adapted from [77].

observed for the case of high intensity suppression fields. Figure 5.9b shows the penetration probability as a function of the angle between the field polarization axis and the collision axis for several suppression laser intensities for $T_{coll} = 240$ μK, typical for the case of a MOT. The anisotropy is quite pronounced at high intensity, where a dominate feature near 60° appears. The feature corresponds to a maximum in suppression efficiency. While T_{coll} here is much lower than in the experiments by Tsao, *et al.* [30], the theory does correctly reflect the difference in the suppression measure between parallel ($\theta = 0°$) and perpendicular ($\theta = 90°$) polarization of the suppression beams (see Fig. 5.5).

	1D L-Z	3D L-Z	QCC	3D QCC
Type	Semiclassical	Semiclassical	Quantum	Quantum
Key Points	Weak Field Coupling Local Interaction No Angular Momentum	Weak Field Coupling Local Interaction Arbitrary Phase No Angular Momentum	Perturbative Field Treatment Three States Spin Ignored	Exact Field Treatment Five States Spin Ignored
Prediction	Angle-averaged, Weak-field Penetration Measure	Weak-field Penetration Measure	Angle-averaged, Weak-field Penetration Measure	Penetration Measure (Including angular dependence and high field)

Table 5.1: Comparison of different models of suppression.

5.3 Experiment

The two 3D models of optical suppression, 3D L-Z and 3D QCC, both predict that the penetration probability depends on the alignment of the suppression polarization axis with respect to the collision axis. While the experiment by Tsao, *et al.* [70] probed two distinct polarization orientations, most of the distribution remained unstudied because of the low density in their atomic beam. Several hours of data collection and significant counting statistics were required for each data point shown in Fig. 5.5. Measuring the optical suppression as a function of angle was not practical. With the development of the cool, bright sodium beam described in Chapter 4, measuring the suppression as a function of angle was finally possible so that the theory of Napolitano, *et al.* [77] could be tested. In this section, the experiment for measuring the angular dependence of optical suppression is described. Figure 5.10a summarizes the experimental layout.

5.3.1 Lasers

The three ring dye lasers described in detail in Section 3.1 are all used in this experiment. The first 899-21 ring dye laser optically collimates the atom beam as described in Chapter 4. The collimation laser frequency ω_{Coll} is referenced to a saturation absorption spectra. The 380D, also referenced to a saturated absorption spectrum, serves as the longitudinally slowing laser ω_C (Section 4.3.3) and also provides the laser beam ω_1 used to photoassociate sodium atoms within the beam. The laser frequency of ω_1 is tuned to the desired frequency by taking advantage of the Doppler effect and will be described in detail below. The second 899-21 serves multiple roles. Initially, it is used as a probe laser to measure the density and longitudinal velocity distributions as discussed in Chapter 4. Once

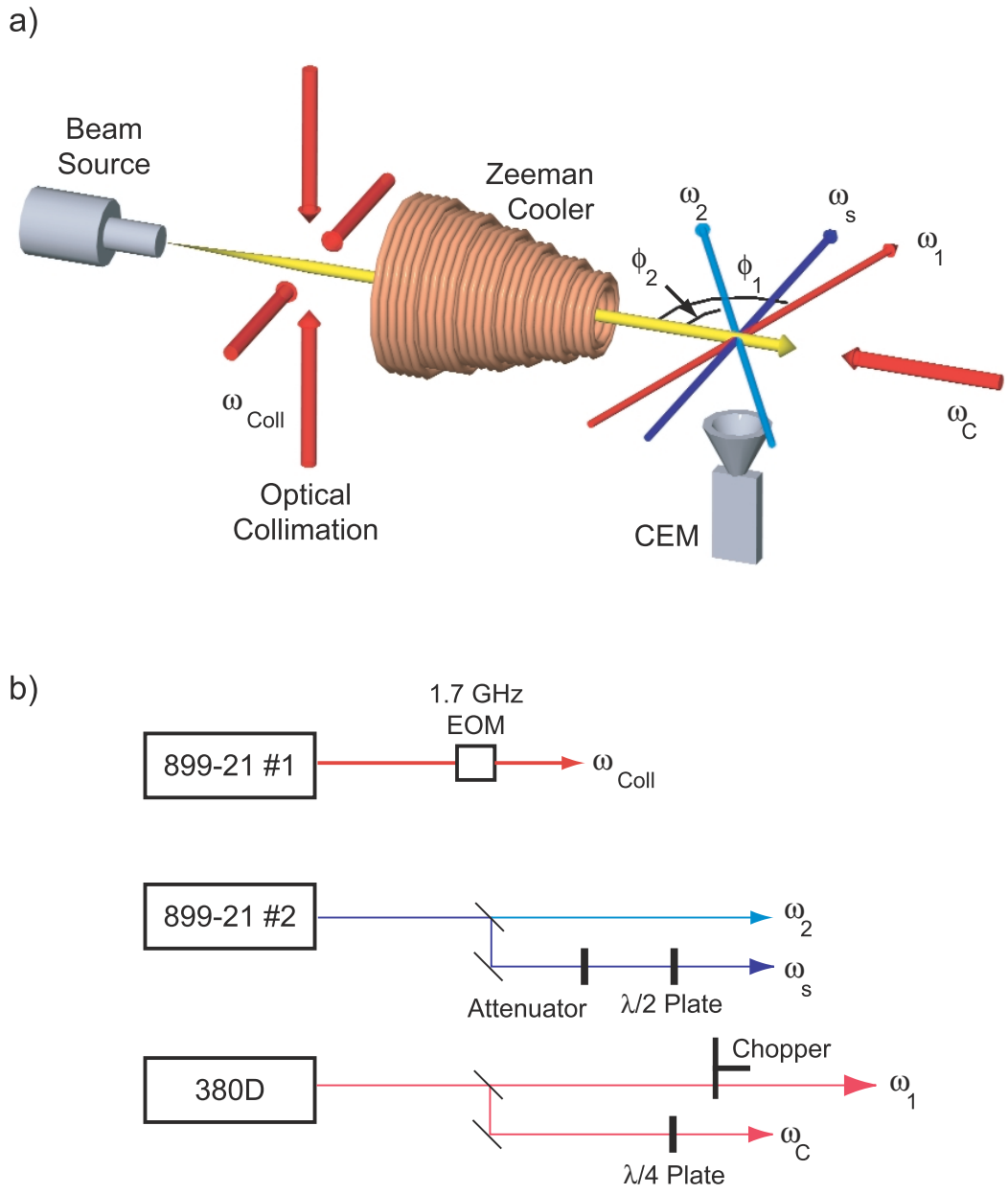

Figure 5.10: Overview of experiment. a) The sodium beam is optically collimated, longitudinally slowed, and then subjected to ω_1, ω_2, and ω_S. Ions are detected with a channel electron multiplier (CEM). b) The sources of the different laser frequencies used in the suppression experiment.

the sodium beam is characterized, the output from the 899-21 is divided to serve as both the suppression laser ω_S and the ionization laser ω_2. The ionization laser also takes advantage of the Doppler shift to tune the frequency in the frame atoms in the beam. An iodine cell serves as the frequency standard for this laser. Figure 5.10b summarizes the production of the different laser beams.

5.3.2 Atom Beam

The apparatus described in detail in Chapter 4 produces the collimated, dense atom beam in which the optical suppression experiment is performed. For convenience, the beam characteristics are summarized here. Atomic flux is generated by externally heating a reservoir (395°C) containing sodium metal. The flux exits a small aperture (1.25 mm diameter) and is mechanically collimated by a second 1.25 mm diameter aperture (the skimmer) 16 cm downstream from the first (Section 4.3.1). Rejected atoms are pumped away by a diffusion pump and a cryopump mounted in between the apertures. Ten centimeters downstream from the skimmer, optical molasses collimates the beam by damping the transverse velocity $v_\perp$ to about 25 cm/s (Section 4.3.2). The collimated sodium beam enters the tapered solenoid where it is subject to a counter-propagating laser with frequency ω_C. Sodium atoms slow as they scatter photons out of the laser beam which is kept in resonance with the atoms by compensating for the Doppler shift with a spatially varying magnetic field generated by the tapered solenoid operating with total current of 58 A (Section 4.3.3). The flux slows to $v_\parallel = 350$ m/s at which point a magnetic shielding assembly mounted coaxially with the beam decouples the atoms from the cooling cycle. Rapidly extracting the atoms from the cooling cycle results in the narrow longitudinal velocity distribution

($\Delta v_{\|} = 5$ m/s) necessary for cold collisions (Section 4.3.4). The atom beam enters the interaction chamber where it is characterized and optimized using the diagnostic techniques described in Section 4.4. The beam density n is 7×10^8 cm^{-3} with a collision temperature T_{coll} of 4 mK.

5.3.3 Collision Experiment

After the sodium beam performance is checked and verified, the photoassociation ω_1, ionization ω_2, and suppression ω_S lasers are introduced to the interaction chamber. The three laser beams intersect the sodium beam in a common plane at a point directly above the channel electron multiplier (CEM). Located above the intersection is a repeller plate and below is an Einzel lens; the exact positions of the ion optics are described in detail in Section 3.6.3.

The frequencies exiting the laser head are not exactly at the desired frequency. Rather than investing in several AOMs to deflect and shift the output to produce ω_1, ω_2, and ω_S, a Doppler tuning technique allows the frequencies to be shifted. When a laser beam crosses a well collimated ($v_{\perp} \approx 0$) atom beam with longitudinal velocity $v_{\|}$ at an angle ϕ, the laser frequency Doppler shifts by an amount given by

$$\Delta\omega_D = \frac{2\pi v_{\|}}{\lambda} \cos\phi \tag{4.15}$$

as given earlier in Section 4.4.2. Changing the optical paths by moving the steering mirrors shifts the incident angle ϕ which changes the laser frequency in the atomic frame. The Doppler tuning technique has several advantages other than the cost savings. It prevents atoms from photoassociating in the hot background because the photoassociation laser frequency ω_1 shifts outside of the resonant absorption range needed for PAI. Another advantage of introducing

Laser Beam	Laboratory Frame	ϕ	Atomic Frame
ω_1	-220 MHz	$105°$	-370 MHz
ω_2	$+270$ MHz	$61°$	$+555$ MHz
ω_S	$+270$ MHz	$90°$	$+270$ MHz

Table 5.2: Laser frequencies in laboratory and atomic frames.

ω_1 and ω_2 at an angle is that the independent steering control simplifies the process of overlapping the laser beams on of atom beam. Table 5.2 summarizes the frequencies of ω_1, ω_2, and ω_S in the two reference frames as well as their incidence angles. The cooling laser is also present in the overlap region and it is ignored in the treatment of the system for two reasons. In the atomic frame of reference, the frequency of this laser is shifted up from -220 MHz in the lab frame to $\sim +400$ MHz and the Condon point for the coupling to the excited repulsive state will be smaller than the PAI radius. Also, the intensity of the field at the interaction region is small ($I_C \sim 150$ mW/cm^2) compared to the other beams. The Condon points for the suppression, photoassociation, and ionization steps are given by the detuning and the C_3 coefficients for the excited states. For the long range molecule, we can estimate the potential as a linear combination of the singlet Σ and the triplet Π states of Na_2^*, weighted $\frac{2}{3}$ and $\frac{1}{3}$, respectively, given approximately by $C_3 = 9.98\ hartree \cdot a_0^3$. From the C_3 coefficient, we estimate the Condon points for suppression $\mathcal{R}_S$ and photoassociation $\mathcal{R}_1$ to be 625 a_0 and 560 a_0, respectively. The excited state molecule is coupled to the doubly excited level at 490 a_0. Figure 5.11 shows the potentials and Condon points under these experimental conditions.

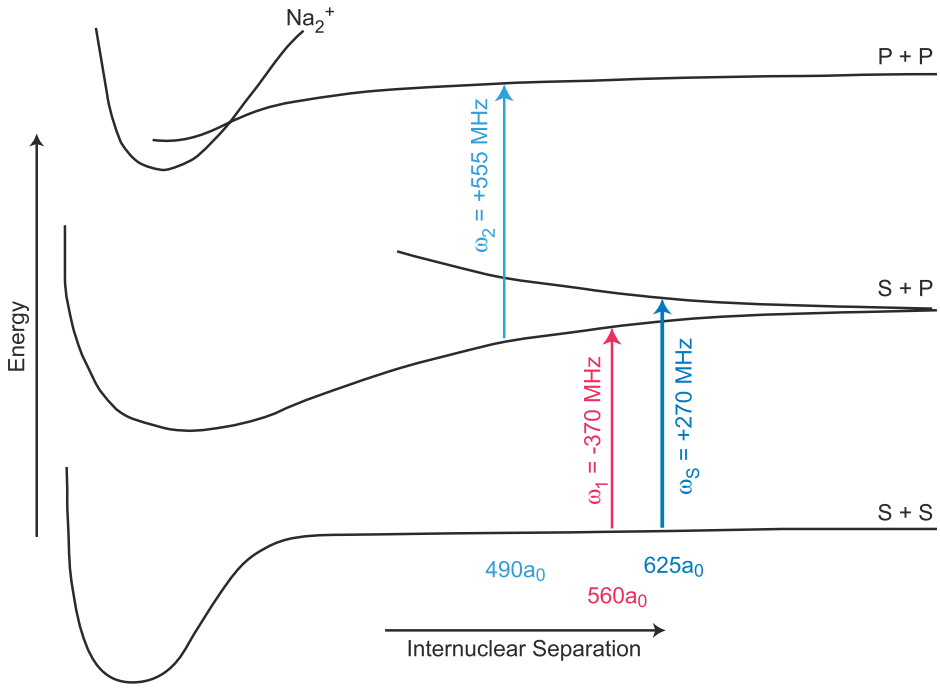

Figure 5.11: Frequencies, in frame of cooled atoms, and Condon radii for the three laser frequencies in the suppression experiment.

Each laser beam passes through a telescope to reduce the beam diameter to 2 mm prior to entering the vacuum chamber through anti-reflection coated windows. The intensity of ω_1 and ω_2 are 3 W/cm^2 and 2.5 W/cm^2, respectively. The intensity of the suppression laser ω_S is 2.5 W/cm^2 for the high suppression intensity case and 0.6 W/cm^2 for the low intensity case. A neutral density filter placed in the beam path attenuates the suppressor beam for the low intensity case.

The laser light leaving the 899-21 is polarized vertically (s-state). After passing multiple reflections from steering mirrors and beam splitters, as well as

passing through the telescope, the polarization purity degrades. Immediately after the telescope, the suppression laser ω_S passes through a linear polarizer to clean up the polarization. A half wave ($\lambda/2$) plate, mounted in a calibrated rotary mount, inserted into the beam path after the linear polarizer rotates the polarization by rotating its optical axis. Rotating the $\lambda/2$ plate over a 90° range rotates the polarization of the laser by 180°. The PAI laser beams, ω_1 and ω_2, are not conditioned by any polarizing elements after exiting the laser.

The CEM detects any ions produced, it is unable to distinguish between Na_2^+ and Na^+ in the current setup, but cold Na_2^+ formation only occurs after photoassociation by ω_1. To remove background Na^+ ion signal produced by the presence of blue detuned laser beams, we pass ω_1 though an 150 Hz optical chopper that produces PAI-on and a PAI-off periods. Subtracting the PAI-off from the PAI-on yields the PAI signal because both periods have background signal, but only the latter also contains the desired signal. After passing through the atom beam, ω_1 exits the interaction chamber through a window and illuminates a photodiode. The photodiode signal acts as the master clock to synchronize the ion counter (Stanford Research Systems, SR400). The SR400 has two built in channels, A and B. The rising slope of the photodiode signal triggers begins the timing cycle for the two channels. Channel A opens for 2 ms after a 0.7 ms delay and counts signal plus background, channel B records the background by opening for 2 ms after a 4.2 ms delay. Figure 5.12 shows the timing diagram for the photon counter. Each channel continuously sums for 2500 periods before the number of ions is written out to a PC for analysis. Each 2500 period cycle is referred to as a single count. Therefore each count measures the number of ions produced via PAI within a 5 s interval. At each angle and intensity we collect $\mathcal{N}$ counts for

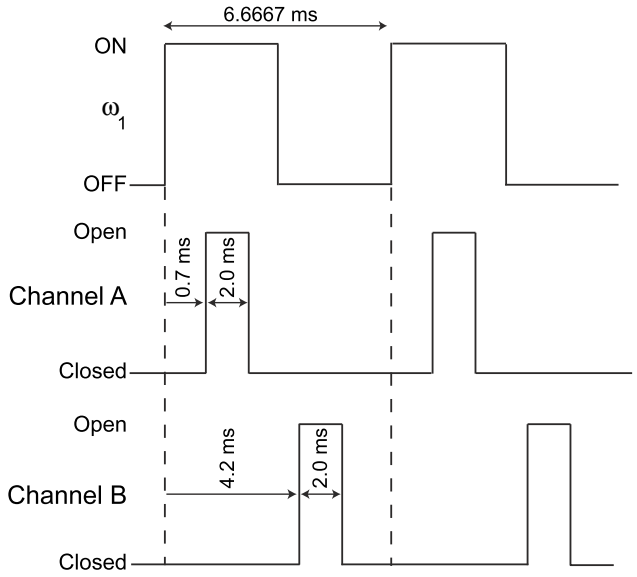

Figure 5.12: Timing diagram for PAI counting.

each channel.

To determine the average ion rate for a particular angle and intensity, a simple averaging is performed:

$$\overline{\mathrm{A}} = \frac{1}{\mathcal{N}}\left(\mathrm{A1} + \mathrm{A2} + \cdots\right) \tag{5.13}$$

where Ai is the number of ions in the i^{th} count. For each count, the uncertainty is given by $\sigma_{\mathrm{A}i} = \sqrt{\mathrm{A}i}$, and the total uncertainty for the total number of counts is [78]

$$\begin{aligned}\sigma_{\overline{\mathrm{A}}} &= \sqrt{\left(\frac{\sigma_{\mathrm{A1}}}{\mathcal{N}}\right)^2 + \left(\frac{\sigma_{\mathrm{A2}}}{\mathcal{N}}\right)^2 + \cdots} \\ &= \sqrt{\frac{\mathrm{A1} + \mathrm{A2} + \cdots}{\mathcal{N}^2}} = \sqrt{\frac{\overline{\mathrm{A}}}{\mathcal{N}}}.\end{aligned} \tag{5.14}$$

The average and uncertainty for channel B is similarly calculated. The PAI rate is the difference between $\overline{\mathrm{A}}$ and $\overline{\mathrm{B}}$, so assuming no correlation between A and B,

the uncertainty in the PAI rate is given by the in quadrature sum of $\sigma_{\overline{\mathrm{A}}}$ and $\sigma_{\overline{\mathrm{B}}}$. For our customary five second counting window, the PAI rate and uncertainty is

$$i \text{ (ions/5 s)} = \left(\overline{\mathrm{A}} - \overline{\mathrm{B}}\right) \pm \sqrt{\frac{\overline{\mathrm{A}} + \overline{\mathrm{B}}}{\mathcal{N}}}. \tag{5.15}$$

To measure the normal PAI rate, the suppression laser beam ω_1 is blocked and the rate i_0 measured with just the photoassociation (ω_1) and ionization (ω_2) laser beams present. With the suppression laser present, we measure the PAI rate i_S as a function of the suppression laser intensity ($I_S = 0.6$ or 2.5 W/cm^2) and angle θ. The suppression laser polarization angle θ varies from $0 - 180^\circ$ in several steps. The penetration measure, or fractional ionization, is the ratio of the ion production rates:

$$P_S(\theta, I_S) = \frac{i_S}{i_0} \tag{5.16}$$

and the uncertainty in the penetration measure is

$$\sigma_{P_S} = P_S\left(\theta, I_S\right) \sqrt{\left(\frac{\sigma_{i_0}}{i_0}\right)^2 + \left(\frac{\sigma_{i_S}}{i_S}\right)^2}. \tag{5.17}$$

5.4 Results

Figure 5.13 shows the penetration measure P_S as a function of the angle between the collision axis and the suppression laser electric field for two different laser intensities (0.6 and 2.5 W/cm^2) on a polar plot for collision temperatures of 4 mK. For clarity, the uncertainty ($\pm\sigma_{P_S}$) in the data is plotted in Cartesian coordinates.

At low suppression laser intensity, the penetration probability is isotropic, within the experimental uncertainty. However, at high field, the angular plot

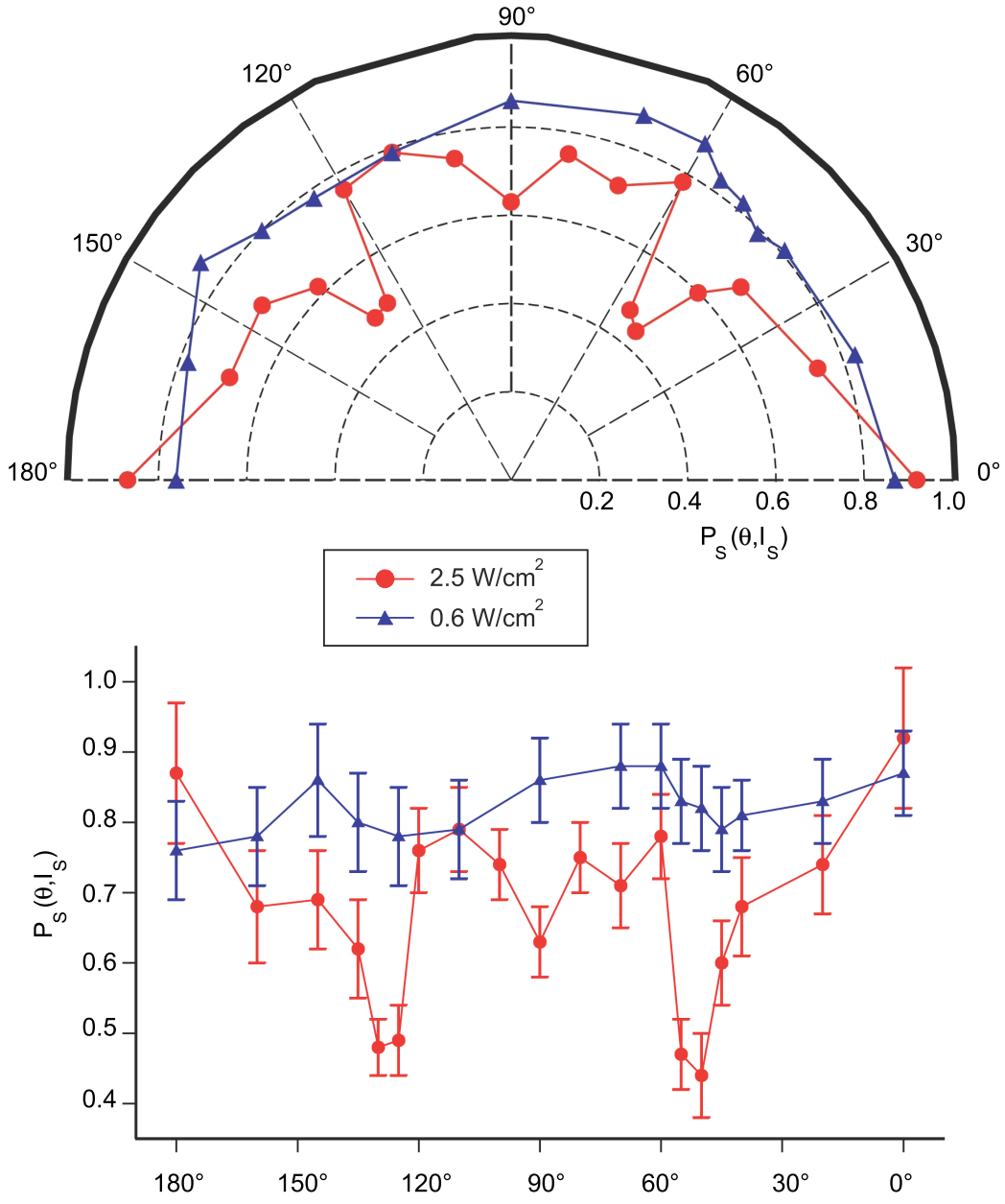

Figure 5.13: Fractional ionization as a function of the angle between the collision axis and electric field and of the suppression laser intensity. For clarity, the data is also plotted in Cartesian coordinates to show the error bars. At high suppression laser intensity, the degree of suppression shows strong anisotropy of suppression.

exhibits pronounced dips, larger than the uncertainty, in the penetration measure P_S around 55°, 90°, and 125°. The features at high field are also symmetric about 90°, this is expected because there is no difference, in the atomic frame, between light polarized at angles $90° + \Delta\theta$ and $90° - \Delta\theta$ with respect to the collision axis. By measuring between $0° - 180°$ rather than between $0° - 90°$, the symmetry of the data acts serves as a consistency check.

5.5 Theory

The 3D QCC model developed by Napolitano, *et al.* [77] predicts the anisotropy in the polarization dependence of optical suppression that is clearly seen in Fig. 5.13. When applying the theory to the experimental conditions presented here, qualitative discrepancies arise between the model and the experimental results. The structure predicted in the 3D QCC model arises from the dominance of a single partial wave, namely the d-wave. Because the collision is between a pair of identical bosons, only even partial waves ($\widetilde{\mathbf{J}} = 0, 2, 4, \ldots$) contribute to the scattering event. The structure in Fig. 5.9 exhibits a shape closely related to the $|\mathrm{Y}_{2,0}(\theta, \phi)|^2$ characteristic of a d-wave. Figure 5.14 shows the 3D QCC results for conditions similar to the high intensity case of the experiment presented here. The structure, while less dramatic at than the 240 μK shown in Fig. 5.9b, is still pronounced. Higher collision temperatures couple in more partial waves that smooth out the features, but the local maximum at 90° appears at both low and high collision temperatures. All of the even partial waves have a local maximum at 90°, but the clear local minimum at 90° in the experimental results indicates there is more physics occurring than considered in the 3D QCC model. In fact, a detailed re-examination of the work by Napolitano, *et al.* [77] revealed an error

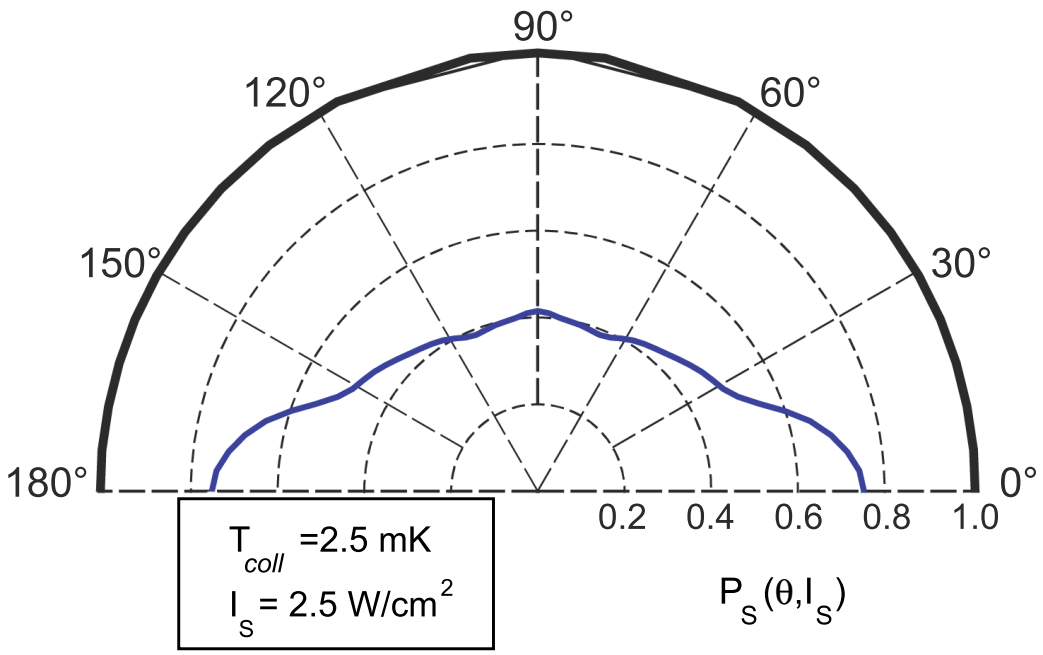

Figure 5.14: Three-dimensional quantum close coupling (3D QCC) model for penetration probability for conditions similar to the experiment presented in this chapter. The local maximum at 90° does not agree with the experiment.

that added the partial waves in an incoherent manner, rather than in a coherent fashion [79].

The error in the 3D QCC model is corrected by adding the scattering matrices for each partial wave prior to squaring, rather than squaring each first as in the 3D QCC model. The coherent 3D quantum close coupling model (Corrected 3D QCC) exhibits a dip in the penetration probability, for conditions similar to the experiment, as shown in Fig. 5.15. While the model does not quantitatively agree with Fig. 5.13, the magnitude and angles do not agree, the appearance of the decrease in penetration at 90° seems to be a signature of an interference effect between the different pathways that the Corrected 3D QCC model predicts.

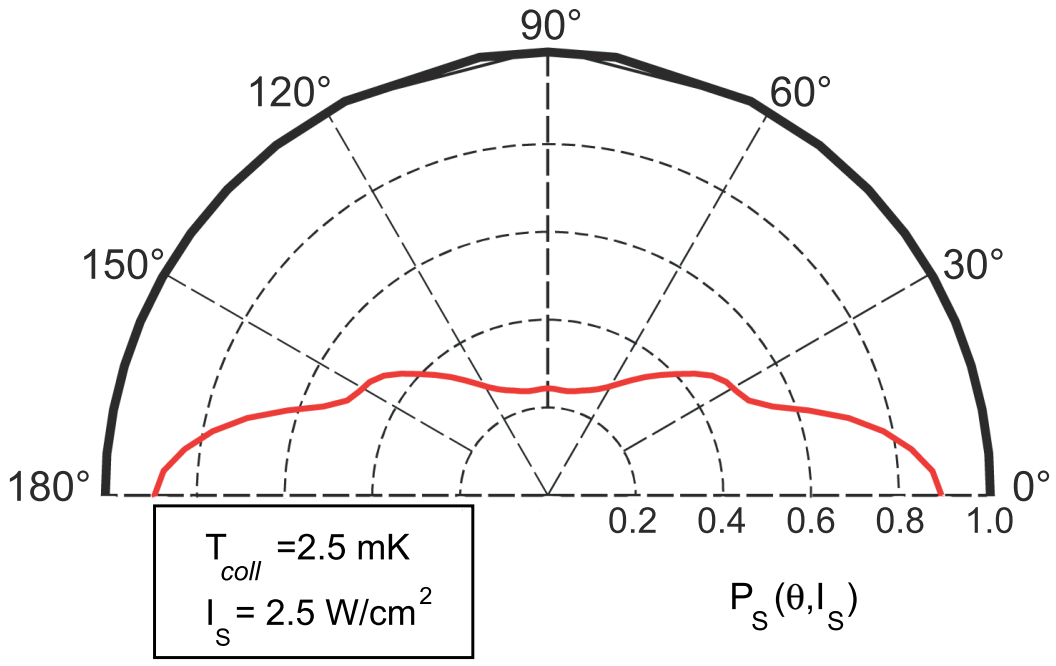

Figure 5.15: Corrected 3D quantum close coupling (Corrected 3D QCC) model for penetration probability for conditions similar to the experiment presented in this chapter. The model has been corrected to coherently sum the partial wave contributions. A local minium at 90° appears to be a signature of the coherent process.

The fact that even when corrected, 3D QCC model fails to quantitatively agree with the experiment should come as no surprise. Only five states are included in the QCC calculations: spin, fine-, and hyperfine structure have all been ignored. Including these effects would make calculations virtually intractable. The results may be particularly sensitive to the ground-state potential. There are indications that there is a d-wave shape resonance in the ground-state that occurs near $T_{coll} =$ 5 mK [80]; PAI experiments in a beam are currently underway to determine the effect it has on the collision [81]. We suspect that the difference in angular dependence between this data and the two polarization cases studied by Tsao *et*

al. [70] arises because of the presence of the d-wave resonance near the collision temperatures at which this work was performed.

To gain deeper insight into the process, more theoretical development is need. The ongoing development of computational power may allow additional states to be added to the 3D QCC model. We have also been informed that Yurovsky and Ben-Reuven are continuing to refine the 3D L-Z model [82].

Chapter 6

Summary and Discussion

In the work presented in this thesis, we produce a cold, dense, bright sodium beam specifically for the purpose of intrabeam collision studies. Atoms effusing from a novel externally heated thermal source are conditioned with several laser beams, producing a beam with a sub-Doppler transverse velocity component ($\Delta v_{\perp} < 50$ cm/s) and a narrow longitudinal distribution ($\Delta v_{\parallel} \sim 5$ m/s) centered about a finite laboratory velocity ($v_{\parallel} \sim 350$ m/s). The small velocity distribution, the result of rapidly decoupling the atoms from the cooling cycle by shielding a region of the vacuum chamber with high permeability foil, results in low energy intrabeam collisions aligned along the beam axis. The density in the beam exceeds 2×10^8 sodium atoms/cm^3 at the interaction region. While this technique is proven here for sodium, other alkali metals and metastable noble gas species can take advantage of the simple decoupling technique to produce a beam with narrow longitudinal velocities. A similar system using permanent magnets has been utilized in producing a cold cesium beam [49].

Using the beam described in Chapter 4, we studied the angular dependence of the optical suppression process. Changing the orientation of the electric field of a laser beam tuned to suppress photoassociative ionization collisions results in

a marked anisotropy in the suppression strength at high field intensity. At low fields ($I < 1$ W/cm^2), the suppression is isotropic. Higher optical field intensities allow higher order partial waves to contribute to the process and the anisotropy appears to be a coherent addition of the different partial wave pathways. While the angular dependence of optical suppression had been previously studied in a beam [70], low beam densities prevented a study of the same detail presented here.

This experiment is, to the author's knowledge, the first collision experiment performed in an optically brightened beam. However, the novelty of such an experiment will certainly be short-lived. The polarization dependence of the photoassociation process is currently underway in the region near dissociation (-5 GHz $\geq \Delta \geq 0$ GHz) by Ramirez-Serrano, *et al.* [41]. Photoassociative ionization spectra are obtained for three distinct polarization cases: parallel to the atom beam, perpendicular to the beam, and circular. Figure 6.1 shows preliminary results of the three spectra, showing strong polarization dependence as the selection rules change with the polarization. Ramirez-Serrano, *et al.* [83] also proposed that a bright, dense atom beam is a good environment for detecting cold molecules formed by the photoassociation process [84]. Optical brightening will, potentially, allow more detailed study of other intrabeam collisions, such as state-changing collisions [14], associative ionization [16], and energy pooling collisions [17] by increasing the density of atoms within the beam. This technique also presents opportunities in crossed beam experiments. Orientational collision effects between different species has been a fertile area of research [85–88] and can benefit by using highly collimated, monoenergetic beams. Changing the collision energy is possible by slowing the species to different terminal longitu-

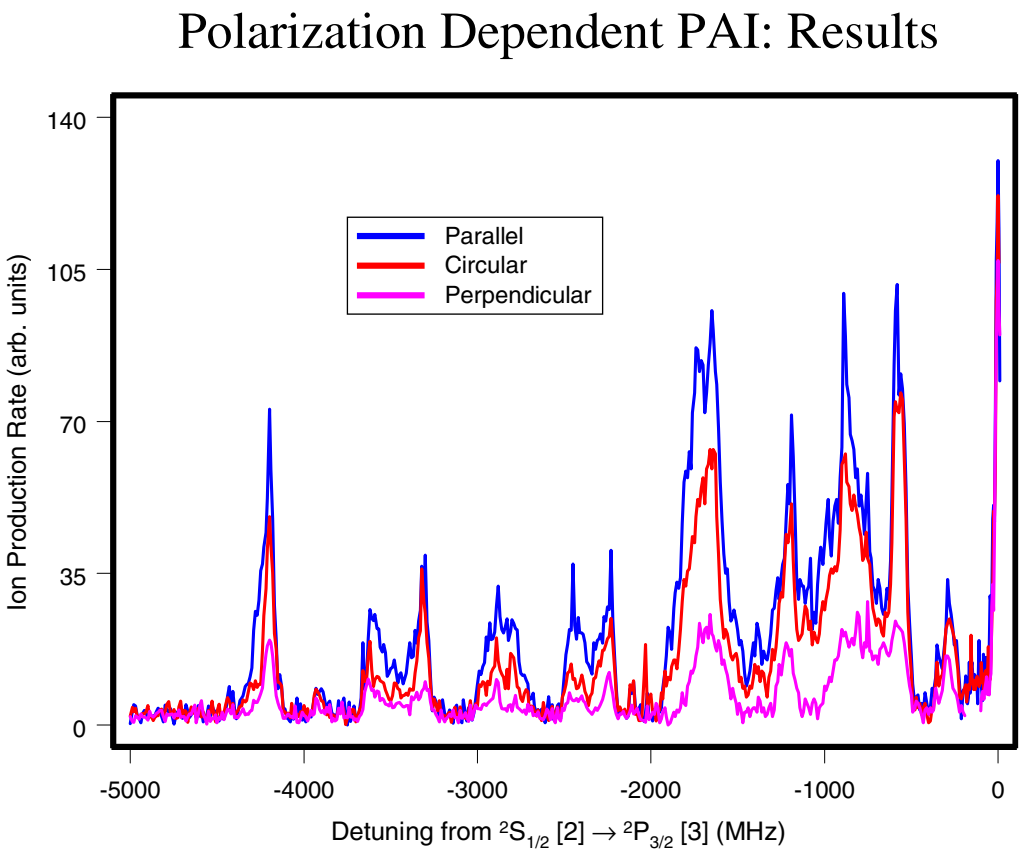

Figure 6.1: Polarization dependent photoassociative ionization (PAI) spectra below the D2 resonance in sodium. Courtesy of Jaime Ramirez-Serrano.

dinal velocities. Thermal averaging of the dynamics is significantly reduced by the narrow velocity distribution provided by rapid decoupling. Heteronuclear molecule formation is another process which might benefit from crossed, bright beams. By conservation of momentum, photoassociated molecules are removed from the beam axes and can be detected in a region absent of background flux.

Appendix A

Notations and Definitions

Parameter	Description
α	Damping coefficient
α	Collision acceptance angle
α_{FS}	Fine structure constant $\left[\sim \frac{1}{137}\right]$
A	Ion counts [PAI + Background]
β	Restoring coefficient
β	Beam divergence angle
B	Magnetic Field
B	Brilliance $\left[= R\frac{v_{\parallel}}{\Delta v_{\parallel}}\right]$
B	Ion counts [Background]
c	Speed of light [3×10^8 m s^{-1}]
C_i	Long-range potential coefficients
d	Beam diameter (FWHM)
$\overrightarrow{d}$	Transition dipole moment
$\widetilde{d}$	$\overrightarrow{d} \cdot \overrightarrow{\varepsilon}$
$\delta\omega_D$	Doppler linewidth (FWHM)
$\delta\omega_L$	Laser bandwidth (FWHM)

Parameter	Description
Δ	Detuning from resonance $[= \omega_L - \omega_0]$
$\Delta\varepsilon_{HF}$	Hyperfine energy shift
$\Delta\varepsilon_M$	Zeeman energy shift
$\Delta\varepsilon_{SO,\mathbf{J}}$	Spin-orbit energy shift
$\Delta\omega_D$	Doppler frequency shift $[= -k_L \cdot \upsilon_A]$
$\Delta\upsilon_{\parallel}$	Longitudinal velocity spread
$\Delta\upsilon_{\perp}$	Transverse velocity spread
e	Electron charge $[= 1.6 \times 10^{-19}$ C$]$
$\overrightarrow{\varepsilon}$	Polarization vector
E_0	Electric field amplitude
E_i	Energy of state i
$\overrightarrow{E}$	Electric field $\left[= \overrightarrow{\varepsilon} E_0 \sin\left(\omega t + \overrightarrow{k_L} \cdot \overrightarrow{z}\right)\right]$
$f(\upsilon)$	Laboratory frame velocity distribution
ϕ	Probe laser-beam axis angle
$\mathbf{F}$	Total angular momentum $[= \mathbf{J} + \mathbf{I}]$
F_{dip}	Dipole force
F_{ge}	Franck-Condon factor
F_{rad}	Radiation pressure force
Φ	Atom beam flux
g	Landé factor
$g(\upsilon)$	Power-broadened lineshape projected into velocity space
Γ	Natural linewidth $[= \tau^{-1}]$
Γ'	Power broadened linewidth
γ_i	Degeneracy of the i^{th} level

Parameter	Definition
h	Planck's constant [6.63×10^{-34} J s]
$\hbar$	Planck's constant/2π [1.05×10^{-34} J s]
i	PAI rate [= A − B]
I	Laser intensity
I_0	Initial intensity prior to entering absorptive medium
I_0	Saturation intensity for a transition
$\mathbf{I}$	Total nuclear spin
$I'(z)$	Attenuated intensity after passing through absorptive medium
J	Beam current [atoms/s]
$\mathbf{J}$	Electron angular momentum [$\mathbf{L} + \mathbf{S}$]
k_B	Boltzman constant [1.38×10^{-23} J K^{-1}]
$\overrightarrow{k_L}$	Laser wavevector
λ	Resonant wavelength [$= c/\omega_0$]
$L(\upsilon)$	Voigt lineshape of absorption profile
$\mathbf{L}$	Total orbital angular momentum
Λ	Liouville phase-space density
$\widetilde{\Lambda}$	Dimensionless Liouville phase-space density [$= \Lambda h^3$]
m	Atomic mass
μ	Reduced mass $\left[= \frac{m_1 m_2}{m_1 + m_2}\right]$
μ_{12}	Zeeman constant for $1 \longrightarrow 2$ transition [$= M_2 g_2 - M_1 g_1$]
μ_B	Bohr magneton [1.3996 MHz G^{-1}]
M	Magnetic quantum number
$M_{\mathbf{F}}$	Total angular momentum projection
n	Atomic ground-state density

Parameter	Definition
n	Principle quantum number
N	Number of photons/atoms
$\mathcal{N}$	Number of periods for ion counting
ω_0	Resonant frequency $\left[= \frac{E_2 - E_1}{\hbar}\right]$
ω_L	Laser frequency
Ω	Solid angle subtended by beam $\left[= \pi \left(\frac{\Delta v_\perp}{v_\parallel}\right)^2\right]$
Ω	Rabi frequency $\left[= -\frac{\tilde{d}E_0}{\hbar}\right]$
$P(v_r)$	Relative velocity distribution
P_{gr}	Penetration probability for 1D-LZ model
P_S	Penetration measure (or fractional ionization)
ρ_2	Excited state population
R	Brightness $[= \Phi/\Omega]$
$\mathcal{R}$	Condon point
θ	Suppression field axis-collision axis angle
θ	Suppression factor $[= 1 - P_S]$
σ_{12}	Absorption cross-section
S_0	Saturation parameter $\left[= \frac{I}{I_0} = \frac{\Omega^2/2}{(\Gamma/2)^2}\right]$
$\mathbf{S}$	Total electron spin
τ	Radiative lifetime
T_{coll}	Collision temperature
T_{long}	Longitudinal temperature (1D)
T_{trans}	Transverse temperature (2D)
T_D	Doppler temperature limit
T_R	Recoil temperature limit

Parameter	Definition
u_{ss}	Linear combination of steady state Optical Bloch Equations
U_{trap}	Dipole trapping potential
U_{SO}	Spin-orbit potential
$\langle \upsilon \rangle$	RMS velocity
υ_r	Relative velocity
υ_{ss}	Linear combination of steady state Optical Bloch Equations
υ_A	Atom velocity
υ_D	Doppler velocity limit
$\upsilon_{\|}$	Longitudinal velocity
$\upsilon_{\perp}$	Transverse velocity
$V_{gr}(R)$	Ground state potential
$V_{ex}(R)$	Excited state potential

BIBLIOGRAPHY

[1] Z.-T. Lu, C. J. Bowers, S. J. Freedman, B. K. Fujikawa, J. L. Mortara, S.-Q. Shang, K. P. Coulter, and L. Young. Phys. Rev. Lett. **72**, 3791 (1994).

[2] Z.-T. Lu, K. L. Corwin, M. J. Renn, M. H. Anderson, E. A. Cornell, and C. E. Wieman. Phys. Rev. Lett. **77**, 3331 (1996).

[3] E. J. D. Vredenbregt, K. A. H. van Leeuwen, and H. C. W. Beijerinck. Opt. Comm. **147**, 375 (1998).

[4] S. G. Miranda, S. R. Muniz, G. D. Telles, L. G. Marcassa, K. Helmerson, and V. S. Bagnato. Phys. Rev. A 59, 882 (1999).

[5] C. S. Adams, M. Sigel, and J. Mlynek. Phys. Rep. **240**, 143 (1994).

[6] J. Fujita, S. Mitake, and F. Shimizu. Phys. Rev. Lett. **84**, 4027 (2000).

[7] W. Demtröder. *Laser Spectroscopy*, 2nd ed (Springer, New York, 1996).

[8] R. W. McGowan, D. M. Giltner. and S. A. Lee. Opt. Lett. **20**, 2535 (1995).

[9] M. Kreis, F. Lison, D. Haubrich, D. Meschede, S. Nowak, T. Pfau, and J. Mlynek. Appl. Phys. B **63**, 649 (1996).

[10] R. E. Scholten, R. Gupta, J. J. McClelland, R. J. Celotta, M. S. Levenson, and M. G. Vangel. Phys. Rev. A **55**, 1331 (1997).

[11] F. Lison, H.-J. Adams, D. Haubrich, M. Kreis, S. Nowak, and D. Meschede. Appl. Phys. B **65**, 419 (1997).

[12] P. Engels, S. Salewski, H. Levsen, K. Sengstock, and W. Ertmer. App. Phys. B **69**, 407 (1999).

[13] W. E. Baylis. Can. J. Phys. **55**, 1924 (1977).

[14] B. Jaduszliwer and Y. C. Chan. Phys. Rev. A **48**, 2102 (1993).

[15] C.-C. Tsao, R. Napolitano, Y. Wang, and J. Weiner. Phys. Rev. A **51**, R18 (1995).

[16] J. J. Blangé, G. Aben, H. Rudolph, H. C. W. Beijerinck, and H. G. M. Heideman. J. Phys. B: At. Mol. Opt. Phys. **30**, 2789 (1997).

[17] H. V. Parks and S. R. Leone, J. Phys. Chem. A **103**, 10042 (1999).

[18] K. Helmerson, B. Davies, K. Mullman, and R. Kishore. Ann. Biomen. Eng. **26**, S-28 (1998).

[19] M. H. Anderson, J. R. Ensher, M. R. Matthews, C. E. Wieman, and E. A. Cornell. Science **269**, 198 (1995).

[20] C. Cohen-Tannoudji, J. Dupont-Roc, and G. Grynberg. *Atom-Photon Interactions: Basic Processes and Applications*, (Wiley, New York, 1992).

[21] S. Chu. Science **253**, 861 (1991).

[22] Y. Song, D. Milam, and W. T. Hill III. Opt. Lett. **24**, 1805 (1999).

[23] Y. Song. *Ph.D. Thesis*, (University of Maryland, College Park, MD, 1999).

[24] A. Thorne, U. Litzen, and S. Johansson. *Spectrophysics: Principles and Applications*, (Springer, New York, 1999).

[25] W. Ertmer, R. Blatt, J. L. Hall, and M. Zhu. Phys. Rev. Lett. **54**, 996 (1985).

[26] W. D. Phillips and H. Metcalf. Phys. Rev. Lett **48**, 596 (1982).

[27] P. D. Lett, W. D. Phillips, S. L. Rolston, C. E. Tanner, R. N. Watts, and C. I. Westbrook. J. Opt. Soc. Am. B **6**, 2084 (1989).

[28] S. Chu, L. Hollberg, J. E. Bjorkholm, A. Cable, and A. Ashkin. Phys. Rev. Lett. **55**, 48 (1985).

[29] E. M. Raab, M. Prentiss, A. Cable, S. Chu, and D. E. Pritchard. Phys. Rev. Lett. **59**, 2631 (1987).

[30] C.-C. Tsao, Y. Wang, J. Weiner, and V. S. Bagnato. J. Appl. Phys. **80**, 8 (1996).

[31] W. DeGraffenreid, J. Ramirez-Serrano, Y.-M. Liu, and J. Weiner. Rev. Sci. Inst., in press (2000).

[32] P. D. Lett, R. N. Watts, C. I. Westbrook, W. D. Phillips, P. L. Gould, and H. J. Metcalf. Phys. Rev. Lett. **61**, 169 (1988).

[33] J. Dalibard and C. Cohen-Tannoudji. J. Opt. Soc. Am. B **6**, 2023 (1989).

[34] C. Cohen-Tannoudji, B. Diu, and F. Laloë. *Quantum Mechanics*, (Wiley, New York, 1977).

[35] A. Siegman. *Lasers*, (University Science Books, Sausalito, CA, 1986).

[36] S. Gerstenkorn and P. Luc. *Atlas du Spectre D'Absorption de la Molécule D'Iode*, (CNRS Press, Paris, 1978).

[37] A. Yariv. *Quantum Electronics*, 3rd ed (Wiley, New York, 1989).

[38] J. F. Kelly and A. Gallagher. Rev. Sci. Instrum. **58**, 563 (1987).

[39] J. Weiner, V. S. Bagnato, S. Zilio, and P. S. Julienne. Rev. Mod. Phys. **71**, 1 (1999).

[40] W. DeGraffenreid, J. Ramirez-Serrano, Y.-M. Liu, A. Rosenbaum, and J. Weiner. in press (2000).

[41] J. Ramirez-Serrano, W. DeGraffenreid, and J. Weiner. unpublished (2000).

[42] J. R. Pierce, *Theory and Design of Electron Beams*, 2nd ed (Van Nostrand, Princeton, NJ, 1954).

[43] E. Riis, D. S. Weiss, K. A. Moler, and S. Chu. Phys. Rev. Lett. **64**, 1658 (1990).

[44] J. Uy, J. Djemaa, P. Nosbaum, and P. Pillet. Opt. Comm. **112**, 136 (1994).

[45] K. Dieckmann, R. J. C. Spreeuq, M. Weidemüller, and J. T. M. Walraven. Phys. Rev. A **58**, 3891 (1998).

[46] J. Nellessen, J. Werner, and W. Ertmer. Opt. Comm. **78**, 300 (1990).

[47] M. D. Hoogerland, J. P. J. Driessen, E. J. D. Vredenbregt, H. J. L. Megens, M. P. Schuwer, H. C. W. Beijerinck, and K. A. H. van Leeuwen. App. Phys. B **62**, 323 (1996).

[48] M. D. Hoogerland, D. Milic, W. Lu, H.-A. Bachor, K. G. H. Baldwin and S. J. Buckman. Aust. J. Phys. **49**, 567 (1996).

[49] F. Lison, P. Schuh, D. Haubrich, and D. Meschede. Phys. Rev. A **61**, 013405-1 (2000).

[50] D. R. Herschbach, in *Advances in Chemical Physics*, J. Ross ed. (Interscience, New York, 1966).

[51] F. Shimizu, K. Shimizu, K. Takuma. Chem. Phys. **145**, 327 (1990).

[52] Glascol Corp. Terre Haute, IN 47802. www.glasscol.com This is not to serve as an endorsement, but rather to let readers know about the availability of custom shaped heating mantles.

[53] R. J. Napolitano, S. C. Zilio, and V. S. Bagnato. Opt. Comm. **80**, 110 (1990).

[54] P. R. Fontana, Phys. Rev. **123**, 1865 (1961).

[55] J. B. Hasted. *Physics of Atomic Collisions*, 2nd ed (American Elsevier, New York, 1972).

[56] M. Marinescu, H. R. Sadeghpour, and A. Dalgarno. Phys. Rev. A **49**, 982 (1994).

[57] P. R. Fontana, Phys. Rev. **123**, 1871 (1961).

[58] W. J. Meath. J. Phys. Chem. **48**, 227 (1968).

[59] G. Herzberg. *Molecular Spectra and Molecular Structure, Vol I: Spectra of Diatomic Molecules*, 2nd ed (Van Nostrand, New York, 1950).

[60] W. I. McAlexander, E. R. I. Abraham, N. W. M. Ritchie, C. J. Williams, H. T. C. Stoof, and R. G. Hulet. Phys. Rev. A **51**, R871 (1995).

[61] K. M. Jones, P. S. Julienne, P. D. Lett, W. D. Phillips, E. Tiesinga, and C. J. Williams. Europhys. Lett. **34**, 85 (1996).

[62] H. Wang, P. L. Gould, W. C. Stwalley. Phys. Rev. A **53**, R1216 (1996).

[63] E. R. I. Abraham, W. I. McAlexander, C. A. Sackett, and R. G. Hulet. Phys. Rev. Lett. **74**, 1315 (1995).

[64] J. R. Gardner, R. A. Cline, J. D. Miller, D. J. Heinzen, H. M. J. M. Boesten, and B. J. Verhaar. Phys. Rev. Lett **74**, 3764 (1995).

[65] E. Tiesinga, C. J. Williams, P. S. Julienne, K. M. Jones, P. D. Lett, and W. D. Phillips. J. Res. Natl. Inst. Stand. Technol. **101**, 505 (1996).

[66] K. M. Jones, S. Maleki, S. Bize, P. D. Lett, C. J. Williams, H. Richling, H. Knöckel, E. Tiemann, H. Wang, P. L. Gould, and W. C. Stwalley. Phys. Rev. A **54**, R1006 (1996).

[67] L. Marcassa, S. Muniz, E. de Queiroz, S. Zilio, V. Bagnato, J. Weiner, P. S. Julienne, and K.-A. Suominen. Phys. Rev. Lett. **73**, 1911 (1994).

[68] L. Marcassa, R. Horowicz, S. Zilio, V. Bagnato, and J. Weiner. Phys. Rev. A 52, R913 (1995).

[69] S. C. Zilio, L. Marcassa, S. Muniz, R. Horowicz, V. Bagnato, R. Napolitano, J. Weiner, and P. S. Julienne. Phys. Rev. Lett. **76**, 2033 (1996).

[70] C.-C. Tsao, Y. Wang, R. Napolitano, and J. Weiner. Euro. Phys. J. D **4**, 139 (1998).

[71] H. Katori and F. Shimizu. Phys. Rev. Lett. **73**, 2555 (1994).

[72] M. Walhout, U. Sterr, C. Orzel, M. Hoogerland, and S. L. Rolston. Phys. Rev. Lett. **74**, 506 (1995).

[73] S. R. Muniz, L. G. Marcassa, R. Napolitano, G. D. Telles, J. Weiner, S. C. Zilio, and V. S. Bagnato. Phys. Rev. A **55**, 4407 (1997).

[74] K.-A. Suominen, M. J. Holland, K. Burnett, and P. Julienne. Phys. Rev. A **51**, 1446 (1995).

[75] V. A. Yurovsky and A. Ben-Reuven. Phys. Rev. A **55**, 3772 (1997).

[76] V. A. Yurovsky and A. Ben-Reuven. J. Phys. Chem. A **102**, 9476 (1998).

[77] R. Napolitano, J. Weiner, and P. S. Julienne. Phys. Rev. A **55**, 1191 (1997).

[78] J. R. Taylor. *An Introduction to Error Analysis* (University Science Books, Mill Valley, CA, 1982).

[79] J. Weiner and R. Napolitano. *Private Communication* (1999).

[80] E. Tiesinga. *Private Communication* (1999).

[81] J. Ramirez-Serrano, W. DeGraffenreid, and J. Weiner. unpublished (2000).

[82] V. A. Yurovsky and A. Ben-Reuven. *Private Communication* (1999).

[83] J. Ramirez-Serrano, W. DeGraffenreid, and J. Weiner. unpublished (2000).

[84] H. R. Thorsheim, J. Weiner, and P. S. Julienne. Phys. Rev. Lett. **58**, 2420 (1987).

[85] C. J. Smith, J. P. J. Driessen, L. Eno, and S. R. Leone. J. Chem. Phys. **96**, 8212 (1992).

[86] J. M. Mestdagh, J. P. Visticot, P. Meynadier, O. Sublemntier, and A. G. Suits. J. Chem. Soc. Faraday Trans. **89**, 1413 (1993).

[87] E. M. Spain, M. J. Dalberth, P. D. Kleiber, S. R. Leone, S. S. O. de Beek, and J. P. J. Driessen. J. Chem. Phys. **102**, 9522 (1995).

[88] E. M. Spain, M. J. Dalberth, P. D. Kleiber, S. R. Leone, S. S. O. de Beek, and J. P. J. Driessen. J. Chem. Phys. **102**, 9532 (1995).